CHARACTERIZATION AND MECHANICAL PROPERTIES OF NANOSCALE PRECIPITATES IN MODIFIED Al-Si-Cu ALLOYS USING TRANSMISSION ELECTRON MICROSCOPY AND 3D ATOM PROBE TOMOGRAPHY

Junyeon Hwang, B.S., M.S.

Dissertation Prepared for the Degree of

DOCTOR OF PHILOSOPHY

UNIVERSITY OF NORTH TEXAS

May 2007

APPROVED:

M.J. Kaufman, Major Professor and Chair of the Department of Materials Science and Engineering
R. Banerjee, Committee Member
T.W. Scharf, Committee Member
B.P. Gorman, Committee Member
N.A. D'Souza, Graduate Advisor of Department of Materials Science and Engineering.
O.N. Garcia, Dean of College of Engineering
Sandra L. Terrell, Dean of the Robert B. Toulouse School of Graduate Studies

Hwang, Junyeon. *Characterization and mechanical properties of nanoscale precipitates in modified Al-Si-Cu alloys using transmission electron microscopy and 3D atom probe tomography*. Doctor of Philosophy (Materials Science and Engineering), May 2007, 172 pp., 11 tables, 72 figures, chapter references.

Among the commercial aluminum alloys, aluminum 319 (Al-7wt%Si-4wt%Cu) type alloys are popularly used in automobile engine parts. These alloys have good casting characteristics and excellent mechanical properties resulting from a suitable heat treatment. To get a high strength in the 319 type alloys, grain refining, reducing the porosity, solid solution hardening, and precipitation hardening are preferred. All experimental variables such as solidification condition, composition, and heat treatment are influence on the precipitation behavior; however, precipitation hardening is the most significant because excess alloying elements from supersaturated solid solution form fine particles which act as obstacles to dislocation movement. The challenges of the 319 type alloys arise due to small size of precipitate and complex aging response caused by multi components. It is important to determine the chemical composition, crystal structure, and orientation relationship as well as precipitate morphology in order to understand the precipitation behavior and strengthening mechanism. In this study, the mechanical properties and microstructure were investigated using transmission electron microscopy and three dimensional atom probe tomography. The Mn and Mg effects on the microstructure and mechanical properties are discussed with crystallographic study on the iron intermetallic phases. The microstructural evolution and nucleation study on the precipitates in the low-Si 319 type aluminum alloys are also presented with sample preparation and analysis condition of TEM and 3DAP tomography.

ACKNOWLEDGEMENTS

I would like to express my deepest respect and gratitude to Dr. Kaufman for his outstanding advice, continuous support, and trust on me. Without his encouragements and help, I could not have finished the dissertation.

I would like to express my appreciation to the committee Dr. Banerjee, Dr. Gorman, and Dr. Scharf for their interactive discussion and help.

I would also like to great acknowledge to Dr. Doty for the financial and some experimental results through GM Powertrain.

I would like to express great thank to my colleagues and staff in Materials Science and Engineering department.

I would like to thank to my wife Hyunju, for her support, patience, and encouragement. I am very proud of my two sons, Inseoh and Insol.

TABLE OF CONTENTS

Page

ACKNOWLEDGEMENTS iii

LIST OF TABLES vi

LIST OF FIGURES vii

INTRODUCTION 1

Chapter

1. BACKGROUNDS 3
   - 1.1 Microstructure, Casting Defects, and Mechanical Properties of the Type 319 Alloys 3
   - 1.2 Precipitation Hardening of the Al 319 Alloy 8
   - 1.3 Precipitation Strengthening Mechanisms of 319 Aluminum Alloy 12
   - 1.4 Characterization of Precipitates 15
   - 1.5 Reference 18

2. THE EFFECTS OF Mn ADDITIONS ON THE MICROSTRUCTURE AND MECHANICAL PROPERTIES OF Al 319 ALLOYS 20
   - 2.1 Introduction 20
   - 2.2 Experimental Procedure 21
   - 2.3 Results and Discussion 23
     - 2.3.1 Microstructure Analysis 23
     - 2.3.2 Fractography 33
     - 2.3.3 Mechanical Properties 39
   - 2.4 Reference 44

3. CRYSTALLOGRAPHIC STUDIES ON THE IRON BASED INTERMETALLIC PHASES IN THE 319 TYPE ALUMINUM ALLOYS 45
   - 3.1 Introduction 45
   - 3.2 Experimental Procedure 47
   - 3.3 Results and Discussion 48
   - 3.4 Reference 64

4. THE EFFECTS OF Mg ADDITIONS ON THE MICROSTRUCTURE AND MECHANICAL PROPERTIES OF 319 ALUMINUM ALLOYS 65
4.1 Introduction 65
4.2 Experimental Procedure 66
4.3 Results and Discussion 68
4.3.1 As-Cast Microstrucutre 68
4.3.2 Microstructure in the T6 Condition 75
4.3.3 Mechanical Properties Studies 84
4.4 Reference 86

5. CHARACTERIZATION OF THE THREE DIMENSIONAL STRUCTURE OF NANOSCALE PRECIPITATES IN MODIFIED 319 TYPE Al ALLOYS 87
5.1 Introduction 87
5.2 Experimental Procedure 89
5.3 Results and Discussion 89
5.4 Reference 101

6. MICROSTRUCTURAL EVOLUTION IN LOW-Si 319 TYPE Al ALLOYS 102
6.1 Introduction 102
6.2 Experimental Procedure 105
6.3 Results and Discussion 108
6.3.1 Observations of T6 Samples 108
6.3.2 Observations of T7 Samples 117
6.4 Reference 129

7. HIGH RESOLUTION TEM STUDY OF HETEROGENEOUSLY NUCLEATED θ' PHASE IN THE Al-Si-Cu-Mg ALLOYS 131
7.1 Introduction 131
7.2 Experimental Procedure 132
7.3 Results and Discussion 133
7.4 Reference 147

8. CONCLUSIONS 148

Appendices

A. FIB SAMPLE PREPARATION FOR ATOM PROBE AND TEM, AND ANALYSIS CONDITIONS OF THE Al-Si-Cu-Mg ALLOYS FOR 3DAP RECONSTRUCTION 151

B. PRECIPITATION STRENTHENING MODELS OF MODIFIED 319 TYPE ALUMINUM ALLOYS 162

LIST OF TABLES

Page

1.1 Crystallographic and morphology of various precipitates observed in the Al-Si-Cu-Mg systems 9

2.1 Target compositions of the alloys used in this study 22

2.2 Average EDX results of the different iron intermetallic phases 27

2.3 The area percent of porosity measured from the metallographic and fracture surfaces of the four alloys 29

2.4 The volume percent of iron containing intermetallic and Si phases 30

3.1 Target compositions of the 319 alloys used in this study 49

3.2 Measured compositions of β and α phases measured by EDS in both the SEM and TEM 49

3.3 Summary of crystallographic data for Al[Fe,Mn]Si phase and AlFeSi phase in the aluminum alloys 54

4.1 Compositions of the Type 319 aluminum alloys used in the experiment 67

5.1 Crystallographic and chemical composition data of selected phases 91

6.1 Composition of the alloy used in the present study 106

LIST OF FIGURES

Page

1.1 Measured yield strength of 3.5 wt% Cu in Al 319 alloy after aging at 190°C, 230°C, and 260°C 11

1.2 Increase in yield strength with particle diameter as a result of shearing and looping model 14

1.3 Schematic diagram of the research performed in this study 17

2.1 SEM microstructures observed in the 319 type aluminum alloys after T6 heat treatment (a) Mn02, (b) Mn30, (c) Mn65, and (d) Mn85 sample 24

2.2 Optical microstructures observed in the 319 type aluminum alloys after T6 heat treatment (a) Mn02, (b) Mn30, (c) Mn65 and (d) Mn85 sample 25

2.3 SEM microstructures observed in the 319 type aluminum alloys after T6 heat treatment. Mn02, (b) Mn30, (c) Mn65, and (d) Mn85 sample showing the α, β intermetallic phases 26

2.4 Micrographs showing the pore observed around the β phase from Mn02 (a), and α phase from Mn65 (b) 31

2.5 Micrographs showing the Si, α, and β phase in the deep etched samples, (a) Mn02, (b) Mn30, (c) Mn65, and (d) Mn85 sample after T6 heat treatment 32

2.6 Micrographs showing the fracture surface (a), crack initiation and propagation along the pore (b), and silicon particles (c) 34

2.7 SEM images and EDS maps of the fracture surfaces of the Mn02 sample (a) and (b), and the Mn85 sample (c) and (d) 35

2.8. Secondary electron (SE) and backscattered electron (BE) images on the fracture surface. (a) Mn02, (b) Mn30, (c) Mn65, and (d) Mn85 sample 38

2.9 Yield strength (YS), and ultimate tensile strength (UTS) as a function of Mn contents in the 319 type aluminum alloys 41

2.10 Ductility as a function of Mn content in the 319 type aluminum alloys after the T6 heat treatment 42

3.1 Microstructures of two types of iron intermetallic phases in the type 319 alloys 50

3.2 Electron backscattered diffraction patterns of the iron intermetallic phases 52

3.3 Plane traces on the stereoprojection and SAD pattern of [111] zone axis of the α phase 55

3.4 Bright field image of Chinese script-like α phase and its CBED patterns from the 3 different zone axis 56

3.5 Schematic illustrations of Kikuchi lines and CBED patterns of the Chinese-script α phase 57

3.6 Bright filed image of β phase and selected area diffraction patterns taken from characteristic major zone axes 61

3.7 (a) Bright field image and (b) dark field image of plate-like β phase in faulted area, and SAD patterns of taken from non-fault area (c,d) and faulted area (e,f)62

3.8 Schematic illustrations of appearance of (h21) planes on the [021] zone axis under the faulted β region 63

4.1 Optical micrographs of the as-cast condition in Mg-free(a), and Mg containing (b) 319 type aluminum alloys 69

4.2 SEM microstructure and EDX maps of the Mg-free alloy in the as-cast condition 70

4.3 SEM microstructure and EDX maps of the Mg-containing alloy in the ascast condition 71

4.4 Section of the quaternary phase diagram for the Al-Si-Cu-Mg system at 502°C and 4 wt% Cu 73

4.5 BF TEM image and selected area diffraction patterns of the Q phase in the Mg-containing sample in the as-cast condition 74

4.6 Optical micrographs of the T6 condition in the Mg-free(a), and Mg containing (b) 319 type aluminum alloys 76

4.7 SEM microstructure and EDX maps of the Mg-free alloy after T6 aging heat treatment 77

4.8 SEM microstructure and EDX maps of the Mg-containing alloy after the T6 aging heat treatment 78

4.9 TEM bright field image and [001] SAD pattern from the Mg-free alloy after the T6 heat treatment. The extra reflections and streaking in the SADP are consistent with the presence of thin θ' precipitates 81

4.10 TEM bright field image and [001] SAD pattern from the Mg-containing alloy after the T6 heat treatment. The extra reflections in the SADP result from the presence of small Q' precipitates 82

4.11 Three dimensional atom maps showing the distribution of the Al, Si, Cu, and Mg atoms in the Mg-containing alloy after the T6 heat treatment 83

4.12 Ultimate tensile strength and % elongation of Mg-free and Mg-containing samples in the as-cast condition (blue) and the T6 condition (red)..... 85

5.1 BF TEM micrograph in the as-cast condition showing the various interdendritic phase including silicon, iron containing intermetallic, and θ and Q phase 91

5.2 TEM results on the T6 conditions, (a) BF TEM micrograph, (b) SAD pattern, (c) DF TEM image showing the plate shape of θ' precipitate..... 92

5.3 Three dimensional isoconcentration surfaces of the θ' precipitates in the modified 319 type aluminum alloy ages at T6 condition..... 93

5.4 STEM micrograph showing the lath-shaped precipitates (a), and EDS spectra (b) obtained from white arrow containing Al, Cu, Si, and Mg 95

5.5 HRTEM images showing the two variants of lath-shaped precipitates 96

5.6 Three dimensional isoconcentration surfaces of the θ' and Q' precipitates showing two different view direction in the modified 319 type aluminum alloy ages at T6 conditions 97

5.7 Compositional profiles through the θ' phase (mark 1) and Q' phase (mark 2) along the cylindrical line 100

6.1 Ternary phase diagram of aluminum rich corner of the Al-Cu-Mg system showing the phase fields as a function of compositions after long term aging at 190°C 103

6.2 SEM micrographs of the atom probe specimens prepared on the Si microtips (a), and the high magnification images on the edge (b)..... 107

6.3 TEM micrographs and corresponding SAD patterns of the Al-Cu-Mg-Si alloy aged at 198°C for 8 h near the <001> Al direction..... 109

6.4 HRTEM micrographs and corresponding FFT spectrums on the θ' precipitates of Al-SI-Cu-Mg alloys aged at 198°C for 8 h along the (a) [001]Al, and (b) [011]Al beam direction 110

6.5 Transmission electron micrograph, in <110> Al orientation showing the presence of θ' phase and GPB zone..... 111

6.6 High resolution TEM micrograph and corresponding FFT spectra on the rod type precipitate of Al-Cu-Mg-Si alloy aged at T6 condition along the $<001>_{Al}$ direction 114

6.7 3DAP reconstructions of two different shapes of precipitates and their compositional profiles 115

6.8 TEM micrographs on the Mn containing particles. (a) lath shape particles along the <011> Al direction, (b) and (c) large globular shape particles with random oriental relationship with matrix 116

6.9 BF TEM near **B=**$<001>_{Al}$ showing the various precipitates after the T7 aging treatment. (a) Low magnification and (b) higher magnification showing the fine precipitates 118

6.10 Transmission electron micrographs near **B=** $<112>_{Al}$ showing the presence of Si-modified GPB2 zone 119

6.11 High resolution TEM micrographs and corresponding FFT spectra on the new precipitates of Al-SI-Cu-Mg alloys aged at T7 along the [001] Al matrix direction 121

6.12 3DAP reconstruction results on the T7 aging treatment sample showing the rod type precipitates 122

6.13 TEM micrograph, in <001> Al matrix showing the presence of θ' phase and Al_2Cu. (a) BF TEM image and corresponding SAD pattern (b), and DF images obtained using the streaks marked by A 126

6.14 3D reconstruction of Al_2Cu precipitates in the modified Al-Si-Cu-Mg alloy and its compositional profile 127

6.15 3D reconstruction of Si modified Al_2CuMg precipitate in the modified Al-Si-Cu-Mg alloy and its compositional profile 128

7.1 HAADF-STEM micrograph showing the 2 abnormally thick Al_2Cu phases marked by A and B 134

7.2 EDX spectra obtained from precipitates marked A, B, C, and D 135

7.3 3D atom probe results show the existence of lath shape Al_2Cu precipitates .. 136

7.4 The 1 D compositional profiles from Fig.7.3 (c) and (d) 137

7.5 BFTEM micrograph and corresponding microdiffraction pattern (indexed as a <013>zone axis from α-Al[Si,Mn]Cu) of a region containing the globular phase nucleating two different Al_2Cu laths 139

7.6 Microdiffration patterns from the lath types of θ' precipitate..... 140

7.7 HRTEM from lath type precipitate..... 141

7.8 3D atom probe results showing the plate shape of θ' precipitate that heterogeneously nucleated on the Si modified GPB zone..... 145

7.9 HRTEM (a) and FFT (b) showing heterogeneous nucleation of θ' precipitate from the Si modified GPB zone 146

A1 Specimen preparation procedure using the FIB on the Si microtips 156

A2 Mass to charge spectra from the 3DAP 157

A3 TEM bright field micrograph, SAD pattern and EDX spectra obtained from circled area, respectively in (a), (b), and (c)..... 158

A4 Three dimensional atom maps showing the distribution of Si (a), Cu (b), and Mg (c) atoms, and isoconcentration surface images (e) and its compositional profile (f)..... 159

B1 Simulated yield strength model strengthened by θ' precipitates 163

B2 Simulated yield strength results strengthened by Q' precipitates 165

B3 Simulated yield strength by micromechanical model 168

B4 Experimental results measured by Rockwell hardness as a function of aging time 169

INTRODUCTION

In an automotive industry, aluminum cast alloys are the most widely used in order to reduce vehicle weight. Among the commercial aluminum alloys, aluminum 319 (Al-7wt%Si-4wt%Cu) and aluminum 356 (Al-7wt%Si-0.3wt%Mg) are popularly used in engine parts. Recently, the Al 319 type alloys have more attractive interest for high temperature application even though Al 356 type alloys have been widely studied over the last 40 years. These alloys have good casting characteristics and excellent mechanical properties resulting from a suitable heat treatment. Several studies on the 319 aluminum alloys have been conducted in recent years to enhance their strength, and ductility.

To get high strength in the 319 type alloys, grain refining, reducing the porosity, solid solution hardening, and precipitation hardening are preferred. All experimental variables such as solidification condition, composition, and heat treatment influence the precipitation behavior. Therefore, understanding the whole process is important to control the precipitation hardening and achieving desired strength. However, precipitation hardening is the most significant because excess alloying elements from supersaturated solid solution form fine particles which act as obstacles to dislocation movement.

The challenges of the 319 type alloys arise due to small size of precipitate and complex aging response caused by multi components. It is important to determine the chemical composition, crystal structure, and orientation relationship as well as precipitate morphology in order to understand the precipitation behavior and strengthening mechanism. In this study, the mechanical properties and microstructure

were investigated using the transmission electron microscopy and three dimensional atom probe tomography.

A short background and research motivations for this study are given in chapter 1. The Mn effects on the microstructure and mechanical properties are discussed in chapter 2. The crystallographic study on the iron intermetallic phases are described in chapter 3. The Mg effect on the microstructure and mechanical properties on the peak aging heat treatment are presented in chapter 4, and 5. The microstructural evolution and nucleation study on the low Si alloy are discussed in chapter 6, and 7. Finally, conclusions are summarized in chapter 8. The sample preparation and experimental procedure transmission electron microscopy (TEM) and three dimensional atom probe (3DAP) tomography is described in the appendix A. The models of strengthening based on the two different types of precipitates are discussed in the appendix B.

CHAPTER 1

BACKGROUNDS

1.1 Microstructure, Casting Defects, and Mechanical Properties of the Type 319 Alloys

The compositions of aluminum 319 type aluminum alloys are aluminum, silicon, copper and some other impurity elements such as iron, magnesium, zinc, and manganese [1]. The roles of Si is to increase the castability and mechanical properties such as corrosion and wear resistance, and reduce the thermal expansion coefficient. When the alloy solidifies, primary Al dendrite and faceted Si particle form and grow with iron containing intermetallic compounds. When the eutectic temperature is reached, the eutectic Al-Si grows. At this temperature brittle intermetallic compounds also forms along the interdendritic region [2].

The 319 aluminum alloys have common casting defects such as porosity and inclusions [3]. Porosity is one of the most common casting defects which can greatly degrade the mechanical properties of the aluminum alloy. Pore, a source of stress concentrator, cannot sustain external load, and hence can lead to initiation and propagation of microcrack. Gas porosity is generated when alloy solidifies from the melt. The hydrogen atoms come out from the melt and form molecular hydrogen. On the other hand, microporosity can be formed along the dendrites after the solidification [4]. In general, the increase of the solidification rate tends to reduce the pore size as well as to promote a finer distribution of gas and microshrinkage porosity. Several studies on the 319 aluminum alloys reveal that fatigue cracks initiate from casting pores located either close to or at the specimen surface [5, 6]. Porosity appears to be the dominant factor in fatigue life compared to area or volume percentage porosity. Boileau et al.[5]

observed that the source of the initiation crack sites was large porosity located near the surface rather than intermetallic compounds, and oxides. The various intermetallic phases such as $Al_{12}(Fe, Mn)_3Si$, Al_5FeSi, and $Al_5Mg_8Cu_2Si_6$ can be formed in these alloys due to high electronegativity and trivalence of the constituent elements [4]. Intermetallic phases are also deleterious to the mechanical properties like pore. These features can act as stress raisers for crack nucleation or as low-energy paths for crack propagation. Among the intermetallic compounds in Al 319 alloys, β-Al_5FeSi phase, which tends to form thin platelets appearing as needles in cross section, is very hard and brittle nature. To reduce the detrimental effect of iron, rapid solidification and melt superheating are used. The intermetallic phases tend to increase the average size as the solidification time increases [5]. However, the rapid solidification rate converts the crystallization of the needlelike β-Al_5FeSi phase to the less harmful Chinese script form (α-AlFeSi phase). This rapid solidification effect appeared only at low level of iron content [3].

To improve the mechanical properties many techniques are devised. First, increase the solidification rate to obtain fine dendrite structure. As the solidification time increases, the secondary dendrite arm spacing also increases and the size and shape of the eutectic silicon became larger and more acicular. Boileau et al. reported that the ultimate tensile strength and ductility are strong functions of solidification time [5]. The increase in the solidification time of Al 319 alloy resulted in the decreases of strength. The formation of coarse eutectic Al_2Cu and segregation from the matrix were causes of the decrease in strength. The thick regions of wedge have small amount of copper in solid solution. This will also lead to lower the strength during precipitation hardening.

The effect of solidification time on the room temperature tensile properties of the Al 319 alloy is presented in Fig.1. In addition, reduced hydrogen content in the melt increase the strength due to low porosity in the final casting [6]. Degassing is also favorable to increase the strength. Vacuum processing, purging inert gas bubbles through molten alloy are actively used to remove the hydrogen gas and obtain fine pore size. The coarse grains and silicon particle are also very detrimental to the mechanical properties. Commonly TiB and Sr are used for grain refiner and silicon modifier, respectively [4].

Alloying elements influence greatly the porosity and morphology of the as-cast 319 alloys as well as solidification condition. Modification of aluminum alloy is normally carried out to improve the mechanical properties. In this alloy, the addition of strontium or/and sodium is to modify the shape of the eutectic silicon from acicular to fibrous [7]. The modified eutectic structure enhances the mechanical properties of the casting. However, this advantage is offset because the modified castings generally increase the amount of porosity, and then adversely affect the fatigue property [6]. The effects of each alloying element on the porosity and microstructure are described as follows.

Si Effect

Al-Si binary alloy is a eutectic system with the composition at 12.6wt% Si. Silicon reduces the thermal expansion coefficient, increases corrosion and wear resistance, and improves casting and machining characteristics of the aluminum alloy [8]. The investigation of Si contents on the grain size and dendritic morphology was reported by Veldman et al.[9]. They showed that silicon has a greater effect on the grain size than cooling rate. As the silicon content increases, the grain size increases, while the morphology changes from almost spherical grains to orthogonal dendritic grains.

Cu Effect

The addition of copper to the Al-Si alloys improves the strength of the castings. Copper in these alloys is present as Al_2Cu or in a complex forms like blocky form, or as a fine eutectic colony. Copper in various levels does not significantly influence the grain size [6]. Caceres reported that Cu content exceeding 0.2 wt% results in a 7 times increase in dispersed microporosity [10], which seemed to be correlated well with the formation of large amount of interdendritic Cu-rich phase. Copper is a main element of precipitation hardening during heat treatment, therefore, strength is influenced by the copper content.

Sr Effect

The modification of the eutectic silicon is usually carried out using strontium which converts the silicon morphology from an acicular to a fibrous form. The presence of Sr leads the dissolution of β needle phase and results in severe segregation of the iron and copper intermetallics from the modified eutectic silicon [9]. The other generally agreed effect of Sr is that the addition of Sr increases the percentage porosity, while the cause of this increase still disputed [11].

Mg Effect

The addition of magnesium reduces porosity without a noticeable change in pore size or shape. The Mg combined with refiner such as titanium and boron minimizes porosity even in high hydrogen containing alloys [6]. The addition of magnesium has a beneficial effect on the mechanical and machining properties. The addition of Mg up to 0.5wt%, to the molten 319 type alloys leads to the precipitation of Mg_2Si phase that appears in the form of rounded black particles dotted along the sides of the eutectic Si

particles. In addition, noticeable transformation of a large proportion of the needle type β-Al_5FeSi phase into a less detrimental Chinese script-like phase ($Al_8Mg_3FeSi_6$) is observed [9].

Zn Effect

Zinc has relatively high solubility in aluminum both at high and low temperatures. A high level of 3wt% has been reported to improve high temperature properties, but role of zinc in porosity and mechanical properties are not clear [6].

Mn Effect

Manganese is normally used to modify intermetallic phases in cast aluminum alloys. A common practice is to add a small quantity of Mn to the melt to promote the formation of α-$Al_{15}(Mn,Fe)_3Si_2$ to neutralize β phase [3]. In order to obtain the crystallization of the iron compound in the Chinese script morphology, a certain critical ratio of Fe and Mn is required. With the increase of the manganese level from 0.35 to 0.7%, the length of the β phase decreases markedly at all cooling rate.

Other Elements

The alloying elements such as sodium, phosphorous, titanium, and boron in modifying silicon phase morphology or refining grains also have effects on porosity formation. In general, the addition of grain refiners increases the number of nucleation sites, reduces grain size, and decreases the volume fraction and size of pores. Commonly Ti and B is known as grain refiner [12], and beryllium is use to modify the morphology of iron containing intermetallic compound to comparatively harmless phases [8].To optimize the proper condition for controlling the morphology, solidification and each alloying element effects must be comprehensively considered.

1.2 Precipitation Hardening of the Al 319 Alloy

Heat treatment is the most favorable method to increase the strength or improve the ductility in the cast 319 alloy. In order to increase the strength in Al-Si alloy, appreciable amounts of copper and magnesium are added in the automotive engine application. Typical Al 319 alloy for automotive application contains the 5.5-10wt%Si, 2.0-4.0wt%Cu, 0.1-1wt%Mg, 1.0max.wt%Fe [13]. The Mg and Cu elements precipitate out forming the fine particles during the aging treatment. However, the details of age hardening for Al 319 cast alloys have not yet been thoroughly investigated. Several sequences of precipitation can be expected in this alloy system as follows [14-16].

$$\alpha_{ss} \rightarrow \text{G.P. zones} \rightarrow \theta' \rightarrow \theta\ (Al_2Cu)$$

$$\alpha_{ss} \rightarrow \text{G.P. zones} \rightarrow S' \rightarrow S\ (Al_2CuMg)$$

$$\alpha_{ss} \rightarrow \text{G.P. zones} \rightarrow \beta' \rightarrow \beta\ (Mg_2Si)$$

$$\alpha_{ss} \rightarrow \text{G.P. zones} \rightarrow Q' \rightarrow Q\ (Al_5Cu_2Mg_8Si_6)$$

The various hardening precipitates in aluminum alloys are summarized by Chakrabarti and Laughlin [16].

Table 1.1 Crystallographic and morphology of various precipitates observed in the Al-Si-Cu-Mg systems [16]. [Reproduced with permission from Elsevier.]

Alloy system	Equilibrium phase (Bravais lattice)	Metastable phase		Metastable phase		
		Isostructural	Non-Isostructural	Bravais lattice (Shape)	Habit plane	Orientation relation
		(with equilibrium phase)				
Al–Cu	θ (body centered tetragonal)		θ′	Body centered tetragonal (plate)	{100}	$[001]_{Al}//[001]\theta'$ $(100)_{Al}//(100)\theta'$
Al–Mg–Si	β (face centered cubic)		β′	Hexagonal (rod)	–	$[001]_{Al}//[0001]\beta'$ $(110)_{Al}//(10\bar{1}0)\beta'$
Al–Cu–Mg	S (side centered orthorhombic)	S′		Side centered orthorhombic (lath)	{210}	$[001]_{Al}//[001]_{S'}$ $(210)_{Al}//(010)_{S'}$
Al–Mg–Si–Cu	Q (hexagonal)	Q′		Hexagonal (lath)	{150}	$[001]_{Al}//[0001]_{Q'}$ $(020)_{Al}//(21\bar{3}0)_{Q'}$

The θ' phase is primarily observed in the Al 319 alloys [13]. Other precipitates including magnesium precipitates are not commonly observed in the underaged condition. Even if observed, the amount of the precipitates is small and negligible. Allison et al. found that there are small semi-coherent metastable phases of θ, and quaternary metastable phase of Q at T6 aging [15]. Esmaeili et al. [17] investigated the thermal stability of β' and Q' phase using differential scanning calorimetry (DSC) on the Al-0.79wt%Mg-0.6wt%Si-0.7wt%Cu-0.25wt%Fe-0.2wt%Mn. It was reported that the most prominent peak for the as quenched sample was the exothermic peak associated with β" phase. This peak significantly decreased in magnitude after 30 minutes of aging and completely disappeared after aging 1 hour at 180^{o}C. They also found that the number of density and volume fraction of Q' precipitates increase steadily during peak aging condition. On the other hand, the density and volume of β' phase increased appreciably during the first hour of aging at 180 ^{o}C. The rate of decrease of β'

precipitate beyond the peak aging temperature, was more pronounced than that of the Q' phase. It is believed that the kinetics of β' precipitate is rapid compared to that of Q' phase. Not much data is published on the aging hardening in the 319 alloys. For most applications, the T6 treatment (peak aging treatment after solution heat treatment) is usually carried out because it can produce maximum tensile strength and hardness. The solution treatment for the Al 319 alloys has two objectives: one objective is to obtain maximum solubility and homogeneity of the alloying elements and impurities in the matrix, the other objective is to modify the acicular morphology of the eutectic silicon to a less detrimental, rounded one [18]. Therefore, solution temperature must be high enough and the treatment time long enough to allow maximum dissolution and homogenization of the alloying elements. Apelian et al. [19] suggested that the solution heat treatment temperature should be close to the eutectic temperature as possible. The control of temperature is very critical, because localized melting occurs at the grain boundaries when the temperature exceeds the melting point and the mechanical properties are reduced. Temporary overheating with respect to the melting point is known to form voids [19].

Weakley-Bollin and Allison [15] presented the strength as a function of aging time and temperature in Fig.1.1. The composition of this alloy is Al-7.5wt%Si-3.5wt%Cu-0.32wt%Fe with small amounts of Mg, Mn, and Sr. After solution treatment at 495^{o}C for 8 hours, quenching in boiling water, and then aged for several hours, the age hardening behavior follows similar with the typical age-hardenable aluminum alloy. By increasing the aging time, the strength or hardness increases until reaching the peak point, and then decreases.

The strengthening process is accelerated as the temperature is increased. The strengthening occurs primarily due to precipitation of plate-shaped precipitate, θ'. Allison also reported that at the peak aged condition, the θ' precipitates are sufficiently thin to produce highly streaked intensity in the diffraction patterns. The effect of the copper concentration on the precipitate diameter and thickness during aging was investigated in three samples having different Cu concentrations (3.0, 3.5 and 4.0wt%). They found that the diameters and thickness of the θ' precipitates are independent of copper concentration over the range of compositions, aging times, and temperatures.

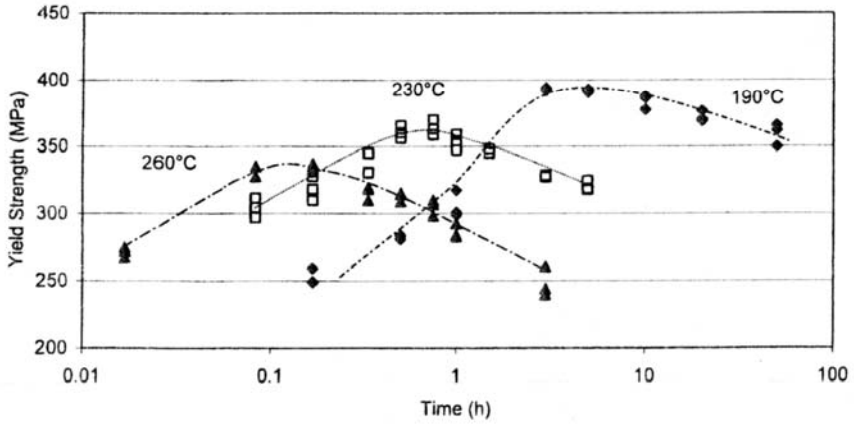

Fig.1.1 Measured yield strength of 3.5wt% Cu in Al 319 alloy after aging at 190^{o}C, 230^{o}C, and 260^{o}C [15]. [Reproduced with permission from Springer.]

1.3 Precipitation Strengthening Mechanisms of 319 Aluminum Alloy

Aluminum 319 alloy is age-hardenable alloy. The strength of such alloy can be described as sum of an intrinsic strength (σ_i), a precipitation-hardening strength (σ_{ppt}), and a solid solution strength (σ_{ss}):

$$\sigma_Y = \sigma_I + \sigma_{SS} + \sigma_{ppt} \quad (2.1)$$

The intrinsic strength is assumed to be constant, while other two factors are related with the interaction of precipitate and solute atom in the matrix. In this alloy, the peak yield strength can be achieved by precipitation hardening process. Many attempts have been produced in this field and will be described here [20-25].

In the following discussion, the contribution of each strengthening mechanism of the present alloy is described based on the theoretical analysis.

1.3.1 Boundary Strengthening

The role of crystallographic boundaries and grain can be described by the following Hall-Petch equation

$$\sigma_{ys} = \sigma_0 + kd^{-1/2} \quad (2.2)$$

where $\boldsymbol{\sigma_0}$ and $\boldsymbol{k}$ are material constant and $\boldsymbol{d}$ is grain size. This boundary strengthening affects on the intrinsic strength ($\boldsymbol{\sigma_i}$) on the total yield strength of materials. The boundary effect on the strength is not big in the cast 319 aluminum alloys compared to precipitation strengthening parameters.

1.3.2 Solid Solution Strengthening

Solid solution strengthening is result from the interaction between solutes in solid solution and moving dislocations. The degree of solid solution effects are generally evaluated when an alloy is in as-quenched condition after solution heat treatment. The

effects of solid solution strengthening weaken gradually and completely disappear after the peak aging point. However, there is no strong physical formulation of this term as a function of aging temperature and solute concentration due to its complexity of this contribution. Therefore, simple modification by fitting with experimental data is used for determining the solid solution effect [26].

1.3.3 Precipitate Strengthening

Precipitation strengthening is one of the several effective methods to increase the yield strength of aluminum alloys. Precipitates increase strength of the alloy by impeding the motion of dislocations. There are two types of dislocation-particle interactions.

Dislocation bypass model and shear model. When the particle size is larger than critical size, dislocation will bypass remaining the dislocation loop which suggested by Orowan [27]. When the particle size is smaller than critical size, the dislocations shear or pass through the particles. In Fig.1.2, yield strength plots are presented as a function of particle size using both models.

The strength of a particle is related to its size. A shearing and looping curve Fig.1.2 [17] shows the potential of spherical type of precipitate strengthening with particle diameter. It consists of two stages. In stage 1, less than 2.7nm particle diameter, the resistance of a precipitate against dislocation cutting results in strength increase. In stage 2, larger than 2.7nm, a dislocation is forced to loop around the precipitate rather than cutting through, which also results in increase strength compared to the solution treated materials.

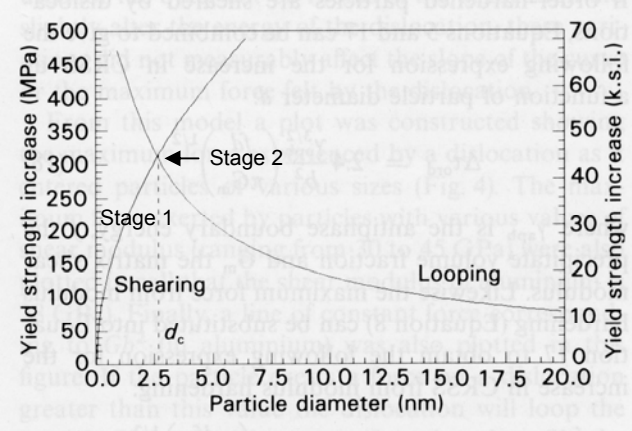

Fig.1.2 Increase in yield strength with particle diameter as a result of hearing and looping model [17]. [Reproduced with permission from Springer.]

The Orowan looping model can be applied to the shear resistant particles and coherent particle which have high misfits [29]. The θ' and Q' precipitates belong to this criteria, therefore strengthening mechanism follows the Orowan equation like

$$\tau = \frac{G\,\mathbf{b}}{2\,r}$$

The shear model strengthening basically 6 properties of the particles which affect the ease with which they can be sheared such as

(1) Coherency hardening

(2) Modulus hardening

(3) Ordered hardening

(4) Interfacial and morphology hardening

(5) Lattice friction hardening

(6) Stacking-fault hardening

Shear model has simultaneously operated two or more of these hardening mechanisms. However, it is not clear how relative strengthening contributions are significant. Thus it remains as a major challenge to evaluate the hardening mechanism in shear particle model. In the 319 alloy system at T6 aging condition, generally θ' particles larger than several tens nanometer size are main hardening phase. Because precipitate size is larger than d_c the dislocations bypass them either by looping, cross-slipping or climbing, Orowan mechanism is only important to understand the precipitation hardening.

1.4 Characterization of Precipitates

The strength can be directly related to the microstructure of precipitates. Thus, the analysis of precipitate is important for material design and process control. The local information of precipitate such as size, shape, and structure, and bulk information such as volume, and number density are important for the characterization of precipitates. Generally, the evaluation of the volume fraction of precipitates is very important for the understanding of the strength of age hardening alloys. However, the quantification of precipitates is also a challenging task. To match the volume fraction of the precipitate and measured strength value, several approaches such as computer simulation, calorimetry measurement, small angle scattering, electrical conductivity measurement, and atomic probe field ion microscopy are explored [14]. Recently three dimensional atom probe (3DAP) tomography is an extremely powerful technique for atomic scale characterization of metals and semiconducting materials. Specifically, 3DAP provides unique and precise results on the nanoscale cluster and precipitate studies because of visualization of individual atom. The morphology and the concentration of the

strengthening phase have been a most important issue to precipitation hardening of aluminum alloys. Thus, the application of the 3DAP to the aging behavior study provides advantages. However, even their superb advantages among the characterization techniques, transmission electron microscopy obviously provide unique characteristic material properties such as crystal structure analysis and orientation relationship with matrix. Thus, the combined investigation with 3DAP and TEM will provide a comprehensive insight into material characterization.

For the identification of the stable and metastable phase, selected area diffraction pattern analysis will distinguish the various precipitates. The stable phases have number of orientation relationships between the precipitates and the matrix. Instead the metastable one has typical orientation relationship. High resolution electron microscopy also provides the information about the lattice parameter or coherency strain between precipitate and matrix. The schematic outline for this research is represented in Fig. 1.3.

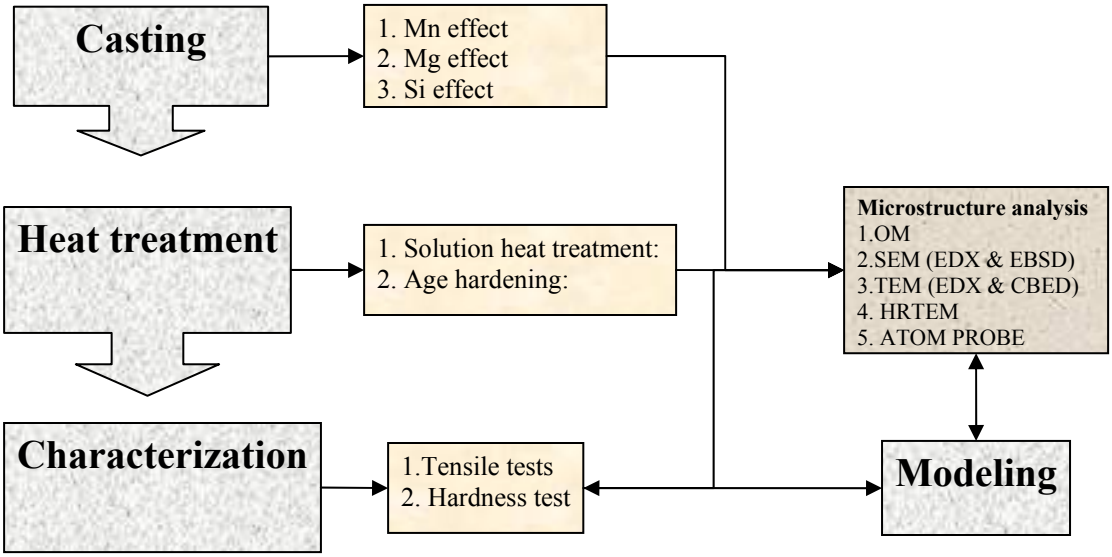

Fig. 1.3 Schematic diagram of the research performed in this study.

1.5 Reference

[1] ASM handbook, “Properties and selection :Nonferrous alloys and special purpose materials”, Vol. 2, OH, 1990.

[2] A.M. Samuel, F.H. Samuel, Metall. Mater. Trans. A, 26A(1995)2359.

[3] L.A. Narayanan, F.H. Samuel, and J.E. Gruzleski, Metall. Mater. Trans. A, 25A(1994)1761.

[4] H. Ye, J. Mater. Eng. and Performance, 12(2003)288.

[5] J.M. Boileau, J.E. Allison, Metall. Mater. Trans. A, 34A(2003)1807.

[6] N. Roy, A.M. Samuel, F.H. Samuel, Metall. Mater. Trans. A, 27A(1996)415.

[7] C.W. Kim,

[8] P.S. Wang, Y.J. Liauh, S.L. Lee, J.C. Lin, Mater. Chem. Physics, 53(1998)195.

[9] F.H. Samuel, P. Ouellet, A.M. Samuel, H.W. Doty, Metall. Mater. Trans. A, 29A(2004)2871.

[10] C.H. Caceres, M.B. Djurdjevic, T.J. Stockell, J.H. Sokolowski, Scripta Mater., 40(1999)631.

[11] P.D. Lee, S. Sridhar, EPD Congress 2002, TMS.

[12] M.N. Binney, D.H. StJohn, A.K. Dahle, J.A. Taylor, E.C. Burhop, P.S. Cooper, Light Metals, 2003, TMS.

[13] R. Jahn, W.T. Donlon, J.E. Allison, Automotive alloys 1999, TMS.

[14] P. Ouellet, F. H. Samuel, J. of Mater. Sci, 34(1999)4671.

[15] S.C. Weakley-Bollin, W. Donlon, C. Wolverton, J.W. Jones, J.E. Allison, Metall. Mater. Trans. A, 35A(2004)2407.

[16] D.J. Chakrabarti, D.E. Laughlin, Prog. Mater. Sci. 49(2004)389.

[17] S. Esmaeili, X. Wang, D.J. Lloyd, and W.J. Poole, Metall. Mater. Trans. A, 34A(1995)751.

[18] L. Lasa, J. M. Rodriguez, J. Mater. Sci. 39(2004)1343.

[19] D. Apelian, S. Shivkumar and G. Sigworth, AFS Trans. 97(1989)727.

[20] A.W. Zhu, J. E.A. Starke Jr, Acta Mater., 47(1999)3263.

[21] J.F. Nie, B.C. Muddle, J. Phase Equil., 19(1998)543.

[22] A.W. Zhu, J. Chen, E.A. Starke Jr, Acta Mater., 48(2000)2239.

[23] C. Wolverton, X.Y. Yan, R. Vijayaraghavan, V. Ozolins, Acta Mater., 50(2002)2187.

[24] M.C. Chaturvedi, D. J. Lloyd and D.W. Chung, J. Mater. Sci., 10(1976)373.

[25] A. Tekin, A. Uguz, J.W. Martin, Mater. Characterization, 25(1990)99.

[26] H.J. Kim, M. Niinomi, Materials Science & Eng. A284(2000)14.

[27] E. Orowan, " Discussion" in Symposium on Internal Stresses in Metal and Alloy, Inst. of Metals, London, 1948, p.451.

[28] R.D. Schueller, F.E. Wawner, A.K. Sachdew, J. of Mater. Sci.,29(1994)239.

[29] J.C. Williams, A.W. Thompson, Strengthening of Metal and Alloys, in "Metallurgical Treaties", Met. Soc. of AIME, Warrendale, PA. 1981.

CHAPTER 2

THE EFFECTS OF Mn ADDITONS ON THE MICROSTRUCTURE AND MECHANICAL PROPERTIES OF Al 319 ALLOYS

2.1 Introduction

In the automotive industry, aluminum-silicon casting alloys are widely used due to their low densities, low cost and acceptable mechanical properties [1]. Among the commercial aluminum-silicon casting alloys, the 319 type (Al-7wt%Si-4wt%Cu) alloys are the most commonly used as cylinder head and engine block materials due to their reasonable heat conductivity, good casting characteristics and acceptable mechanical properties that can be achieved using suitable heat treatments [2-5]. Further enhancements in the strength and ductility of these alloys are frequently accomplished through slight alloying modifications that either cause grain refinement or modify the interdendritic silicon phase [6,7]. It is well known that the intermetallic β-Al_5FeSi phase that forms during the solidification of 319 type alloys is detrimental to the mechanical properties because it is both brittle and exists as thin plates [8]. In general, Mn additions are used to reduce the detrimental effects of the β phase by replacing it with the less-detrimental Chinese script α-$Al_{15}(Fe,Mn)_3Si_2$ phase [7,8]. Other elements, namely, Cr, Co, K and Be have also been reported to cause a similar modification of the β phase to the α phase [9]. While Mn additions result in the replacement of the β phase, they also increase the total amount of intermetallic compounds in the system [8]. Therefore, additions of Mn are typically restricted to only the amounts necessary to effect the β phase modification. In addition, the microstructure change definitely affects the mechanical properties, which are influenced not only by the α phase, but also by other

morphological factors such as porosity, density of intermetallic phase. However, there are few systematic studies on the overall microstructures and mechanical properties as a function of Mn content. In this study, we investigate the role of Mn on the microstructure and properties as a function of Mn content in the 319 type aluminum alloys.

2.2 Experimental Procedures

The alloys used in this study were melted, degassed using pure, dry argon in order to reduce the hydrogen effect, and then cast into a sand mold. In order to increase the cooling rate, an iron chill was used at the end of the mold. The chemical compositions used in this experiment are given in Table 2.1. After casting, the samples were solution heat treated at 488^{o}C for 8 hours followed by quenching in warm (70^{o}C) water and then aged to a T6 condition at 193^{o}C for 8. The area percent of porosity was determined by analyzing the metallographic surfaces and the fracture surfaces of tensile specimens that were analyzed in the scanning electron microscope and optical microscopy. In order to observe the second phases with idea of the 3-D morphologies, deep etching samples were prepared using the HNO_3 acid and methanol. The fracture surface and deep etched samples were observed under the stereomicroscope. The average volume fraction of the intermetallic compounds was determined by image analysis using both optical and scanning electron microscopy (SEM) images.

The cross section taken from the immediately underneath fracture area within 500μm from the fracture surface was also observed.

Table 2.1 Target compositions of the alloys used in this study.

Alloy	Element (wt. %)					
Designation	Al	Si	Cu	Fe	Mg	Mn
Mn02	Bal	6.7	3.75	0.5	0.45	0.02
Mn30	Bal	6.5	3.5	0.5	0.5	0.3
Mn65	Bal	6.5	3.5	0.5	0.5	0.65
Mn85	Bal	6.7	3.75	0.5	0.45	0.85

2.3 Results and Discussion

2.3.1 Microstructural Analysis

The microstructures of the four different samples used in these experiments are comprised of aluminum dendrites, eutectic silicon, iron-, copper- and magnesium-containing intermetallic phases, and porosity (Fig.2.1). The microstructures of each alloy demonstrate that, while the aluminum dendrites have little variation in size and dendrite arm spacing (DAS), the interdendritic regions display considerable variations in the size, shape, and distribution of the intermetallic phases as well as the amount of porosity. For example, the microstructure of the Mn02 sample in Fig. 2.2(a) and the Mn85 sample in Fig. 2.2(d) contain relatively coarse interdendritic structures compared to the alloys with intermediate Mn contents (Fig. 2.2(b) and (c)). Scanning electron microscopy (SEM) images of these alloys (Fig.2.3) show two different shape of iron-containing intermetallic phase where it can be seen that the majority iron-containing phase in the Mn02 samples is the needle or plate-shaped β-phase whereas the majority iron-containing phase in the higher Mn alloys is the Chinese script α phase. Cleary, the intermediate Mn30 specimen contains both β needles/plates and Chinese script α phase. Finally, there are iron-containing polyhedral type particles which have essentially the same composition as the Chinese script α phase. The complex polyhedral intermetallic phases have been reported in certain Mn-modified alloys and referred to as “sludge”, and have been shown to have a detrimental effect on the mechanical properties [10]. In this study, the coarse polyhedral was observed only in the Mn85 sample. Both the α and β phases were observed in the Mn30 sample indicating that the Mn concentration was insufficient to completely eliminate the β phase. The structure of the α phase is bcc ($Im\bar{3}$ space

Fig.2.1 SEM microstructures observed in the 319 type aluminum alloys after T6 heat treatment. (a) Mn02, (b) Mn30, (c) Mn65, and (d) Mn85 sample.

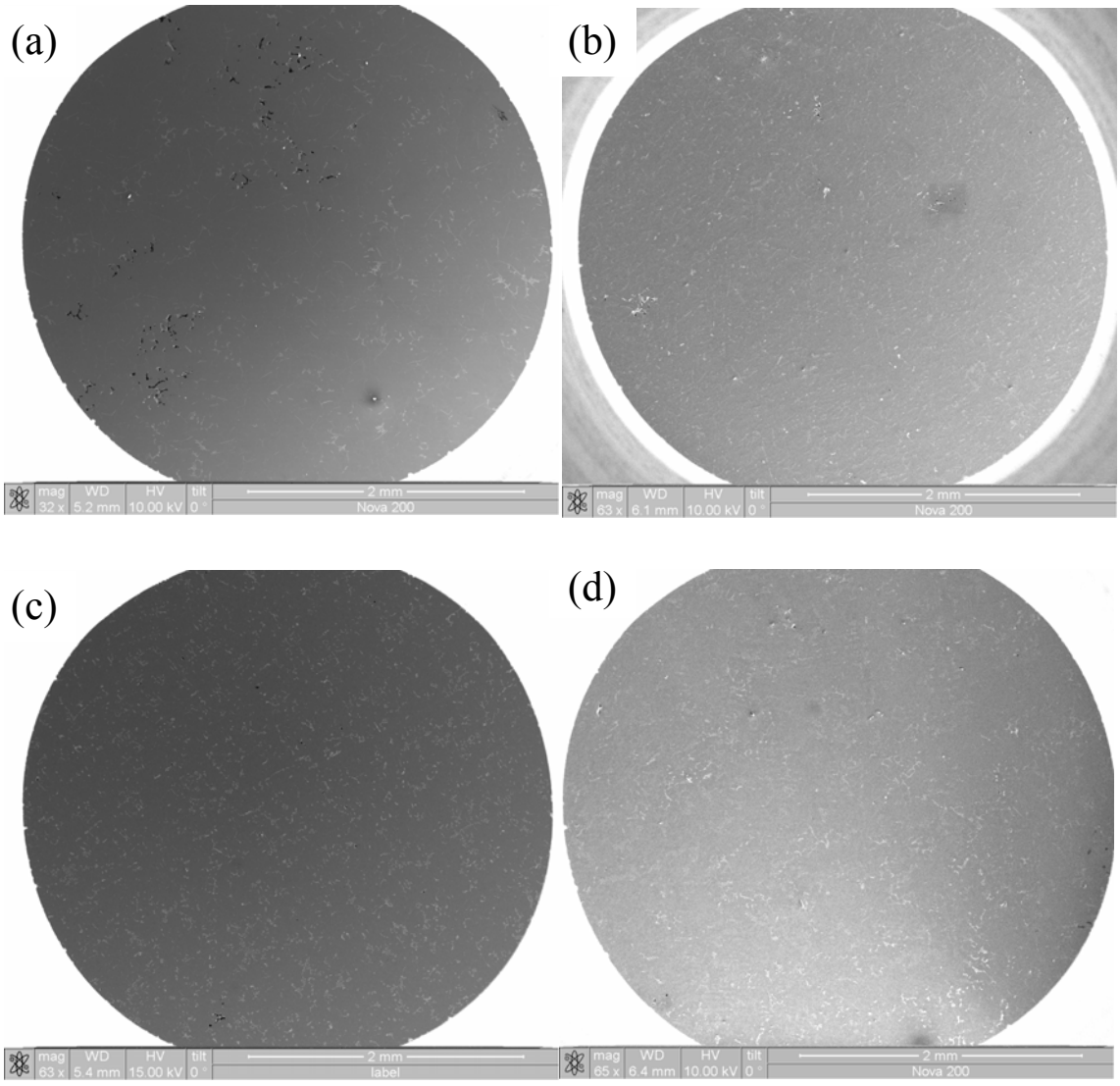

Fig. 2.2 Optical microstructures observed in the 319 type aluminum alloys after T6 heat treatment. (a) Mn02, (b) Mn30, (c) Mn65, and (d) Mn85 sample.

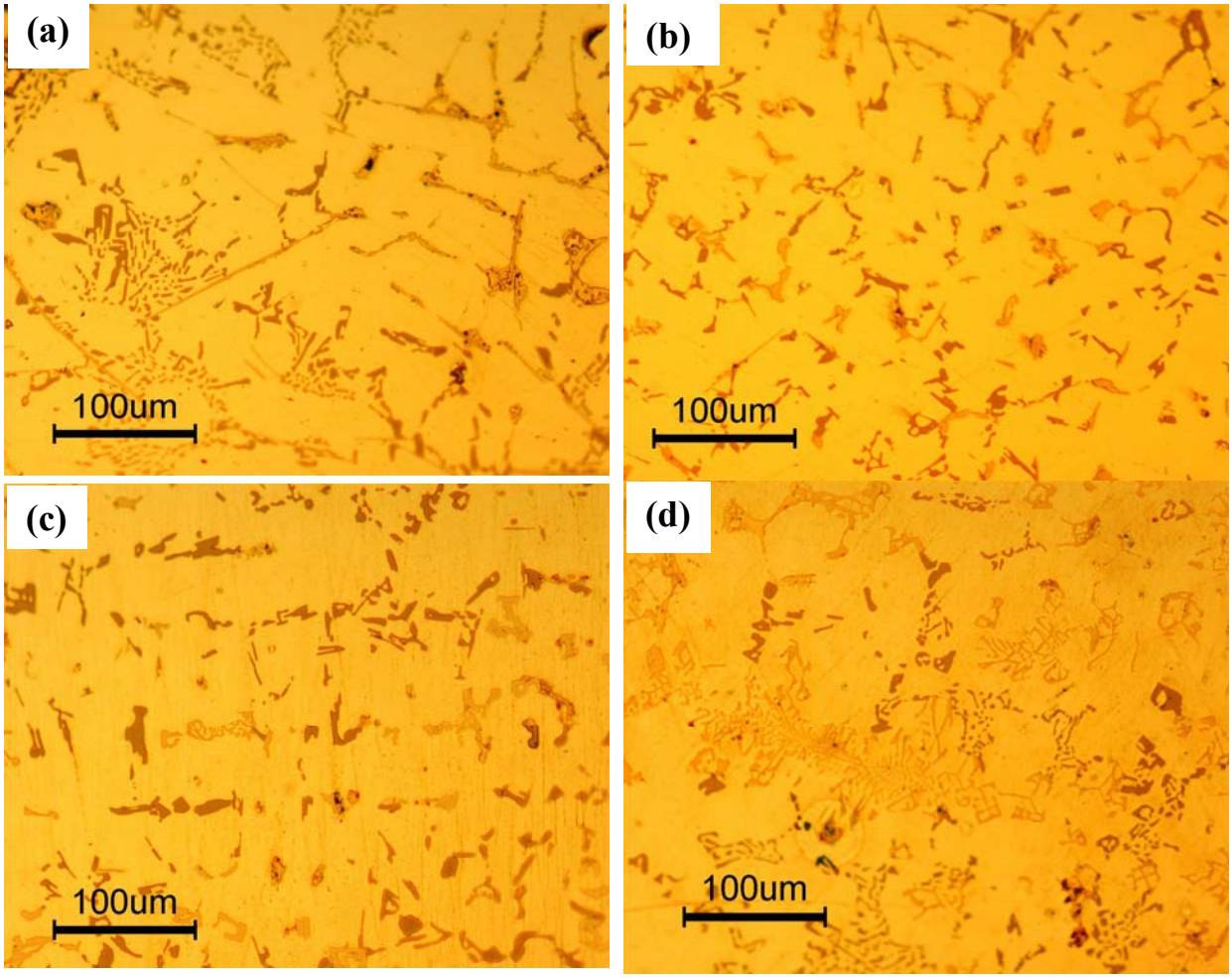

Fig.2.3 SEM microstructures observed in the 319 type aluminum alloys after T6 heat treatment. (a) Mn02, (b) Mn30, (c) Mn65, and (d) Mn85 sample showing the α, β intermetallic phases.

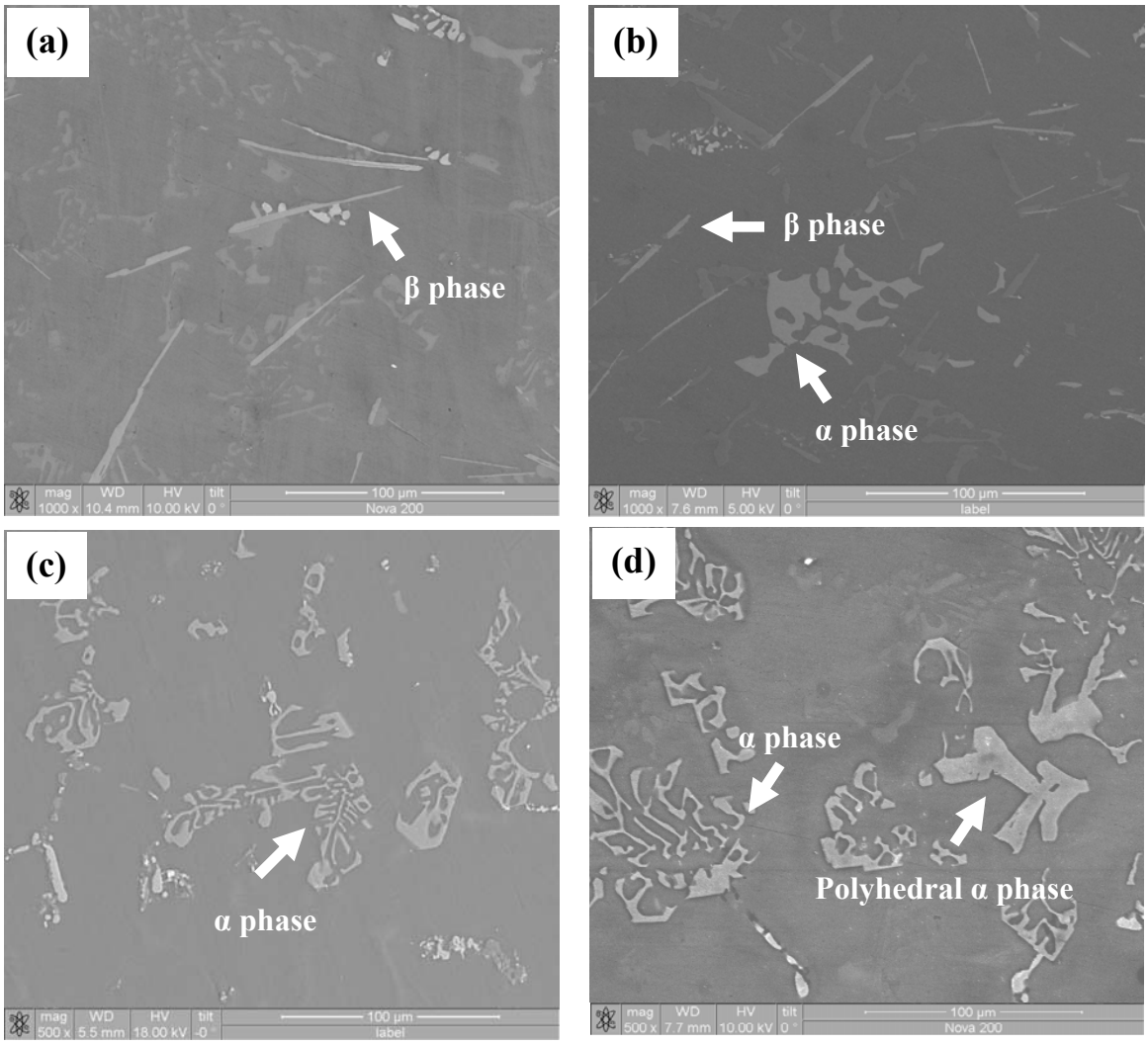

group) with a large unit cell, a=1.2nm, whereas the β phase is orthorhombic. A detailed study of the crystallographic features of both the α and β phases will be presented in chapter 3.

The average compositions of the α and β phases measured by EDX analysis in the SEM are presented in Table 2.2. The compositions of the β particles detected in the Mn02 and Mn30 have approximately the same ratio of Al:Fe:Si, namely, 5:1:1. The compositions of the α phases observed in the Mn30, Mn65, and Mn85 samples also have similar ratio of Al:[Fe,Mn]:Si, 13:4:2.

Table 2.2 Average EDX results of the different iron intermetallic phases (at. %).

	Al	Si	Mn	Fe	Cu, Mg
β particles in Mn02 sample	65 ± 1.8	16 ± 2.4	0 ± 0.2	15 ± 0.8	bal
β particles in Mn30 sample	64 ± 2.1	12 ± 3.3	2 ± 1.1	13 ± 1.7	bal
α particles in Mn30 sample	64 ± 5.1	11 ± 0.6	11 ± 3	9 ± 1.4	bal
α particles in Mn65 sample	67 ± 0.8	13 ± 0.3	10 ± 0.5	8 ± 0.2	bal
α particles in Mn85 sample (Chinese script)	64 ± 4.2	9 ± 1.2	13± 0.1	10 ± 1.9	bal
α particles in Mn85 sample (Polyhedral)	66	11	12	9	bal

Significantly, the Mn/Fe ratio in the α phase is similar in the Mn30 and Mn65 and Mn85 samples and is approximately 1.2. If it is assumed that all of the Mn and Fe are tied up in these intermetallic phases, it is possible to use the measured Mn/Fe ratio in the α phase and the Fe content in the alloy to estimate the amount of Mn required for complete modification of the β phase. For example, given that the iron content in these alloys is ~0.5 wt. % and that the atomic weights of Fe and Mn are similar, then the amount of Mn required to completely modify the β phase should be approximately 0.6 wt. %, consistent with the experimental observations. Excess Mn beyond that necessary to eliminate the β phase is expected to lead to an even greater volume fraction of the α phase, which should be detrimental to mechanical properties due to (1) its expected brittle nature and (2) the porosity frequently associated with this phase (Fig. 2.4). It is noted that, even though the porosity associated with the β phase is usually larger than that associated with the α phase, the additional volume fraction of α phase observed with increasing Mn does result in a greater overall volume fraction of porosity. Thus, the pore fraction could be minimized by modification of the β phase. The total fraction of porosity observed after the T6 samples in the metallographic surfaces (Fig.2.1) is summarized in the Table 2.3.

Table 2.3 The area percent of porosity measured from the metallographic and fracture surfaces of the four alloys.

	Porosity from the metallographic surface in Fig.2.1	Porosity (recessed area) in the fracture surface from Fig.2.8
Mn02	0.5	20
Mn30	0.1	18
Mn65	0.1	12
Mn85	0.2	17

Deep etching was used in an attempt to get a better idea of the 3-D morphologies of the intermetallic phases in the various alloys (Fig.2.5). Using quantitative stereology, the total volume fraction of intermetallic phases in the alloys appears to increase linearly with Mn concentration. The measured volume densities of the various secondary phases are summarized in Table 2.4. As expected, the total amounts of the intermetallic phases increases with Mn concentration, while the amount of Si remains approximately constant.

Table 2.4 The volume percent of iron containing intermetallic and Si phases.

	α phase	β phase	Si
Mn02	0.1	1.7	7.1
Mn30	0.5	1.5	7.1
Mn65	2.9	0	7.2
Mn85	3.4	0	7.5

Several previous researchers have attempted to quantify the total amount of intermetallic compounds. For example, Roy, et al. [4] observed three different iron-containing intermetallics in cast alloys containing Mn, namely, (1) the needle-like β phase, (2) the Chinese script α phase, and (3) the polyhedral α phase. Ashtari et al. suggested that additions of Mn or Mn plus Sr caused (1) refinement of the β phase and (2) formation of the α phase instead of the β phase [11]. Their findings are consistent with the present results. The relative volume fractions of the iron-containing intermetallic phases are also found to depend on the cooling rates where faster cooling produces more of the α phase compared with the β phase. In the present study, the relative amounts of these phases were observed to depend mostly on the Mn/Fe ratio with a slight dependence on solidification rate. Specifically, in the Mn02 alloy, only the β phase was observed, whereas the polyhedral α phase was observed only in the Mn85 sample. Therefore, it is important to control the Mn/Fe ratio in order to completely eliminate the β phase and to minimize the total amount of the α phase.

Fig.2.4 Micrographs showing the pore observed around the β phase from Mn02 (a), and α phase from Mn65 (b).

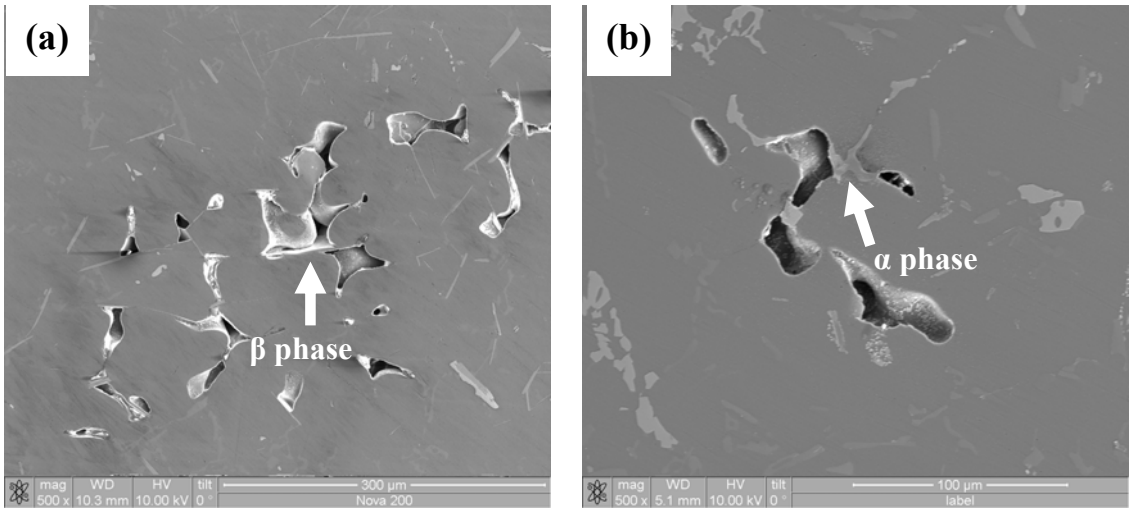

Fig.2.5 Micrographs showing the Si, α, and β phase in the deep etched samples, (a) Mn02, (b) Mn30, (c) Mn65, and (d) Mn85 sample after T6 heat treatment.

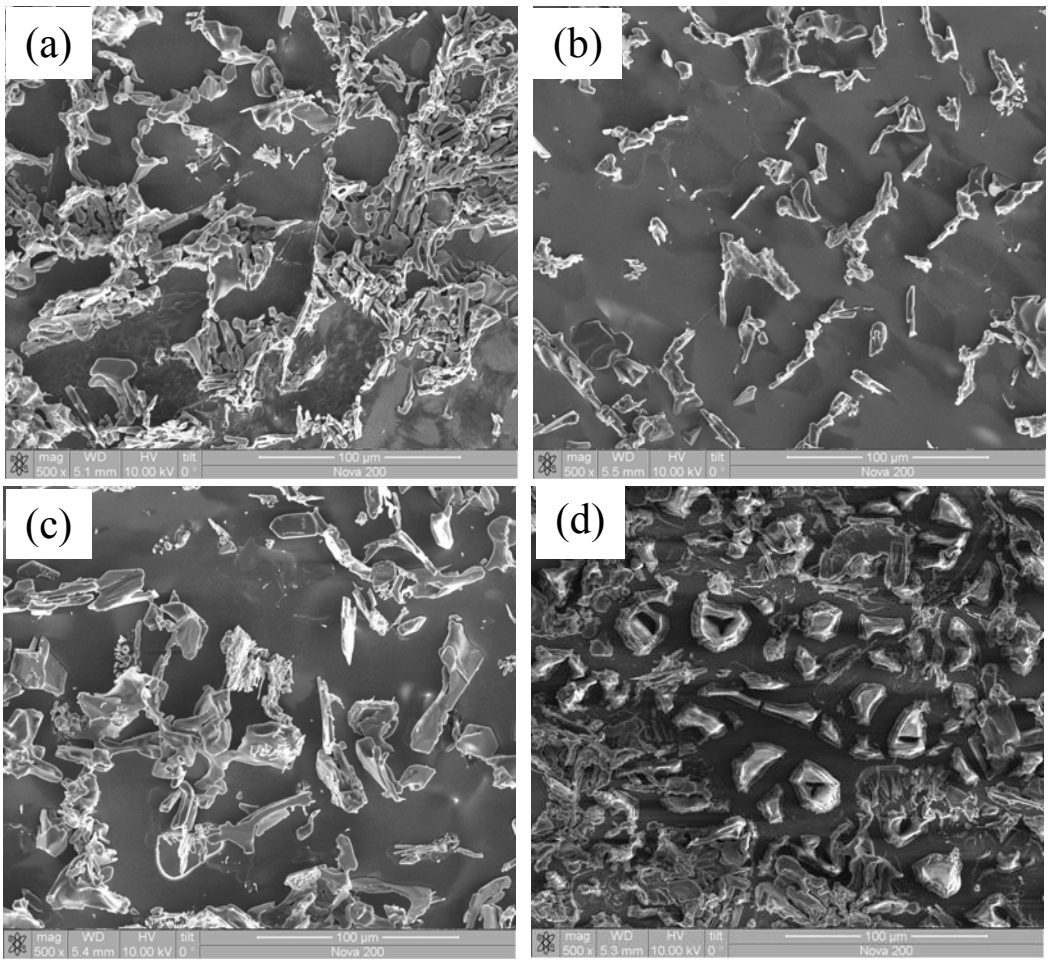

3.2 Fractography

It is well known that porosity reduces both strength and ductility in castings and this applies to Alloy 319 as well (see Li, et al. [12]). Consequently, understanding and controlling porosity is clearly beneficial. In the present study, evidence of cracks emanating from porosity was observed by polishing the surfaces of the tensile specimens adjacent to the Fig. 2.6(b). Clearly, such porosity not only provides stress concentration sites but also easy paths for crack propagation. Silicon particles and the β phase are known to serve as crack nucleation sites in Al-Si alloys [9].

In the present study, cracks were observed to initiate around the silicon phases and propagated through the silicon phases in the gage surfaces of the samples just below the fracture surface (Fig. 2.6c). SEM images and corresponding energy dispersive spectrometers (EDS) map of the fracture surfaces of the Mn02 and Mn85 samples (Fig. 2.7) reveal several interesting features. First of all, it is clear that the smooth surfaces bounding the pores are the Al dendrites. The rougher regions, however, display the various intermetallics consistent with them being the regions of preferred crack propagation due to their brittle nature. Specifically, in the Mn02 sample (Fig. 2.7a,b), it is clear that the plates (red) were involved in the fracture as were the Si (blue) and Al_2Cu (cyan) phases. In the high Mn alloy (Fig. 2.7c,d), there was no β phase as expected. However, there were regions of Si, Al_2Cu, the Mg-rich phase and the (Fe+Mn) phase (gold). Clearly, the nature and distribution of the phase is expected to be less detrimental to the mechanical properties. From the SEM images and EDS maps, it appears that there is more porosity associated wit the phase in the Mn02sample. We can see the β is more effective to nucleate the large pore. In addition,

Fig.2.6 Micrographs showing the fracture surface (a), crack initiation and propagation along the pore (b), and silicon particles (c): dotted arrow shows cross sectional area (a), and straight arrows (b, c) represent the cracks in the metallographic gage surface just below the fracture surfaces in (a).

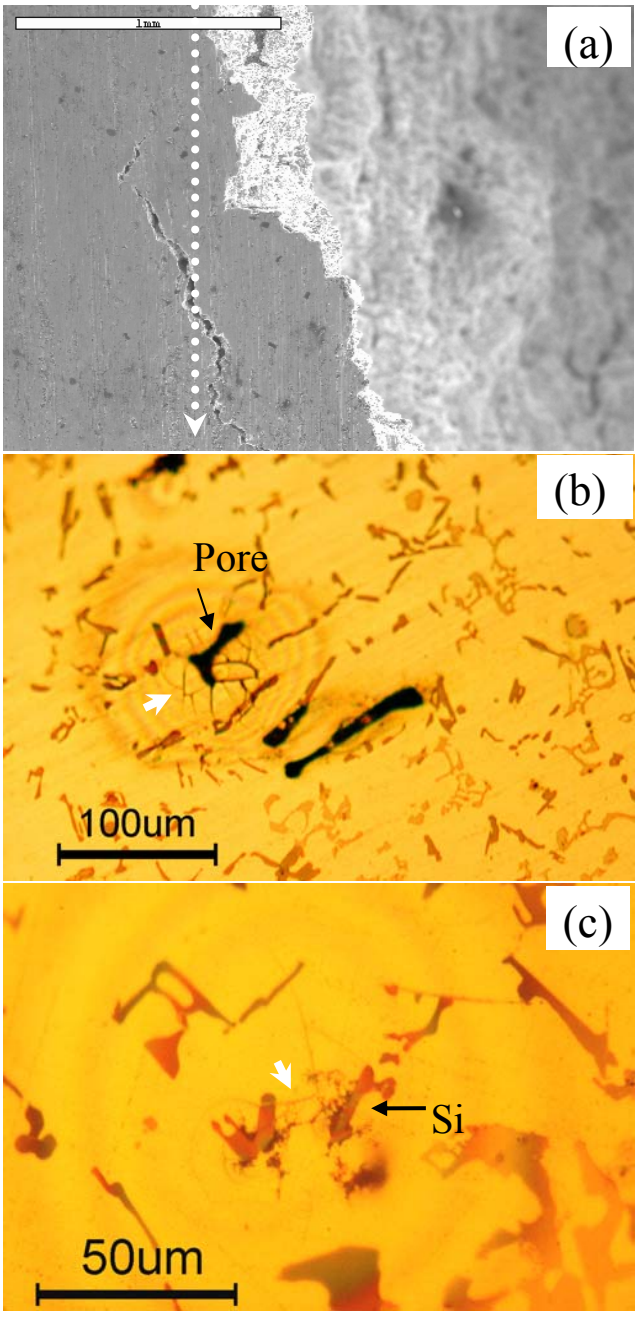

Fig.2.7 SEM images and EDS maps of the fracture surfaces of the Mn02 sample (a) and (b), and the Mn85 sample (c) and (d).

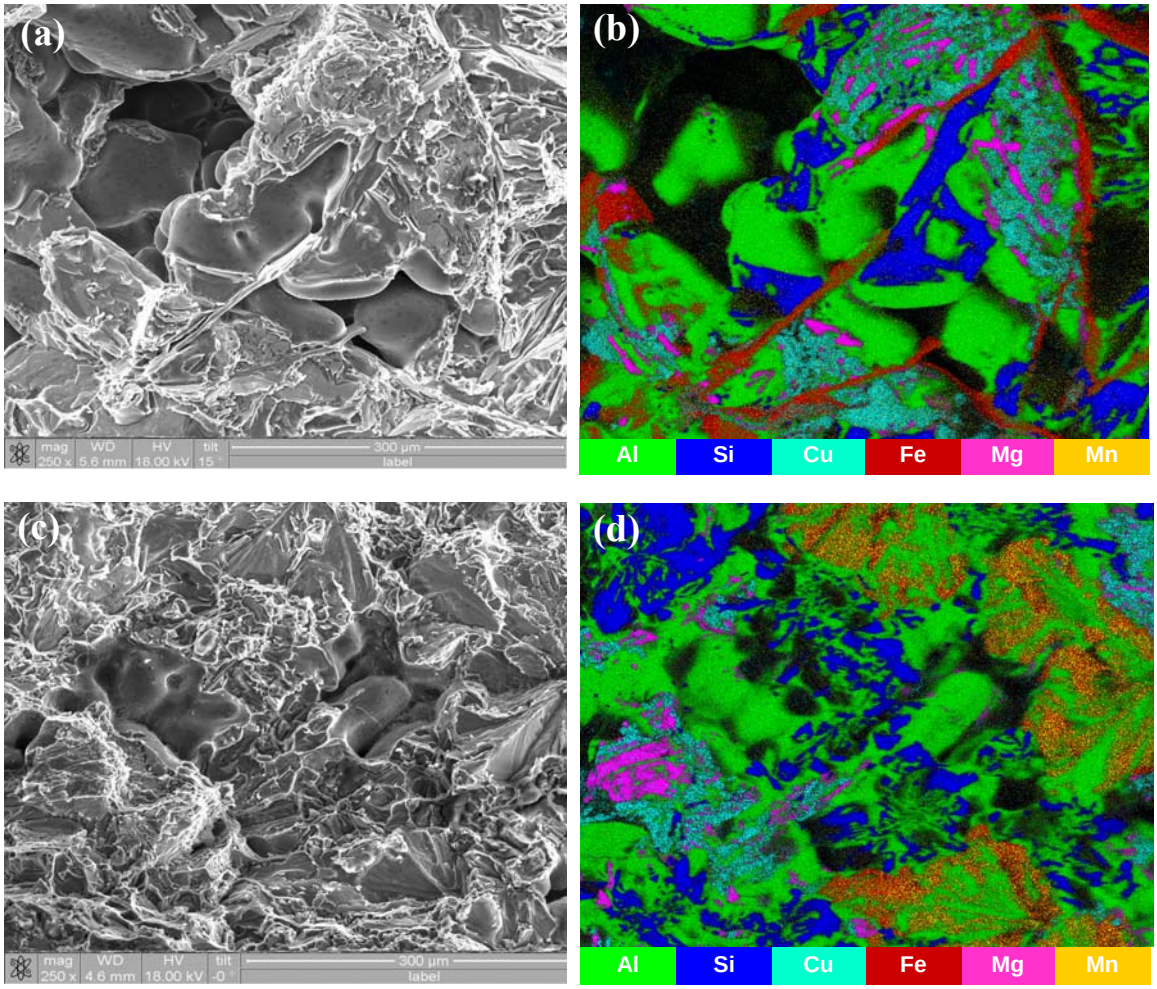

it appears that the Si may have preferentially nucleated on the α phase (Fig 2.7(b)) and implies that α intermetallic phase may be a possible nucleation site for eutectic Si. For the Mn85 alloy, the Si phase appears somewhat refined compared with that in the Mn02 alloy implying that the Mn also affects the Si morphology.

There are some reports on the relationship between porosity and other casting defects on mechanical properties [13-15]. Several investigators reported that the maximum pore size appears to be the dominant factor in fatigue life as opposed to the total volume fraction of porosity. However, it is difficult to determine the relationship between metallographic pore size and fatigue data [5]. Porosity measurements are generally carried out by image analysis from direct measurements on metallographic surfaces; such measurements give average porosity from locally limited areas and may not reflect the magnitude of the effects of porosity on mechanical properties. However, the porosity associated with the fracture surfaces should provide more relevant information related to its effect on tensile properties as reported by Surappa, et al. [13] and Caceres and Selling [14]. Instead metallographic surface is the result of an arbitrary two-dimensional slice. In order to quantify the porosity or defects on the fracture surface, back-scattered electron topography study were carried out combined with secondary electron images in Fig. 2.8. As can be seen, the regions that appear smooth and, in some cases, slightly recessed are the surfaces bounding the pores whereas the rougher surfaces are those that underwent fracture. Clearly, these rougher surface regions that separate the exposed porosity appear to have fractured by brittle cleavage for the most part. From image analysis, the smallest recessed areas associated with porosity occurred in the case of the Mn65 sample. The results of the total area porosity

are represented in Table 2.3. It is observed that trace of convergence of fracture propagation marks in the Mn65 sample in Fig. 2.8(c). It indicates that crack has initiated on certain point and continued to favorable direction with resistance of propagation. Other 3 samples show no evidence of resistance of crack propagation, instead there are multiple deep cavity areas. It is likely due to multiple points of crack initiation inducing abrupt fracture at a time. We found that low Mn and high Mn sample have large area of recessed area compared to Mn30 and Mn65 samples. It is plausible to match with the total volume of α and β intermetallic phases. The recess area in the case of Mn02 is the largest even the total volume of intermetallic phase is smallest, which imply that β is most effective to nucleate the shrinkage pore by blocking the melt feeding. It is also likely to occur of blocking of melt by α intermetallic phase, which also cause of porosity increase. The evidence of nucleation of pore due to α and β phase are already shown in the Fig. 2.4 and Fig. 2.7. Thus, the pore should be most detrimental effect on the tensile properties especially in elongation, and can be reduced by removing the source of iron intermetallic phases. Among α and β phases, β is more harmful for the formation of pore. It might be from the morphological shape. Plate like shape is effective to block the molten metal than Chinese script α phase. We found the β phases inside the aluminum dendrite, which are formed prior to the interdendritic α phase, thus β is more harmful compared to α phase.

Fig.2.8 Secondary electron (SE) and backscattered electron (BE) images on the fracture surface. (a) Mn02, (b) Mn30, (c) Mn65, and (d) Mn85 sample.

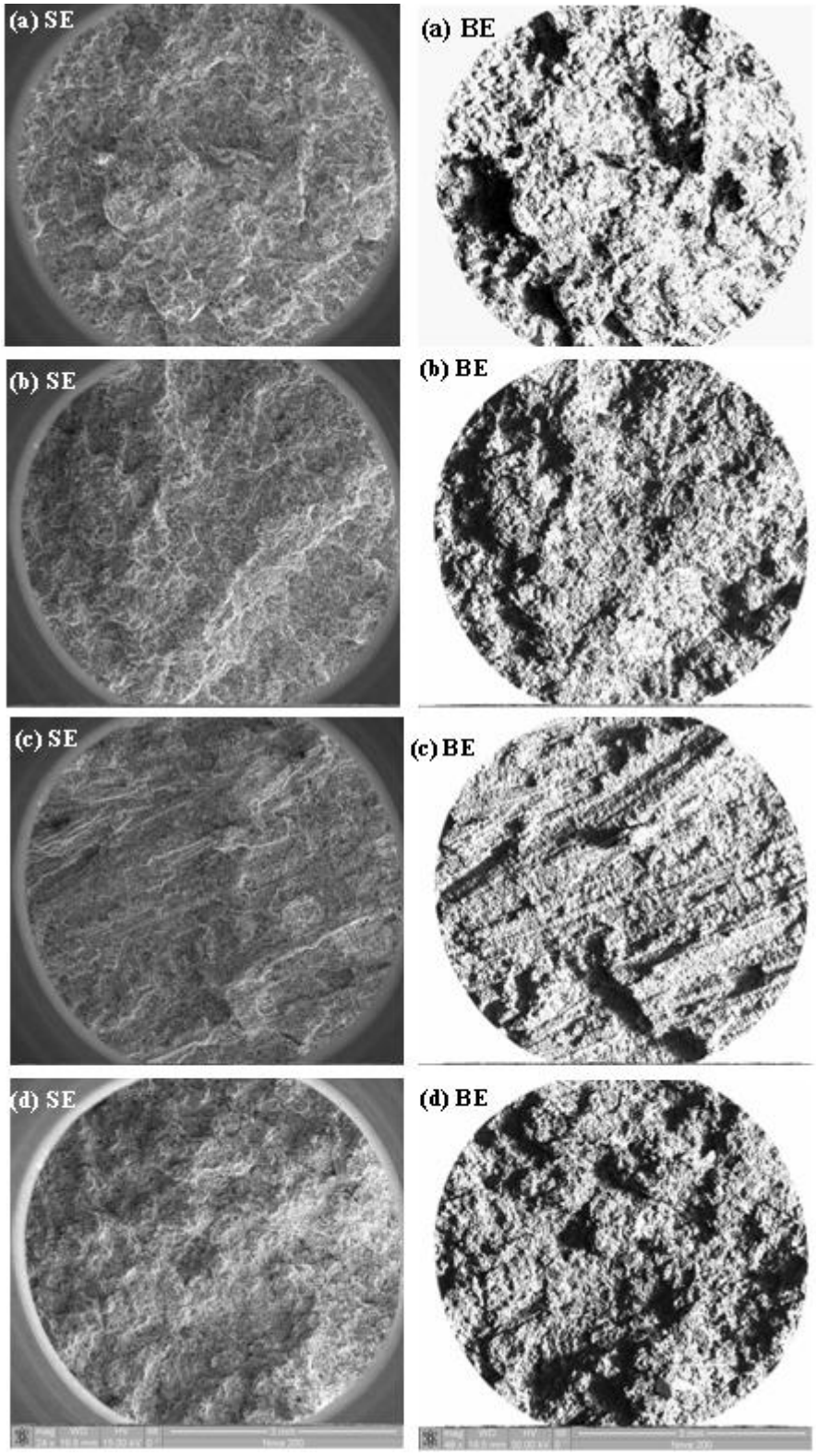

2.3.3 Mechanical Properties

The yield strength (YS) and ultimate tensile strength (UTS) of the 319 aluminum alloys as a function of Mn content are shown in Fig. 2.9. The strength of as cast condition in 4 different alloys has the similar values. In general, the tensile properties of 319 aluminum alloys are heavily dependent on the DAS structure, which is a function of cooling rate [12]. The addition of Mn to these alloys does not change the DAS structure significantly (Fig. 2.1 and 2.2). An increase in both yield and ultimate strength is observed in the T6 heat treated samples. The 319 aluminum alloys are heat treatable in order to enhance the strength by precipitation of the θ'-Al_2Cu phases. At the peak aging condition, the size of the θ' phase is around 100nm and aligned with <001> cube axis in the matrix. A detailed study of the effects of microstructure and crystal structure on the hardening precipitates will be discussed in the following chapter. The properties of precipitates are influenced by the composition and heat treatment conditions in this alloy [16]. Under the T6 condition, the size and distribution of the θ' precipitates do not show a significant difference in the 4 different alloys; this suggests that the yield strength is less dependent on the Mn composition. However, the UTS value increases with Mn content up to 0.65% and then, decreases slightly. Compared to the YS values, the UTS values are more sensitive to the variation of the Mn content. Li reported that the DAS, iron-containing intermetallic phases, and eutectic Si structure will generally affect the UTS value [12].

It was found that the dendrite structure and Si structure of the 4 different samples are not so significantly changed as seen in Fig. 2.1 and 2.2. Rather the morphological change and volume fraction of iron containing intermetallic phases show significant

variation as a function of Mn content. In addition, plate-like β phase nucleate the pores more seriously by blocking the melt flow than pores caused by Chinese script α phase, which is also employed to produce the pores. This is clearly confirmed by fracture surface in Fig. 2.4 and Fig. 2.7. The UTS values in the T6 samples are in inverse proportion to recessed area measured from the fracture surface in Fig. 2.8. It is more accurate to predict the relationship between the tensile strength and microstructural analysis.

Li et al. [12] reported that dispersion of iron containing intermetallic phase will improve the UTS in the as-cast condition. However, we could not find the significant relation with strength and iron intermetallic phases.

As can be seen in Fig.2.10, the ductility of these alloys in the T6 condition is strongly dependent on Mn concentration and, as already discussed is observed to increase with Mn concentration up to 0.65% and then decrease as the excess amount leads to increases in the total volume fraction of the α phase. As already pointed out, the plate shaped b phase is detrimental for two reasons – first, the shape and brittleness of this phase and second, the increased porosity associate with this phase. of possible explanation of detrimental effect of β phase on the low ductility is nucleation of shrinkage pore. We propose that shrinkage pore due to blocking of melt flow during solidification is reasonable. Although both the β and α phases can induce the shrinkage pores as shown in Fig.2.4, the β phases are more critical because its inherent plate shape morphology is more harmful than Chinese script α phase. The recessed pore areas measured from the fracture surface in Fig. 2.8 using the back scattered images are summarized in the table 2.3. The porosity of fracture surface in Mn02 sample is

Fig.2.9 Yield strength (YS), and ultimate tensile strength (UTS) as a function of Mn contents in the 319 type aluminum alloys.

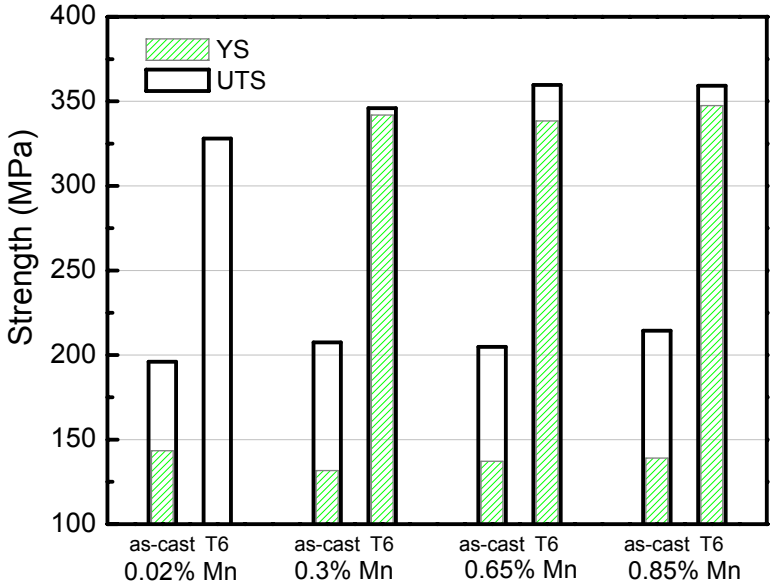

Fig.2.10 Ductility as a function of Mn content in the 319 type aluminum alloys after the T6 heat treatment.

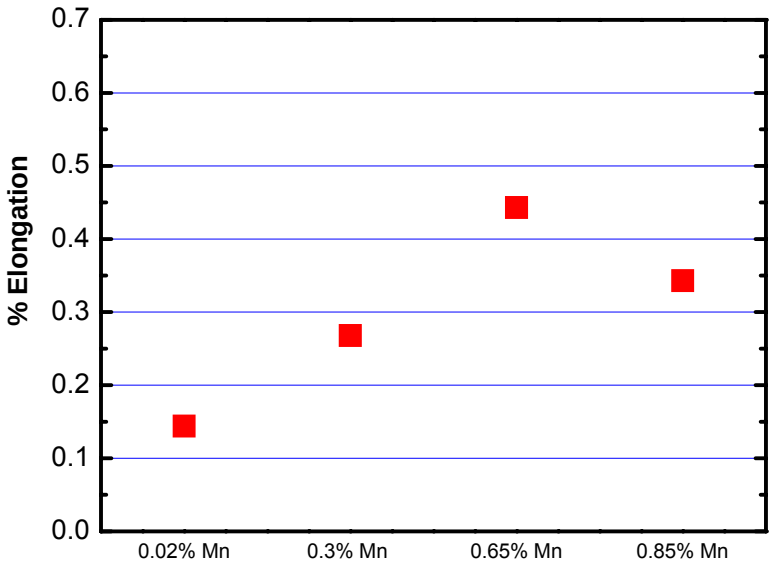

largest and Mn30 and second largest. Mn65 case has the smallest porosity in the fracture surface. Mn85 sample has the largest volume of iron intermetallic phase, but all are α phase which will slightly increase the total volume of pore.

There are critical correlations between the UTS and % elongation as shown in Figs. 2.9 and 2.10. The change in strength as a function of Mn content follows the ductility change. When the ductility increases, the UTS also increases and vice versa. There are a lot of factors to determine the mechanical property and morphological changes when Mn is added. In our research we find the area percent of casting defect bounding iron intermetallic phase and pore and silicon appeared in the fracture surface will explain the more exactly. This might result from the morphological characteristics of iron intermetallic phases. The addition of Mn will increase the ductility up to 1.2 Mn/Fe ratio and no more effective on the modification after that.

The microstructure and mechanical properties of 319 aluminum casting alloys have been examined as a function of Mn content. It is shown that, as the Mn content is increased up to 0.65 wt. pct. (corresponding to an Mn/Fe ratio of ~1.2) in the baseline alloy (Al-7wt%Si-3.8wt%Cu-0.5wt%Fe), the plate-like β-Al_5FeSi intermetallic phase is completely modified to the Chinese script α-$Al_{13}(Fe,Mn)_4Si_2$ phase resulting in improved tensile properties. Excess amounts of Mn, however, deteriorate the mechanical properties by increasing the total amount of intermetallic phase. The UTS values in the T6 samples are in inverse proportion to recess area measured from the fracture surface. The UTS and % elongation are slight increased, as the amount of Mn contents increase in the T6 heat treated sample, while the YS is less dependent on the Mn variation.

2.4 Reference

[1] H. Ye, J. Mater. Eng. and Performance, 12(2003)288.

[2] A.M. Samuel, F.H. Samuel, Metall. Mater. Trans. A, 26A(1995)2359.

[3] G.A. Edwards. G.K. Sigworth, C.H. Caceres, D.H. St.John, J. Barresi, Modern Casting, 105(1997)809.

[4] N. Roy, A.M. Samuel, F.H. Samuel, Metall. Mater. Trans. A, 27A(1996)415.

[5] J.M. Boileau, J.E. Allison, Metall. Mater. Trans. A, 34A(2003)1807.

[6] L. Liu, A.M. Samuel, F. H. Samuel, H.W. Doty and S. Valtierra, Int. J Cast Metal, 16(2003)397.

[7] L.A. Narayanan, F.H. Samuel, J.E. Gruzleski, Metall. Mater. Trans. A, 25A(1994)1761.

[8] L. Lu, A.K. Dahle, Metall. Mater. Trans. A, 36(2005)819.

[9] S. Murali, K.S. Raman, K.S.S. Murthy, Cast Metals, 4(1994)189.

[10] S.G. Shabestari, Mater. Sci. Eng. A, 383(2004)289.

[11] P. Ashitari, H. Tezuka, T. Sato, T. Sato, Mater. Trans. 44(2003)2611.

[12] Z. Li, A.M. Samuel, F.H. Samuel, C. Ravindran, S. Valtierra, H.W. Doty, Mater. Sci. & Eng. A, 367(2004)96.

[13] M.K. Surappa, E. Blank, J.C. Jaquet, Scripta Metall., 20(1986)1281.

[14] C.H. Caceres, B.I. Selling, Mater. Sci. & Eng. A, 220(1996)109.

[15] M. Dash, M. Makhlouf, J. Light Metals, 1(2001)251.

[16] J.Y. Hwang, H.W. Doty, M.J. Kaufman, TMS letters, 3(2006)39.

CHAPTER 3

CRYSTALLOGRAPHIC STUDIES ON THE IRON CONTAINING INTERMETALLIC PHASES IN THE 319 TYPE ALUMINUM CASTING ALLOYS

3.1 Introduction

Al-Si alloys are widely used to produce a large number of casting components especially for the automotive industry. Type 319 Al alloys (Al-Si-Cu) are commonly used as engine blocks and heads due to their good castability and acceptable mechanical properties at both ambient and slightly elevated temperatures after appropriate heat treatments [1]. These alloys invariably contain iron as an impurity, which leads to the formation of various intermetallic compounds, the nature of which depends on the overall composition of the alloy. These compounds tend to be brittle in nature and thereby degrade the mechanical properties; this is especially true for the β-Al Fe Si phase, which tends to form needle or plate-shaped morphologies. Significant research has been conducted to reduce the negative effects of iron impurities by modifying the undesirable β phase to the less-harmful α phase, which has a cubic structure and forms in a Chinese script morphology [2-11].

Given the different and characteristic morphologies of these phases, they are usually easily identified in optical images. However, this does not provide information about composition and structure. Backscattered electron imaging in the SEM along with qualitative EDS analysis [8] are sometimes used to confirm the optical characterization. Even so, the identification of these phases, their crystal structures, morphologies and orientation relationships with the Al matrix has been the subject of controversy. For example, the β phase has been identified as monoclinic, orthorhombic and tetragonal,

all closely related given that (1) two of the lattice parameters in the monoclinic and orthorhombic phases are similar and (2) the unique angle in the monoclinic phase is close to reported to be between 90 and 91 degrees. The α phase, on the other hand, is usually identified as having a cubic Im3 structure with a lattice parameter of ~1.26nm. Unfortunately, the structure of this higher symmetry phase is complex leading to EBSD patterns (SEM) and Kikuchi patterns (TEM) that are also complex and frequently misidentified in the literature [12-13].

The reason for this will become clear in the present study. Unfortunately, in only a few of these studies have the iron intermetallic compounds in the 319 alloys been identified using crystallographic information. Rather, the phase identification in these studies has been based on both morphological and composition data, the latter frequently obtained by EDS results. The crystallographic information of the iron intermetallic phases has usually been studied in wrought Al alloys as well as in cast 356 (Al-Si-Mg) alloys. Unfortunately, there have been several recent reports of the structure of these phases using electron backscattered diffraction in the SEM that appear to be incorrect in their indexing [12], while one of the recent TEM studies has reported a tetragonal β phase that is closely related to the orthorhombic structure [14]. Based on these inconsistencies and the desire to be able to quickly and unequivocally identify these phases in Al alloys of this type, this study was initiated.

In the present study, the iron-containing α and β. phases were characterized using both electron backscatter diffraction (EBSD) in the scanning electron microscope (SEM) and convergent beam electron diffraction (CBED) and selected area diffraction (SAD) in the transmission electron microscope (TEM). The results are then discussed

and compared to previous studies in an effort to clarify the nature of these phases and their identification in these commercial alloys.

3.2 Experimental Procedures

The compositions of the alloys used in this study are given in Table 3.1 and were provided by GM Powertrain, Metal Cast Inc. The samples were cast in sand molds and then subjected to solution treating and aging treatments. The details of the casting procedures and heat treatments for these alloys have been described in the chapter 2. For the metallographic and EBSD studies, the as-received alloys were cut with a low speed diamond saw, mounted in epoxy, polished to 30 μm using silicon carbide paper and final polishing was performed with a 0.05 μm alumina suspension. The as-polished samples were examined using an FEI Nova Nano200, dual beam focused ion beam/scanning electron microscope system equipped with a TSL EBSD system. For the TEM study, thin (~100 μm) samples were punched into 3mm disks and then electrolytically polished using a twin jet electropolishing system with 33 vol.% HNO_3 in methanol at -20°C. Because some of the phases in the alloys were not electrolytically attacked (e.g., silicon) the as-electropolished samples were subjected to short exposure in a Gatan model 651, precision ion polishing system at 5KV for 30 minutes in order to produce more uniformly thinned regions. A Philips 420 transmission electron microscope equipped with an EDAX, EDS detector was utilized for the CBED and SAD pattern analyses. The camera length was calibrated using pure silicon as a standard.

3.3 Results and Discussion

Typical microstructures of the iron-containing intermetallic phases in the cast aluminum alloys are shown in Fig. 3.1. The phases of interest appeared in two different morphologies, namely, a Chinese script-like morphology (Fig.3.1(a)) and as thin plates (Fig.3.1(b)). The plate-like phases often appeared as long needles in the two-dimensional metallographic sections. However, it is apparent from observations of this phase on fracture surfaces and adjacent to shrinkage porosity that they are consistently plates rather than needles. Thus it implies that networks of this phase may block the melt flow during solidification and result in stress concentrations which lead to premature fracture. It has also been suggested that the plate-shaped intermetallic phase is a nucleation site for eutectic silicon and gas porosity [5]. On the other hand, the Fe-containing phase in the Chinese script regions has a morphology less likely to be as detrimental to the properties. In the previous chapter 2, we addressed that the plate-shaped particles were observed in the Mn-free samples, while the Chinese script intermetallics were observed in the Mn-containing samples regardless of whether the samples were chilled or unchilled during the casting process. The recent literature by Kral et al. [12] suggested that Mn additions had no influence on the modification of the Fe-containing intermetallic, in contrast to both the present results and those of other investigators [9.10].

The approximate compositions of these phases were determined using energy dispersive spectroscopy (EDS); the values given in Table 3.2 are average values based on measurements on more than ten different particles in both the SEM and TEM. The EDS results indicate that the Chinese script phase is indeed stabilized by Mn whereas

Table 3.1 Target compositions of the 319 alloys used in this study.

	Al	Si	Cu	Mg	Fe	Mn
1	Bal.	6.5	3.5	0.5	0.5	0.65
2	Bal	6.7	3.75	0.45	0.5	0.02

Table 3.2 Measured compositions of β and α phases measured by EDS in both the SEM and TEM (at.%).

	Al	Si	Cu	Fe	Mn	Mg
β phase (SEM)	66.9±3.8	16.4±3.4	2.7±0.5	12.7±0.8	0	1.1±0.5
α phase (SEM)	66.8±2.7	13.3±0.3	1.7±0.7	8.3±0.2	10.2±0.5	0.5±0.5
β phase (TEM)	67.1±2.3	16.6±4	0.6±0.2	13.4±2	0	2.2±0.4
α phase (TEM)	61.4±6.7	16.5±5.8	2.6±1.1	8.0±1.7	10.3±2.5	1.9±0.7

Fig.3.1 Microstructures of two different types of iron intermetallic phases in the Type 319 aluminum alloy: (a) Chinese script α-Al[Fe,Mn]Si phase and (b) plate-like β-AlFeSi phase.

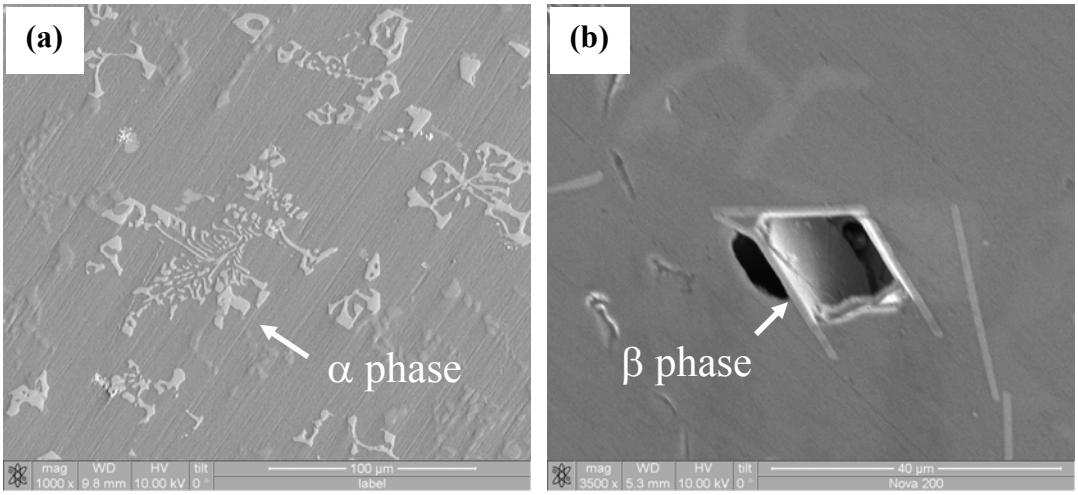

the plate-shaped phase is essentially free of Mn. Furthermore, the compositions of the two phases are slightly different from those of the published phases expected for this system, namely α-$Al_{15}[Fe,Mn]_3Si_2$ and β-Al_5FeSi [14]. The composition difference between the referred α, β intermetallic phases and observed phases might be due to the difference in the starting compositions. (We also found that the amount of Mn does not seem to change the composition of the β phase, although an increase in Mn does result in an increase in the amount of the α phase. In the previous chapter, we discussed the effect of morphological changes on the mechanical properties due to α and β transition.

EBSD analysis was used to investigate the crystal structures of the two different intermetallic phases and typical patterns are shown in Fig. 3.2. In order to get a credible analysis, all available crystallographic information from the various references was utilized in the simulation attempts (Table 3.3). The EBSD pattern from the Chinese script phase (Fig.3.2a) is consistent with the cubic α phase [15], while that from the plate-shaped phase (Fig.3.2b) is consistent with the orthorhombic β phase [17]. However, the EBSD pattern from this α phase is considerably more complex than patterns from typical cubic structures. For example, note that the major zones indexed near the two-fold <010> zone are of the type <583>, <352>, <085>, <380>, and <032> rather than the <110>, <111>, etc. zones typical of common cubic structures. Nevertheless, the indexing provided in Fig.3.2 is consistent with the angular distances between the poles indicated. Other unusual features in these patterns are relatively strong double bands, some of which are asymmetric. The plane traces on the stereography projection in the α phase show in good agreement of EBSD results and

Fig.3.2 Electron backscatter diffraction patterns of the iron intermetallic phases in the 319 type aluminum alloy: (a) α-Al[Fe,Mn]Si phase and (b) β-AlFeSi phase. Note the asymmetric “double bands” in (a) where the red and green lines represent almost parallel bands corresponding to the <352> and <583>, respectively.

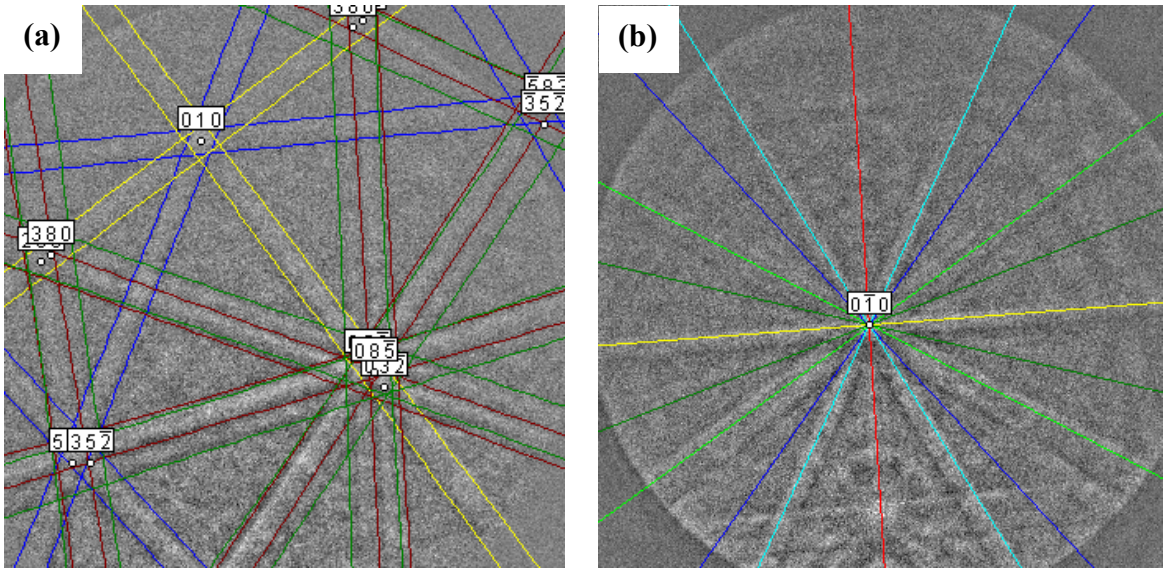

simulated projection in Fig.3.3. There are almost parallel double bands corresponding to the {583} and {352} plane trace. The diffraction spots on the <111> SAD pattern taken from this α phase show the very bright spot at {358} and {352} plane having only 1.63° angle (Fig.3.3b). For the β phase pattern, the structure could probably be indexed with either the orthorhombic, tetragonal or monoclinic structure given the similarities in these phases (Table 3.3).

In an effort to corroborate the EBSD results and to help explain the reason for the predominance of the unusual zones in the α phase, TEM analysis of the α phase was performed. As can be seen in Fig.3.4, the α phase was rather featureless in contrast indicating that there was no significant internal structure that might compromise the diffraction analysis. We did not observe the specific orientation relationship in the aluminum matrix with α phase. As in the EBSD pattern in Fig.3.2a, the <010> convergent beam electron diffraction (CBED) pattern has 2-fold symmetry with two orthogonal mirror planes. Furthermore, the nature of the Kikuchi lines observed in the TEM (illustrated in Fig. 3.4) is consistent with the bands that intersect the 100 pole in the EBSD pattern in Fig.3 2(a). The strong Kikuchi lines correspond to the strong {020}, {400}, and {310} planes, which make the extinctive Kikuchi lines orthogonal to the strong reflection disks. This schematic Kikuchi lines is well matched up to the simulated stereographic projection in Fig.3.3. It is believed that the double Kikuchi bands in Fig.3.2(a) are also likely due to strong reflections disk resulting from atomic structure factor. The CBED patterns with smallest condenser aperture and camera length are shown in Fig.3.5(b).

Table 3.3 Summary of crystallographic data for α-Al[Fe,Mn]Si phase and β-AlFeSi phase in the aluminum alloys.

	Bravais Lattice	a (Å)	b (Å)	c (Å)	β (º)	Ref.
α phase						
$Al_{19}Fe_4MnSi$	cubic	12.56				[15]
$Al_{15[}Fe,Mn]_3Si_2$	cubic	12.5				[14]
Al_8Fe_2Si	hexagonal	12.3		26.3		[14]
β phase						
$Al_{4.5}FeSi$	monoclinic	6.161	6.175	20.813	90.42	[16]
$Al_9Fe_2Si_2$	monoclinic	6.12	6.12	41.5	91	[19]
Al_4FeSi_2	tetragonal	6.14		9.48		[19]
Al_5FeSi	orthorhombic	6.18	6.2	20.8		[17]

Fig.3.3 Plane traces on the stereoprojection and SAD pattern of [111] zone axis of the α phase.

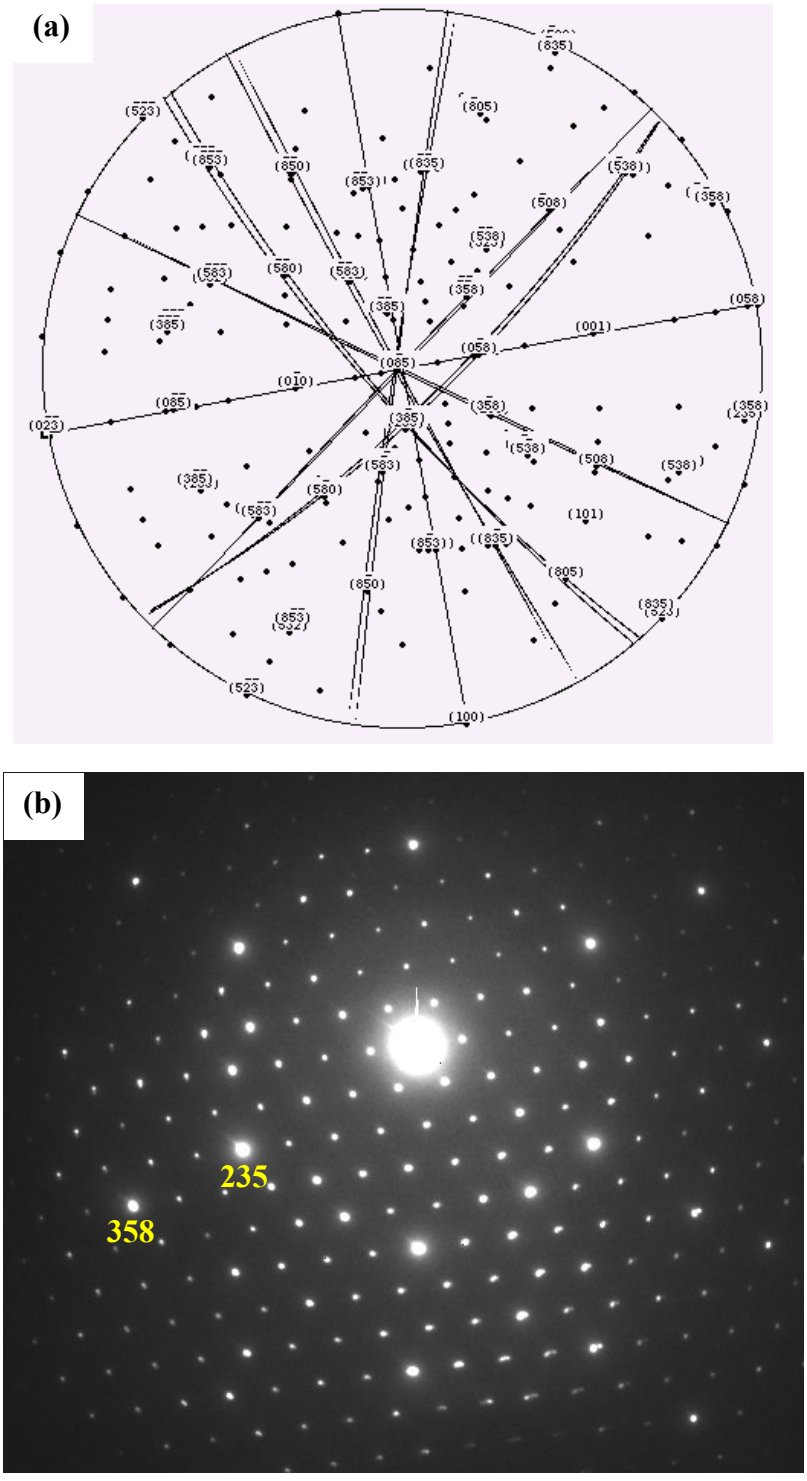

Fig.3.4 Bright field image of Chinese script-like α phase and its CBED patterns from the 3 different zone axis.

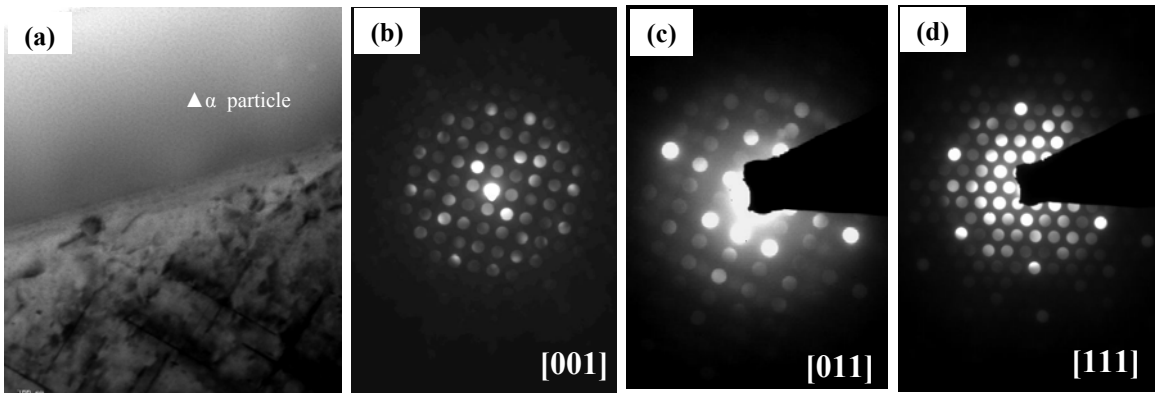

Fig.3.5 Schematic illustrations of Kikuchi lines and CBED patterns of the Chinese-script phase.

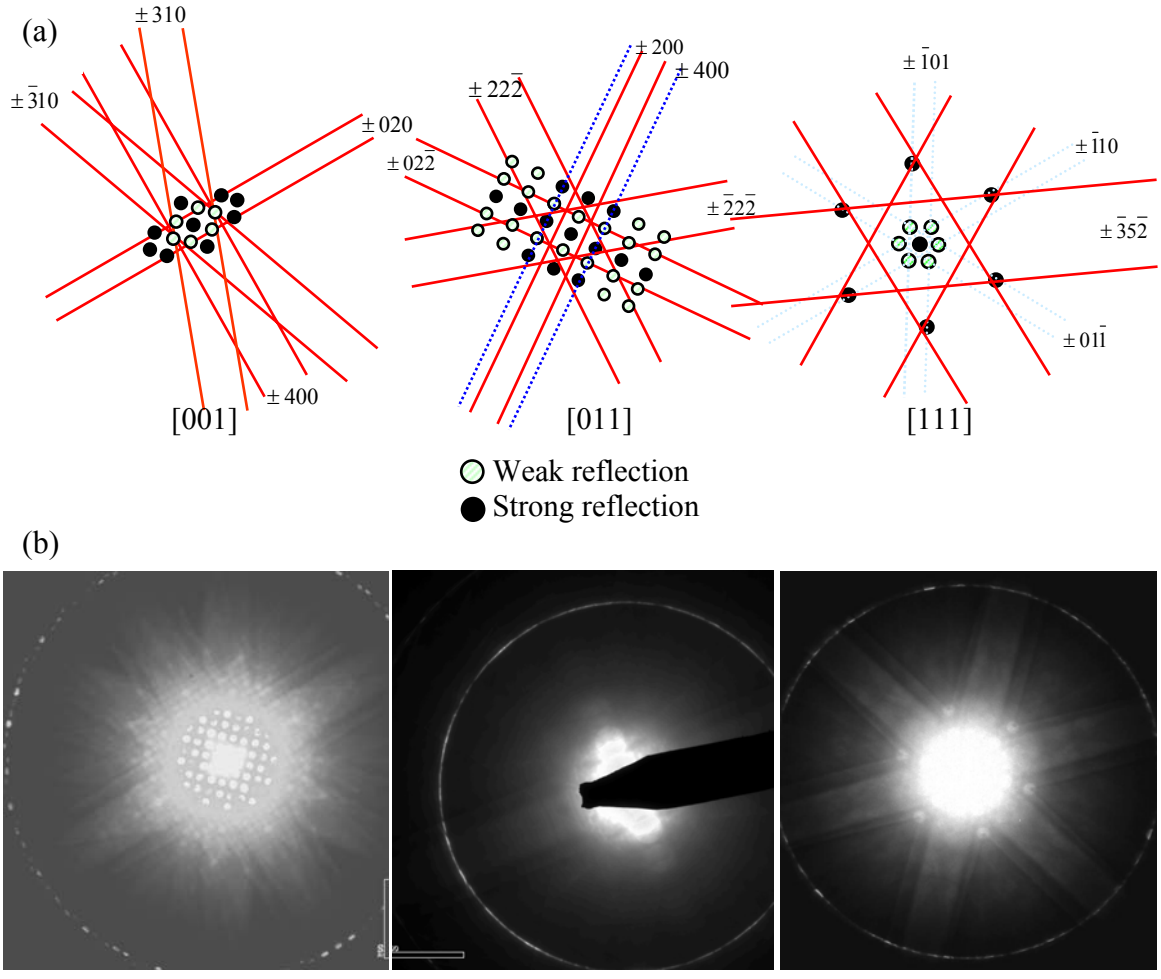

Based on the results, this Chinese script-like intermetallic phase has the lattice parameter of 1.25nm. This phase is pretty much consistent with the phase, $Al_{19}Fe_4MnSi_2$ in Pearson's handbook having Im $\bar{3}$ space group. However, the stoichiometry of chemical composition of the cubic α phase corresponds to $Al_{13}(Fe,Mn)_4Si_3$. This is similar to the body centered cubic α-$Al_{15}(Fe,Mn,Cr)_3Si_2$ phase reported by Mondolfo [14]. The transition element such as Mn and Cr can substitute the iron in the same crystal structure while aluminum content is slightly varied.

The EBSD pattern of a plate-like particle is shown in Fig.3.2(b). The stoichiometry of this phase corresponds to Al_5FeSi which is often called the β phase in the literature. The literature survey of this β phase shows that there are mainly 3 different type structures such as monoclinic, orthorhombic, and tetragonal structure. Regardless of tetragonal phase, monoclinic and orthorhombic β phase have most similar lattice parameters. The structural study of β phase is summarized in Table 3.3. Nevertheless there are numerous studies on the β phases, confusion over its identification still remains. Among the previous results Rømming [16] and Zheng [17] published symmetrical studies of the β phase. They also presented extensive investigation of the β phase using the CBED technique with TEM. However, their results of the β phase analysis are different. This might be because of difficulties in the symmetry analysis due to not only small size, but also poor crystallinity and defects [16]. The results of the present study on the 319 type of aluminum casting alloy is similar to Zheng's analysis [17], where β phases were composed of orthorhombic and tetragonal lattices. The high density of planar defects parallel to the (001) plane were regarded as different structure having two different structure such as orthorhombic and tetragonal

phases, which were cause of the extra patterns along the <12/> reflections on the [210] axis. However, the present study has a different explanation. The typical bright field image and selected area diffraction pattern of the β phase are shown in Fig.3.6. These results are obtained from fault free area. By tracing the major Kikuchi lines under the smallest condenser, the selected area diffraction patterns are obtained from the major zone axis. The diffraction study shows that the β phase has the orthorhombic crystal structure having Cmcm space group. The lattice parameters for this phase were measured as: a = 20.8, b = 6.2, c = 6.18. Our results also have similar diffraction patterns with Zheng's orthorhombic phase. The SAD patterns of the [012] axis clearly corresponds the orthorhombic structure following the general reflection condition: h + k = 2n. However, one interesting result has been observed in the faulted regions in the β intermetallic phase. The bright and dark field images are shown in Fig.3.7. The straight dark lines in Fig.2.7 (a) appear in most β phases, which might be the cause of divergent descriptions of the β phase. The straight lines are parallel to the (100) plane of this β phase within very thin range around 100 nm. The lines correspond to either planar defects or platelet boundaries [18]. We found that extra spot are only observed in the fault area.

The diffraction patterns observed in un-faulted area are presented in Fig.3.7 (c) with patterns from fault area in (d) and (e). There are extra spots corresponding to (121), (321),…..etc. These (h21) reflections should not be allowed for reflection. If those spots come from the tetragonal structure which Zheng mentioned, there should be an increase in the symmetry of this phase. However, we did not see more symmetry. Rather these forbidden spots were only observed in the faulted region. Thus, we

suggest one possible explanation on the appearance of forbidden spots, which is the alternative stacking of orthorhombic structure changing ***b*** and ***c*** axis. The schematic illustrations are shown in Fig. 8. The combined reflections can be obtained in the faulted area by switching the ***b*** and ***c*** axis. This assumption explains the streaks and extra spots along the (h21) in Fig.3.7(d) and (e). The streaks are also observed in the diffraction from the β phase even in other aluminum alloy systems [16-18]. Formation of the fault stacks might be either during transformation to obtain the stable structure from the high temperature to low temperature, or solidification from melt.

From the structural point of view, Chinese script α phase has a cubic structure therefore, it is favorable to grow 3 dimensionally in any direction, while orthorhombic β particles favor to grow in 2 dimensional lateral growth mode. The lateral growth requires more time to obtain the stable structure without defects. However, as the orthorhombic β particles forms in the fast cooling process, it is hard to transform to a defect-free structure. Thus, the planar defects are also likely to form easily along the lateral growth plane. The existence of Mn in the alloys makes the formation of the α phase favorable compared to the β phase. In Mn free samples, we can not observe the α particle for even in the fast cooling samples. The volume of α and β particles are influenced only by the amount of Mn. Therefore, the Mn is important to modify the morphology in the 319 type aluminum alloys.

Fig.3.6 Bright filed image of β phase and selected area diffraction patterns taken from characteristic major zone axes.

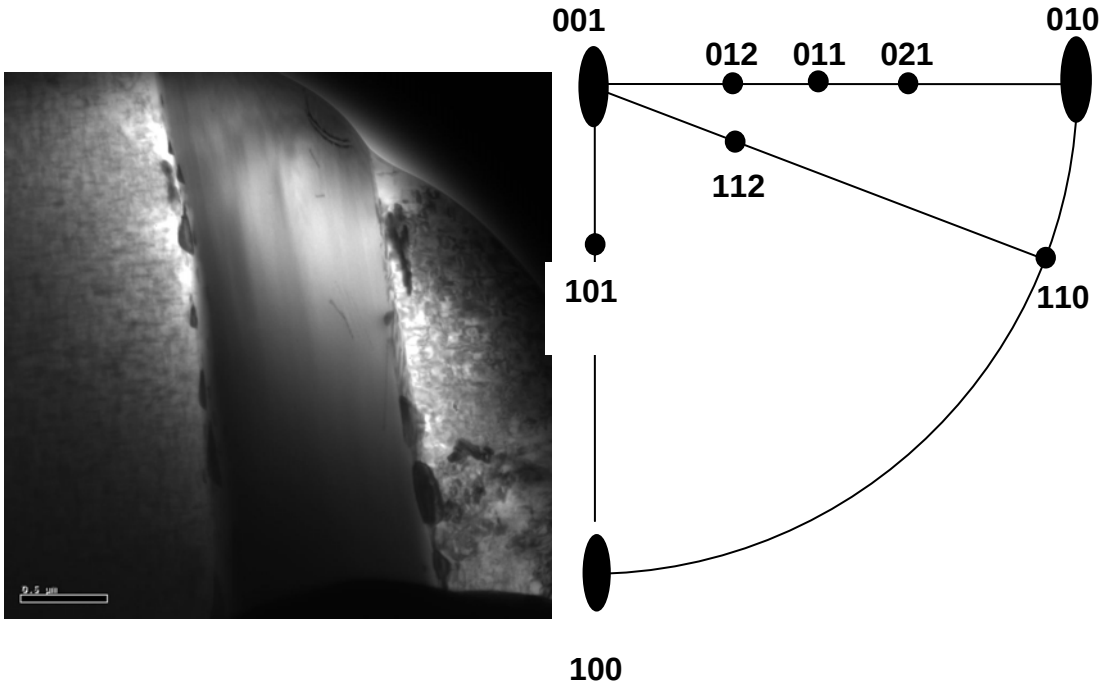

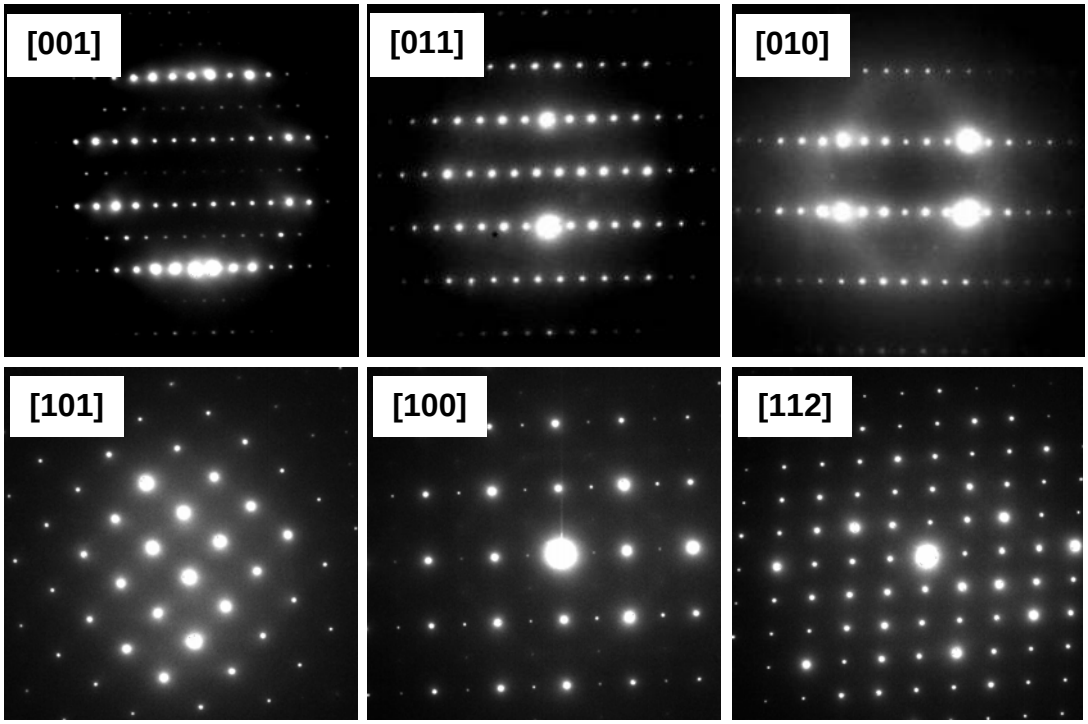

Fig.3.7 (a) Bright field image and (b) dark field image of plate-like β phase in faulted area, and SAD patterns of taken from non-fault area (c,d) and faulted area (e,f)

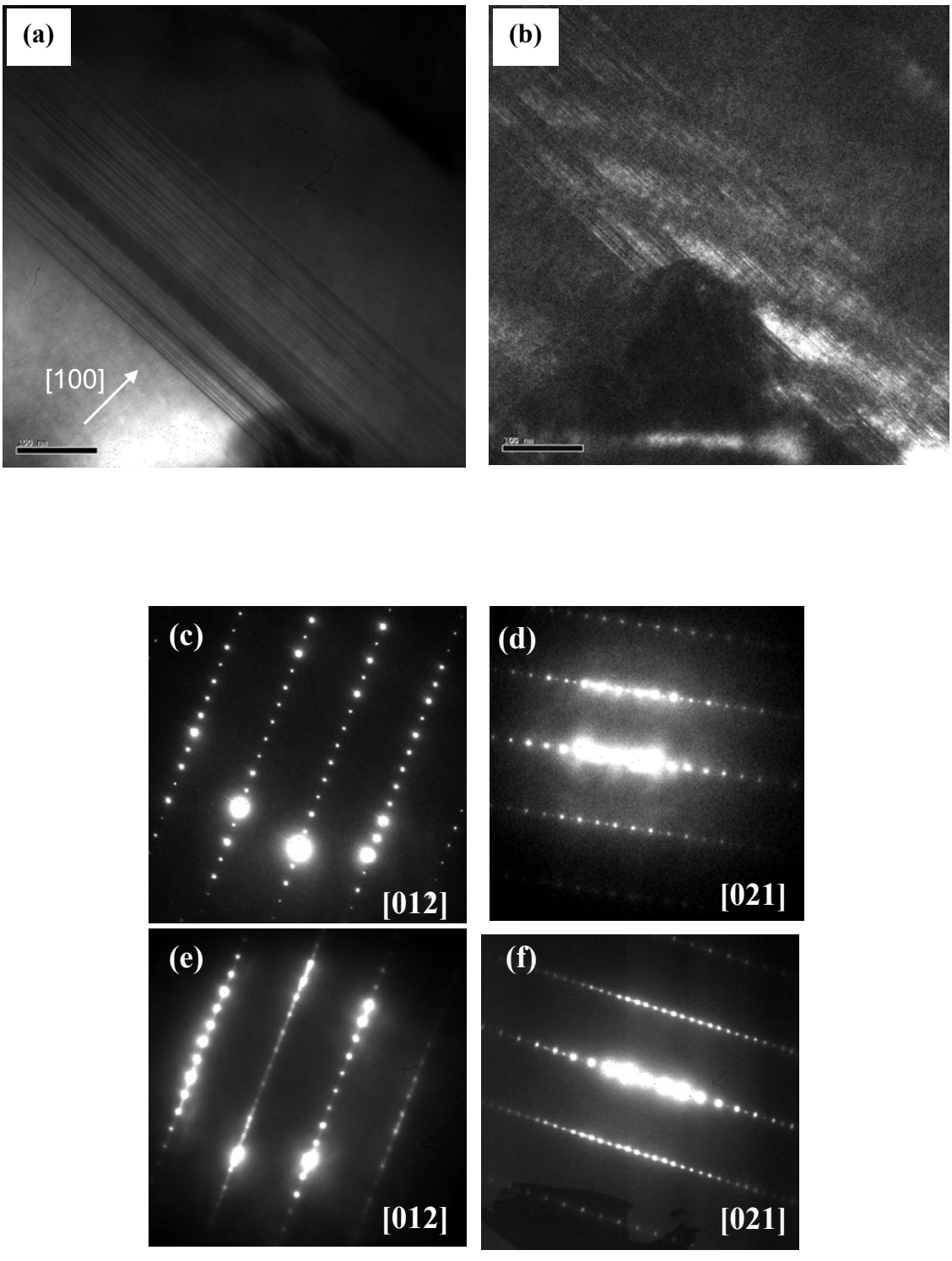

Fig.3.8 Schematic illustrations of appearance of (h21) planes on the [021] zone axis under the faulted β region.

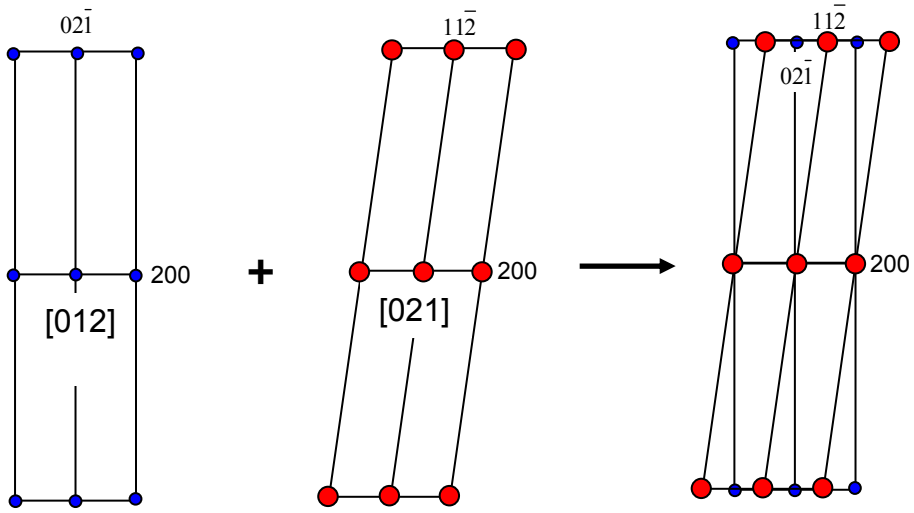

3.4 Reference

[1] A.M. Samuel, F.H. Samuel, Metall. Mater. Trans. A, 26A(1995)2359.

[2] P. Skjerpe, Metall. Trans. A, 18(1987)189.

[3] H. Westengen, Z. Metallkde, 73(1982)360.

[4] A.L. Dons, Z. Metallkde, 76(1985)609.

[5] L.A. Narayanan, F.H. Samuel, J.E. Gruzleski, Metall. Mater. Trans. A, 25(1994)1761.

[6] J.A. Taylor, G.B. Schaffer, D.H. StJohn, Metall. Mater. Trans. A, 30(1999)1657.

[7] W. Khalifa, F.H. Samuel, J.E. Gruzleski, Metall. Mater. Trans. A, 34(2003)807.

[8] W. Khalifa, F.H. Samuel, J.E. Gruzleski, H.W. Doty, S. Valtierra, Metall. Mater. Trans. A, 36(2005)1017.

[9] L. Lu, A.K. Dahle, Metall. Mater. Trans. A, 36(2005)819.

[10] S.G. Shabestari, M. Mahmudi, M. Emamy, J. Campbell, Int. J. Cast Metals Res.15(2002)17.

[11] P. Ashtari, H. Tezuka, T. Sato, Scripta Mater. 51(2004)43.

[12] M.V. Kral, H.R. McIntyre, M.J. Smillie, Scripta Mater. 51(2004)215.

[13] M.V. Kral, Materials Letters, 59(2005)2271.

[14] L.F. Mondolfo, Aluminum Alloys: Structure and Properties, Butterworths, London, 1976.

[15] M. Cooper, Acta Crystal., 23(1967)1106.

[16] C. Rømming, V. Hansen, J. Gjønnes, Acta Cryst. B50(1994)307.

[17] J. G. Zheng, R. Vincent, J.W. Steeds. Philosophical Magazine A, 80(2000)493.

[18] K.Y. Wen, W. Hu, G.Gottstein, Mater. Sci Tech. 19(2003)762.

[19] G. Phragmen, J. Inst. Metal., 77(1950)489

CHAPTER 4

THE EFFECTS OF Mg ADDITIONS ON THE MICROSTRUCUTRE AND MECHANICAL PROPERTIES OF 319 ALUMINUM ALLOYS

4.1 Introduction

Type 319 aluminum casting alloys are widely used in the automotive industry due to their excellent mechanical properties, corrosion resistance and good castability [1]. Several attempts are being made to improve the mechanical properties by additions of alloying elements. Increase in strength was observed in the case of Mg additions [2]. In typical 319 aluminum alloys, Mg is limited to 0.1 wt% to reduce the dross formation, which increases the cost to remove the secondary smelter and induces melt loss during casting. Recently, 319 type alloys with 0.5wt% Mg were produced without significant impact on the melting and casting process [3]. However, there are some arguments as to whether such small additions of Mg have an impact on the microstructure and mechanical properties. For example, DasGupta et al. did not observe any significant improvement in the mechanical properties with an addition of 0.534 wt% Mg after a T5 heat treatment [4] whereas Zindel et al. reported that only 0.15wt% Mg had a significant increase on the hardness with no further increase up to 0.45wt% Mg [5]. A possible explanation for these different reports has to do with the poor understanding of the role of the quaternary Q phase (list reported formula - $Al_4Cu_2Mg_8Si_6$ etc.) and its response to heat treatments. Samuel has observed that equilibrium Q phase is sensitive to the solution heat treatment temperature and, when present, can lead to incipient melting, which greatly reduces the mechanical properties [6]. Even if incipient melting is

eliminated, there remains a poor understanding of the subsequent precipitation and microstructural development of the Q phase and its effect on properties.

It is well known that the development of the θ' precipitates in the peak-aged condition plays a dominant role in the strengthening in 319 type alloys [7]. However, Q type precipitates have been reported to coexist with the θ' phase by Jahn et al. [8]. They suggested that this quaternary phase forms such a small amount that it might not contribute to the hardening behavior. In addition, due to its very small dimensions, it has been difficult to observe in a manner that allows for determination of its structure and composition when using conventional transmission electron microscopy techniques. As a result, there have been some inconsistencies in the composition and structure reported by different investigators [9]. The objectives of this research are to evaluate the role of Mg on the microstructure in both as-cast and aged samples, and to correlate the mechanical properties with the microstructural observations. Quantitative transmission electron microscopy (TEM) studies are conducted to identify the structures and morphologies of the various precipitates in both Mg-free and Mg-containing 319 type aluminum alloys. In addition, a three-dimensional atom probe has been used to measure the compositions of the various phases. These combined results help to clarify the role of Mg in the precipitation hardening of modified 319 type aluminum alloys.

4.2 Experimental Procedures

In order to investigate the effects of Mg on the microstructure and properties, a Mg-free alloy and an alloy containing 0.45 wt% Mg added to the typical 319 type aluminum alloys were used in these experiments. The overall compositions of these two alloys are presented in Table 4.1. The casting conditions and post annealing

treatments were described in chapter 3. An iron chill plate was used in some of the casting in order to increase the solidification rate and produce a finer dendritic structure near the end of the mold during solidification.

After casting, the samples were solution treated at 488°C for 8 h and quenched in warm water. The subsequent T6 aging treatment was carried out at 193°C for 8h based on previous studies. Microstructural characterization was carried out using optical microscopy, scanning electron microscopy and transmission electron microscopy. 3D atom probe tomography was used to determine the three-dimensional morphologies, and compositions of the various phases. The procedures for performing the 3DAP analysis are described in appendix A.

Table 4.1 Compositions of the Type 319 aluminum alloys used in the experiment.

	Element (wt. %)					
	Al	Si	Cu	Fe	Mg	Mn
Mg-free	Bal	6.7	3.75	0.6	0	0
Mg-containing	Bal	6.7	3.75	0.5	0.45	0.02

4.3 Results and Discussion

4.3.1 As-cast Microstructures

The as-cast microstructures of the two 319 aluminum alloys consist of α-Al dendrites, plate-shaped β-Al_5FeSi, eutectic Si, and equilibrium θ-Al_2Cu (Fig.4.1). In the case of the alloy containing Mg Fig.4.1(b), an additional phase, the quaternary Q phase, was observed near the θ or silicon phases. Interestingly, the Q phase was always in contact with the θ phase. This suggests that the Q phase probably occurs during the final eutectic reaction during solidification. This is in agreement with the thermal analysis results reported by Samuel et al. [10]. SEM micrographs and X-ray maps from the two as-cast alloys indicate that the plate-like iron-containing phase is the β-Al_5FeSi phase (Fig.4.2 and 4.3). In addition, the Mg-containing alloy contained what appears to be a quaternary phase, which was assumed to be the Q phase with a composition measured using EDS to be approximately Al-32Mg-29Si-14Cu with considerable variation observed when different regions were measured. Clearly, based on the results in Chapters 2 and 3, there was none of the Chinese script α phase. Likewise, there was none of the Fe and Mg-rich π phase ($Al_8Mg_3FeSi_6$) indicating that magnesium does not cause modification of the iron-containing intermetallic phase. The variation in composition of the Q phase appears to be consistent with the variations reported in the literature [9]. Specifically, various stoichiometries have been reported for the Q phase including $Al_4CuMg_5Si_4$, $Al_5Cu_2Mg_8Si_6$, $Al_4Cu_2Mg_8Si_7$, $Al_4Cu_2Mg_8Si_5$. These variations are likely to come from the overall compositions and solidification conditions of the alloys being investigated as well as possible errors in the measurements. From the section of the quaternary phase diagram for the Al-Si-Cu-Mg at 502°C and 4wt% Cu

Fig.4.1 Optical micrographs of the as-cast condition in Mg-free(a), and Mg-containing (b) 319 type aluminum alloys.

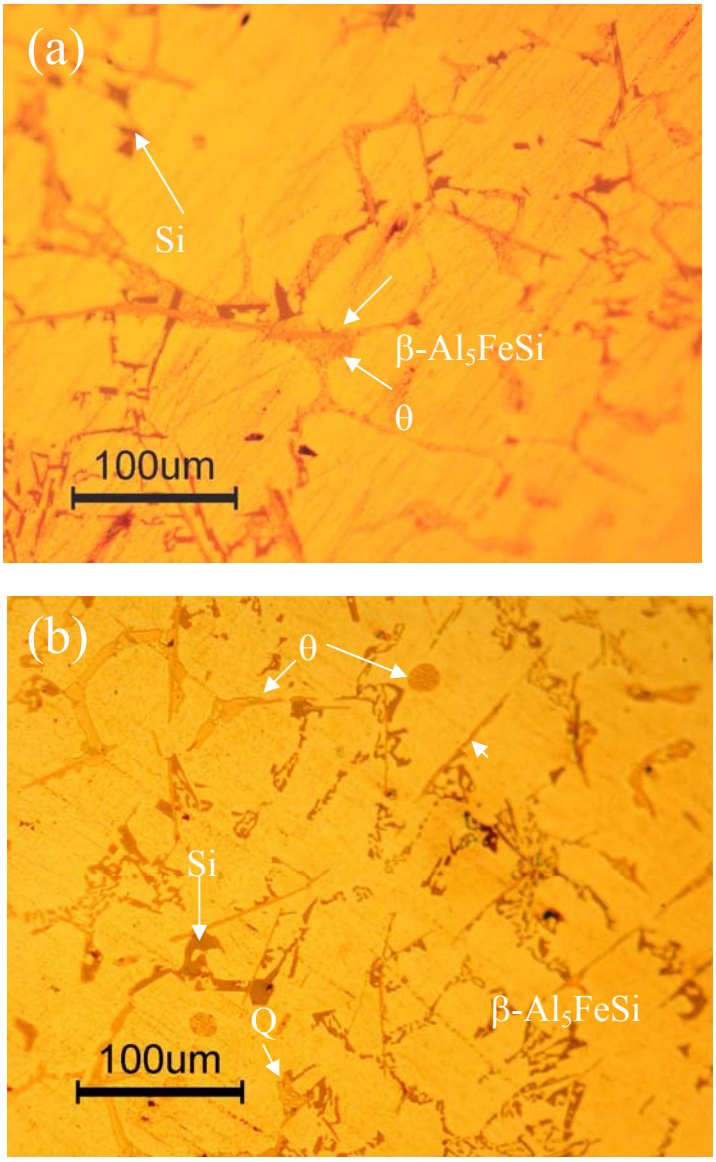

Fig.4.2 SEM microstructure and EDX maps of the Mg-free alloy in the as-cast condition.

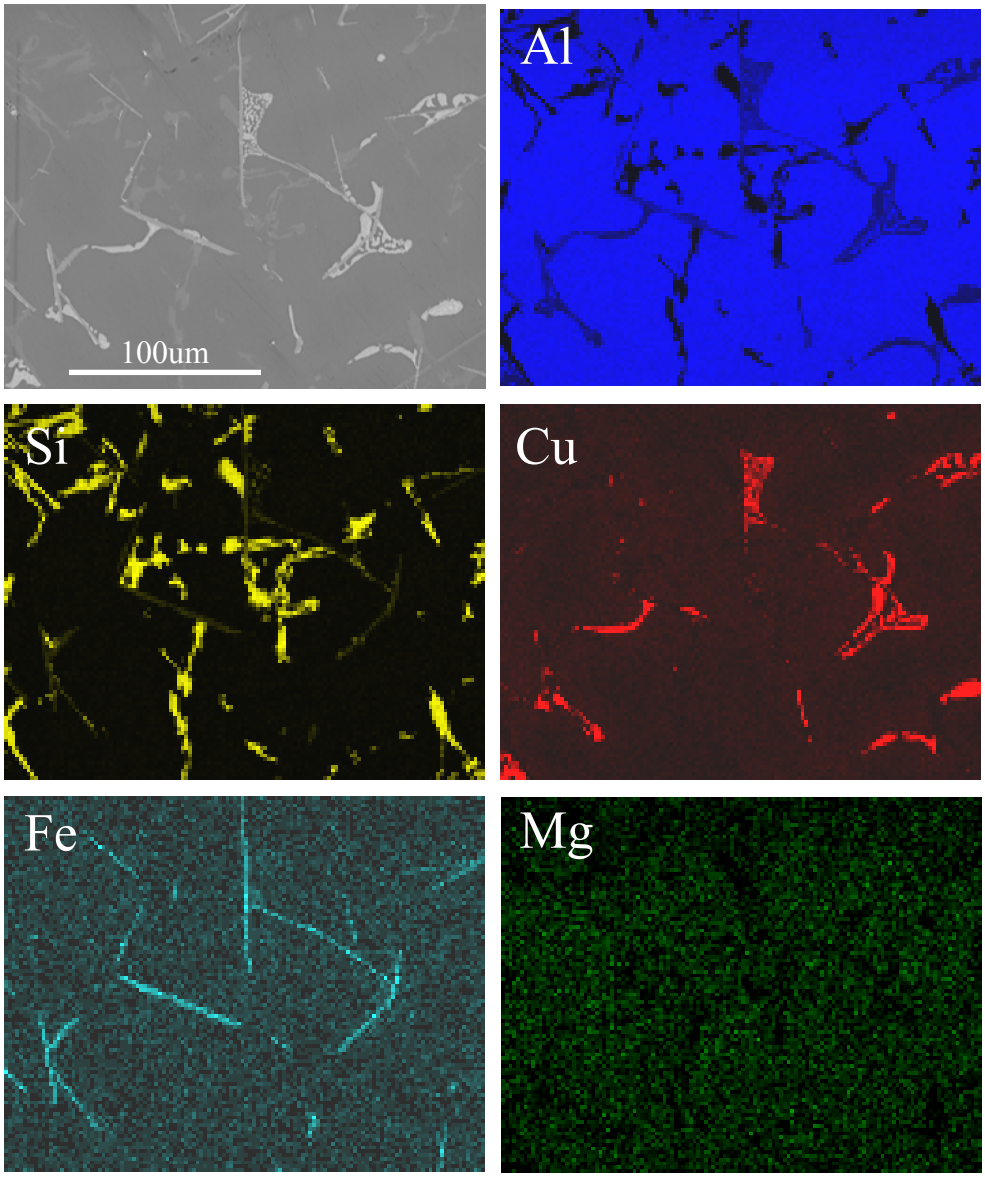

Fig.4.3 SEM microstructure and EDX maps of the Mg-containing alloy in the as-cast condition.

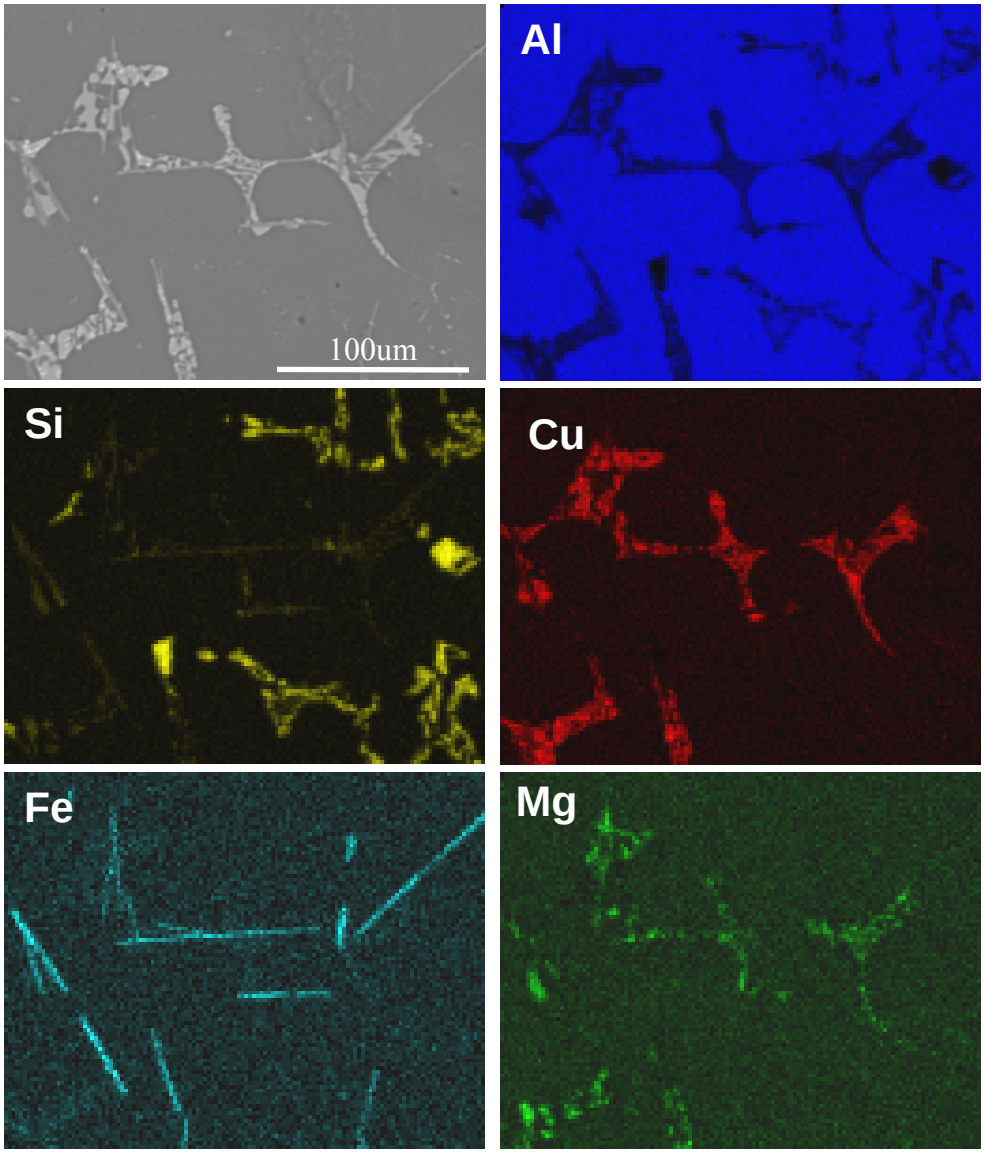

shown in Fig. 4.4 [11], the quaternary Q phase is expected to form along with the α-Al and Si and θ phases. This is in a good agreement with our experimental results. However, there are still arguments as to whether the Q phase has a unique composition or whether it exists over a range of compositions. [12]. Regardless of the Q composition in the as cast material, it will be shown below that the Mg additions do influence the age hardening behavior and mechanical properties [13].

In an effort to determine the composition and crystal structure of the Q phase in detail, analytical transmission electron microscopy was performed. As can be seen in Fig.4.5, the Q phase was observed near dislocations in the matrix. Selected area diffraction patterns (SADPs) obtained from the Q phase (Fig. 4.5b, 5c) indicated that the Q phase has a hexagonal unit cell with a~1.04nm and c~0.4nm. This is consistent with the crystal structure reported by Arnberg et al. [14] who suggested that the composition of the Q phase was approximately $Al_4Cu_2Mg_8Si_7$. Although the composition measured in this study is slightly different, the structural similarity indicates that this is truly the same Q phase reported previously. The simulated patterns using Desktop Microscopy are also presented in the Fig. 4.5(d), and (e).

Fig.4.4 Section of the quaternary phase diagram for the Al-Si-Cu-Mg system at 502°C and 4wt% Cu [11].

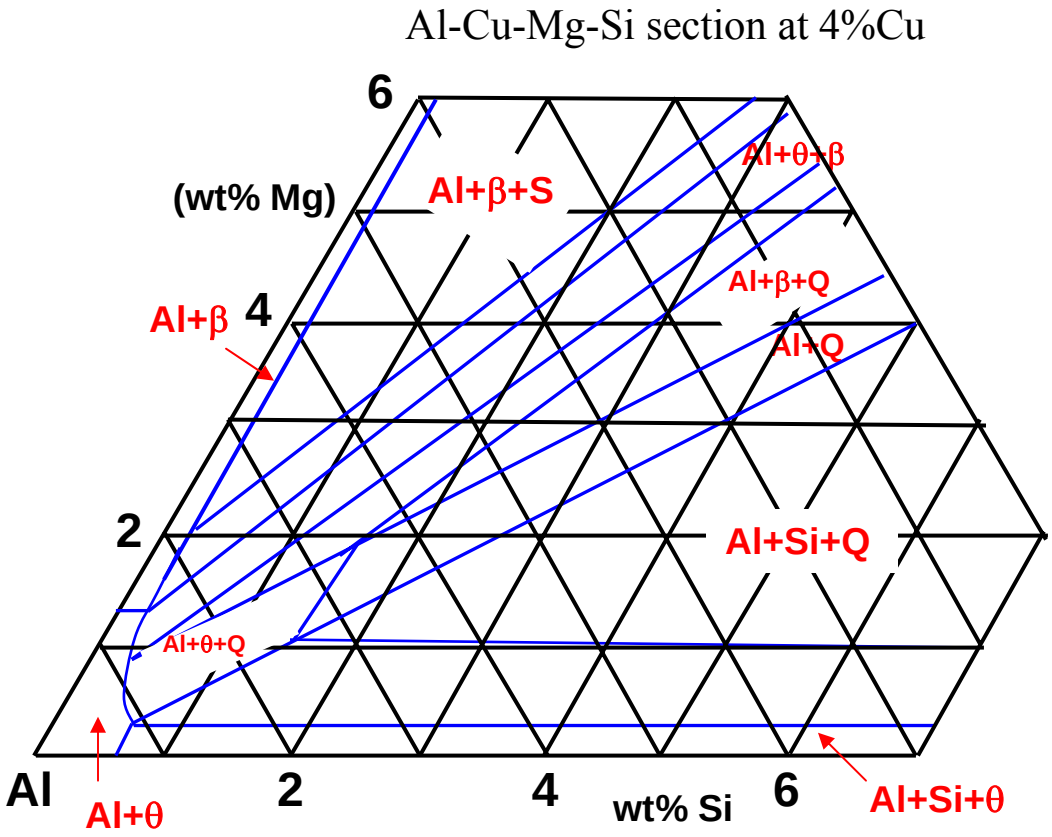

Fig.4.5 BF TEM image and selected area diffraction patterns of the Q phase in the Mg-containing sample in the as-cast condition.

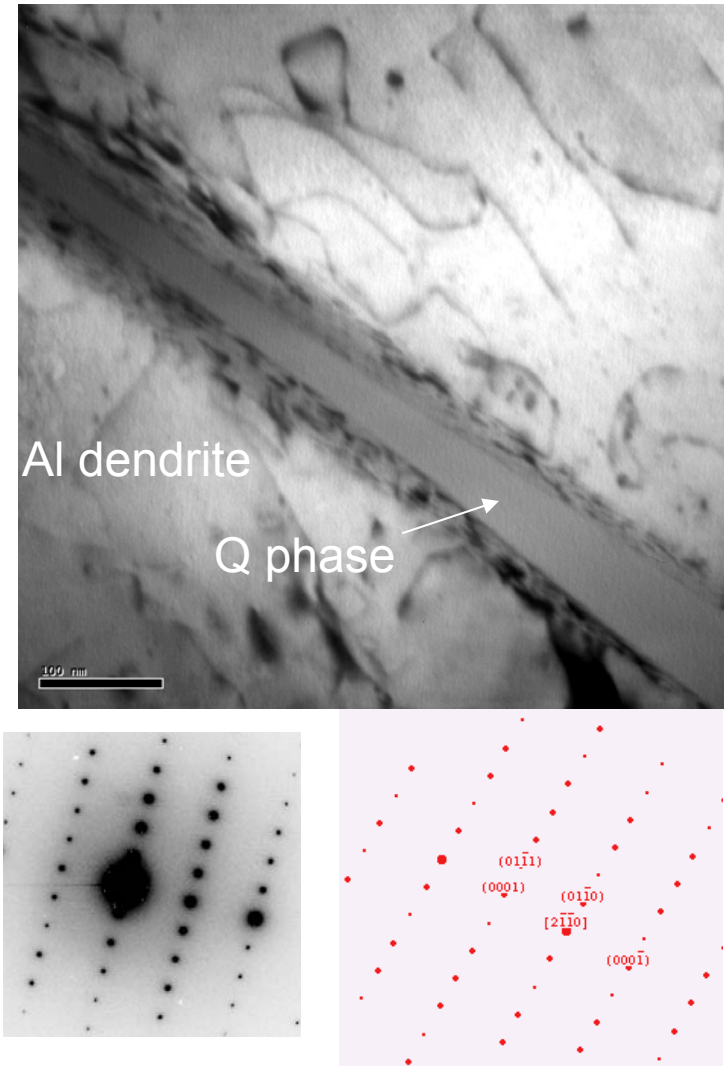

4.3.2 Microstructure in the T6 Condition

The optical microstructures of the Mg free and Mg-modified 319 aluminum alloys after the T6 heat treatment are shown in Fig.4.6. Compared to the as-cast microstructure in Fig. 4.1, it is obvious that solution heat treatment and aging affected the microstructural features. For example, a significant amount of the fine eutectic phases such as Al_2Cu and Q phase are dissolved in the matrix, while some other phases such as eutectic Si and β-Al_5FeSi phase have coarsened slightly. As can be seen in Fig.4.6, the blocky Al_2Cu phases still remained in the matrix without completely dissolving. There is no evidence of dissolution of the β-Al_5FeSi or fragmentation even in the Mg containing sample. It is different from the previous result [10]. It is noteworthy that Mg additions did not change the microstructure even after the heat treatment except for the dissolution of the Mg-containing Q phase. The SEM micrographs and EDX maps in Figs.4.7 and 8 reveal the dissolution of the fine eutectic phase, while the large and blocky θ and Q phases are partially dissolved during the aging process. After the T6 aging treatment, the Mg-free alloy contained thin plate-like θ' precipitates lying parallel to the {001} planes. The streaking along the 002 systematic rows in the SAD pattern (Fig. 4.9(b)) is consistent with the thin nature of these precipitates. Since the θ' phase has a body centered tetragonal structure with a=0.404nm and c=0.58nm, it is not surprising that the θ' phase is extremely thin (around 4nm thickness) along [001] direction and that it has a square-like morphology (around 100nm on a side) in the other two dimensions.

Fig. 4.6 Optical micrographs of the T6 condition in the Mg-free(a), and Mg-containing (b) 319 type aluminum alloys.

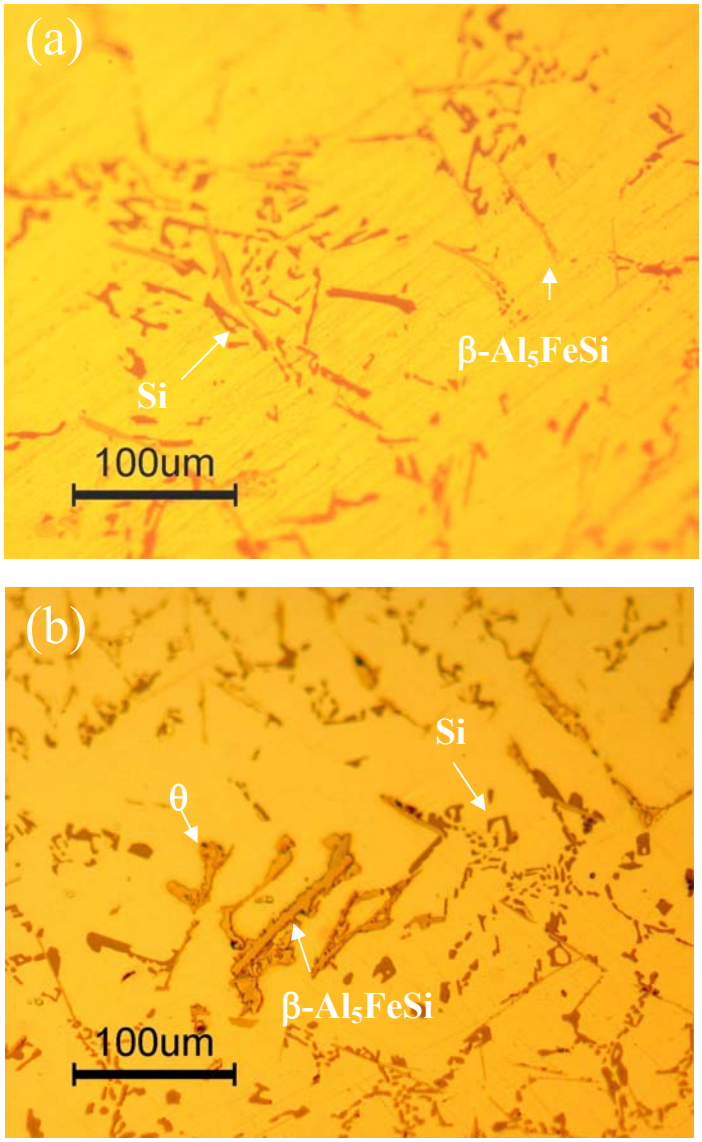

Fig. 4.7 SEM microstructure and EDX maps of the Mg-free alloy after T6 aging heat treatment.

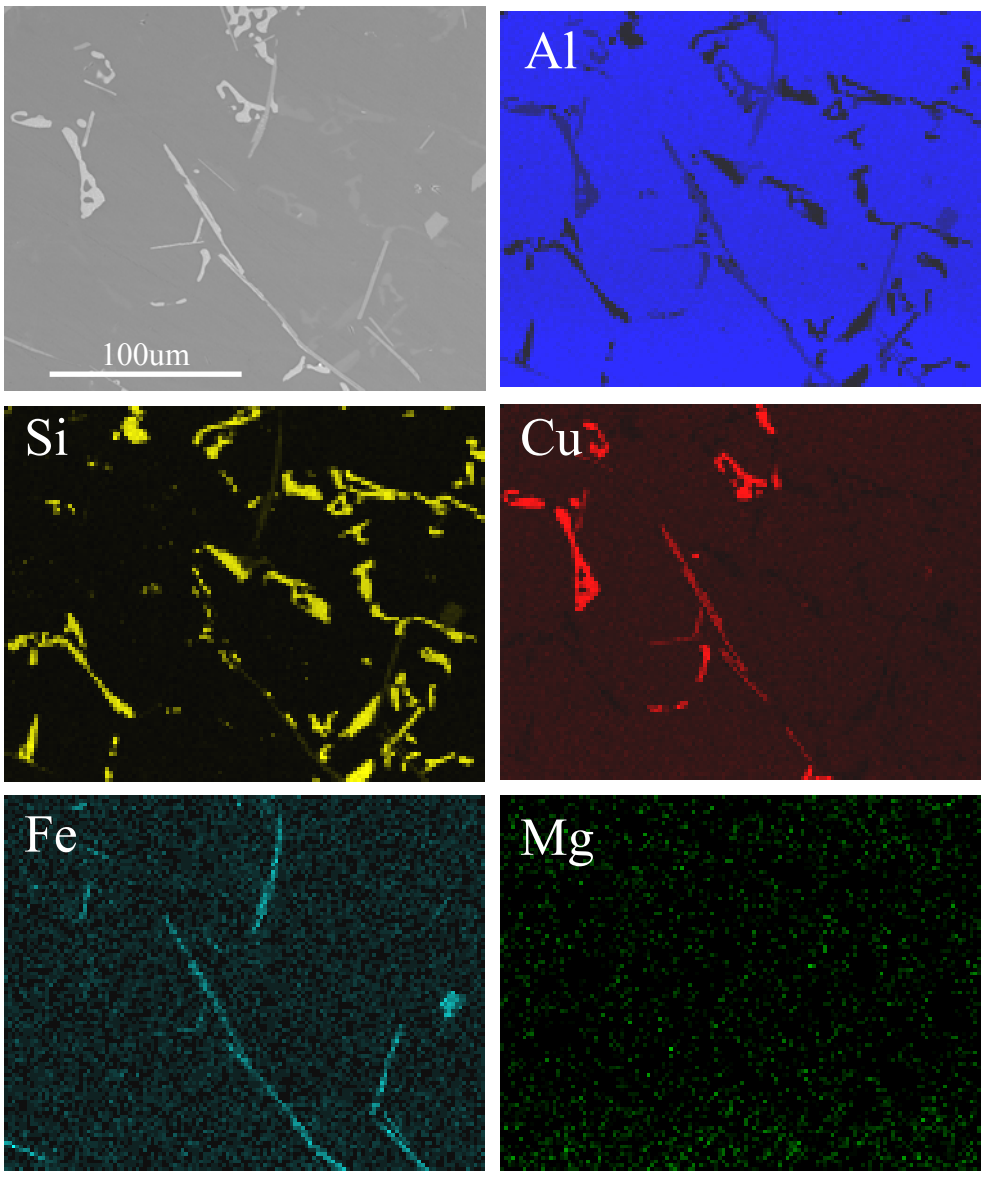

Fig.4.8 SEM microstructure and EDX maps of the Mg-containing alloy after the T6 aging heat treatment.

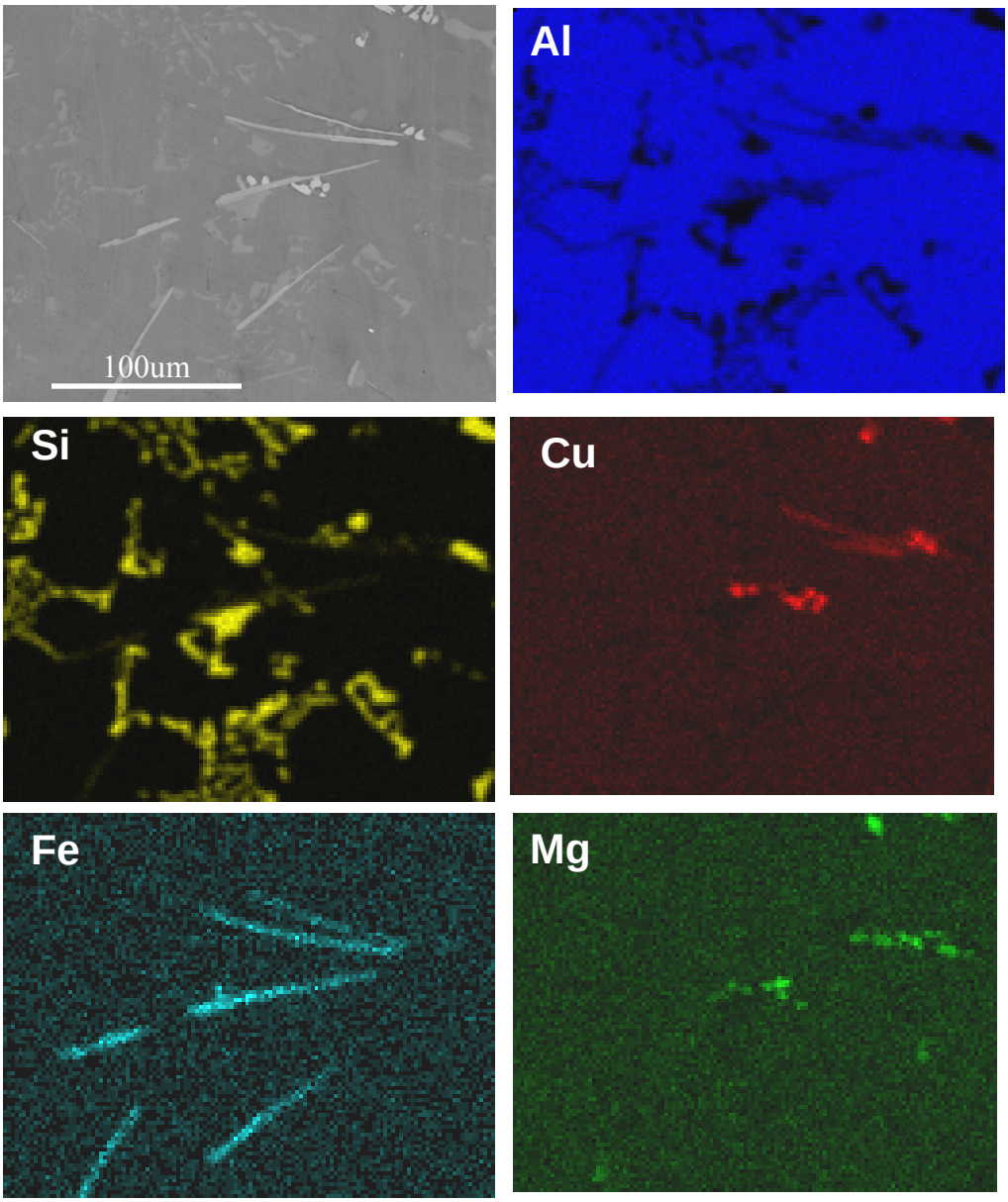

In the case of the Mg-containing sample, additional fine precipitates were observed in addition to the θ' plates (Fig.4.10). These fine particles appear equiaxed or lath-like and are only ~4nm length. Based on the morphology this phase appears similar to that reported by both Jahn [8] and Chakrabarti [9]. They suggested this phase as a Q' or Q type precipitate. However, it is hard to identify the crystal structure and chemistry due to its extremely small dimensions even high number of density. The number density of this fine precipitate is 192/μm^2, while the number density of the θ' precipitate is 53/μm^2. Therefore, it is believed that both types of precipitates can significantly increase the strength in the matrix. The simulated yield strength results enhanced by the two different precipitates are discussed in appendix 2 based on morphological features such as precipitate shape, size, and volume density.

The compositions of the θ' and Q' precipitates were analyzed using the 3DAP and three dimensional maps representing the distribution of (a) aluminum, (b) silicon, (c) copper, and (d) magnesium in the Mg-containing 319 aluminum alloy after T6 aging treatment (Fig. 4.11). The two different types of precipitates observed are well matched with the morphologies of the precipitates shown in Fig.4.10. We observed approximately 6.8 million atoms consisting of 98.7% Al, 0.3% Si, 0.8% Cu, and 0.2% Mg in the sample. Aluminum and silicon were distributed throughout the matrix, while copper and magnesium were mostly detected in the precipitates. The large particles in the center do not contain magnesium and, based on their composition (~66%Al and 33%Cu), must correspond to the θ' plates. On the contrary the smaller lath-like precipitates contain copper, silicon and magnesium. The composition appears to be approximately 35 at% Al, 10 at% Cu, 30 at% Si, and 25 at% Mg. This phase is different from the ternary S

(Al_2CuMg) and binary β (Mg_2Si) type precipitates reported in some alloys and, therefore appears to be similar to the Q phase that was present in the as-cast material but went into solution during the solution heat treatment. A detailed study of the crystal structure and phase identification will be discussed in the following chapter.

Fig.4.9 TEM bright field image and [001] SAD pattern from the Mg-free alloy after the T6 heat treatment. The extra reflections and streaking in the SADP are consistent with the presence of thin θ' precipitates.

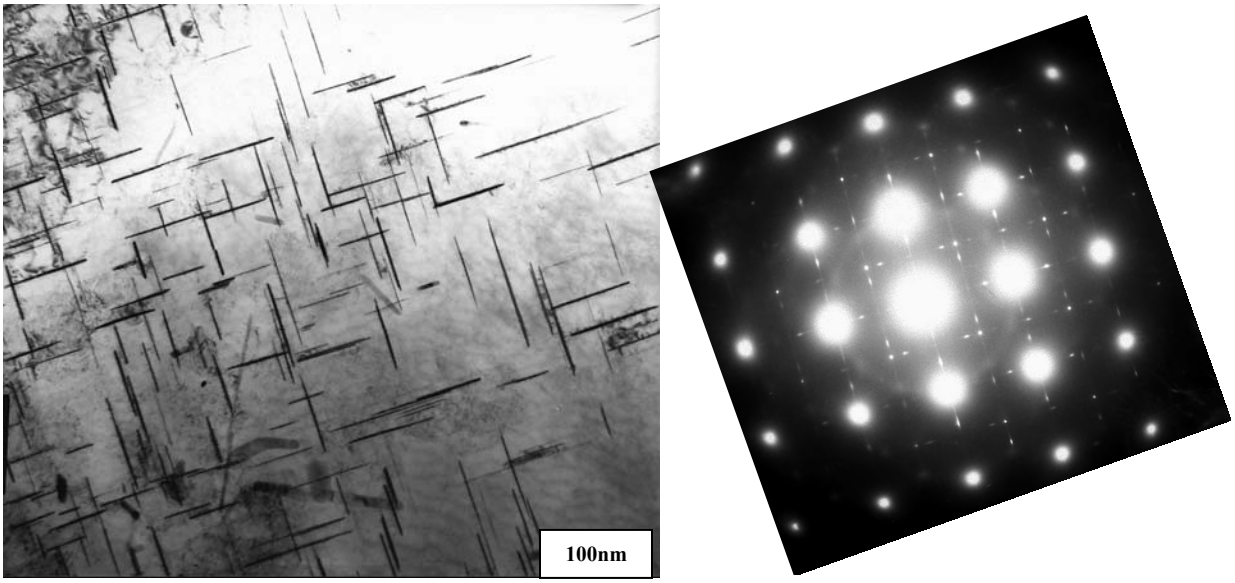

Fig.4.10 TEM bright field image and [001] SAD pattern from the Mg-containing alloy after the T6 heat treatment. The extra reflections in the SADP result from the presence of small Q' precipitates.

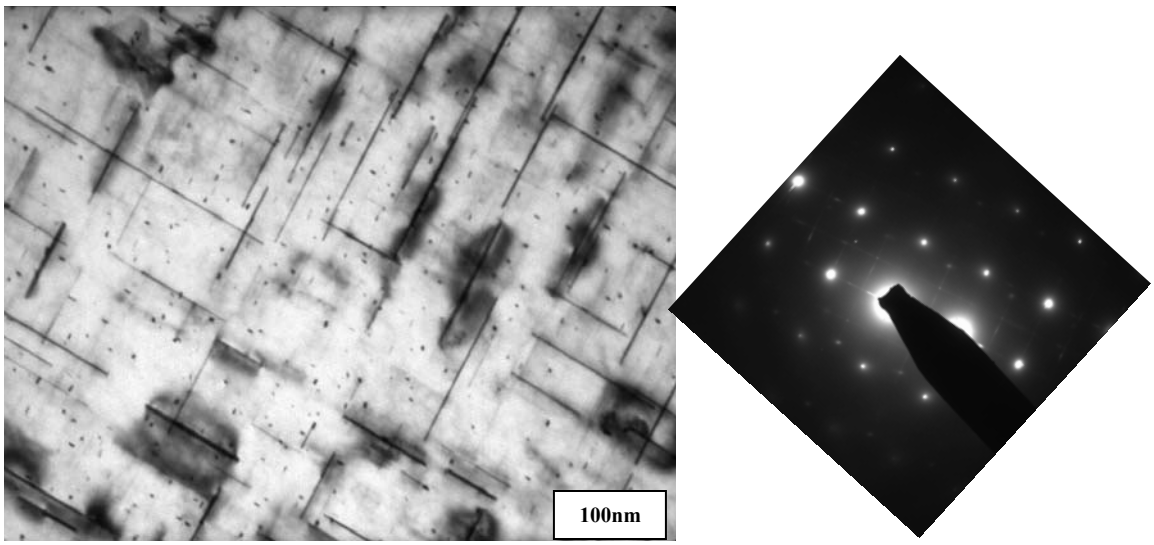

Fig. 4.11 Three dimensional atom maps showing the distribution of the Al, Si, Cu, and Mg atoms in the Mg-containing alloy after the T6 heat treatment. The mixture of Si, Cu, Mg atoms is represented in the (e).

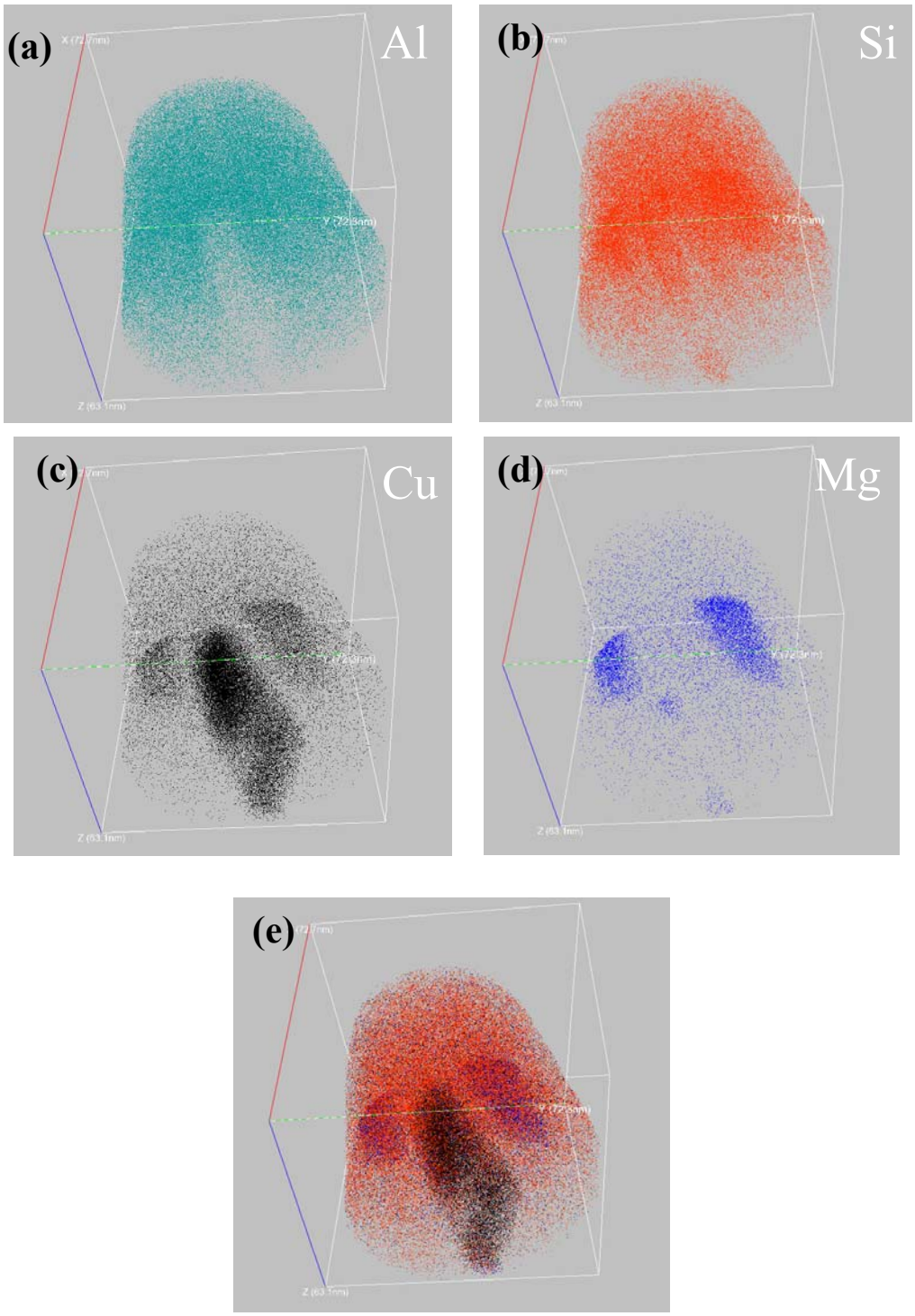

4.3.3 Mechanical Properties Studies

As already shown, there was a considerable difference observed in the aging response of the Mg-free and Mg-containing alloys. As expected, these microstructural differences result in variations in the mechanical properties of these two alloys (Fig. 4.12). As can be seen, there is a 70% increase in the UTS in the Mg-containing alloy from 196 to 328 MPa, while in the case of Mg free alloy, only a30% increase was observed after the same heat treatment. It is believed that this difference in aging response is attributed to the distribution of the small Q' precipitates in the Mg-containing alloy. Unfortunately, the yield strength was unable to be measured due to the low ductility of the Mg-containing alloy. The low ductility is probably the result of the iron containing β phases. However, the results indicate that it is possible to obtain a desirable strength enhancement in the 319 type aluminum alloys with proper additions of Mg and proper heat treatments. The modification of the iron intermetallic phase with Mg addition seems to be effective to achieve the mechanical properties in the industry.

Fig.4.12 Ultimate tensile strength and % elongation of Mg-free and Mg-containing samples in the as-cast condition (blue) and the T6 condition (red).

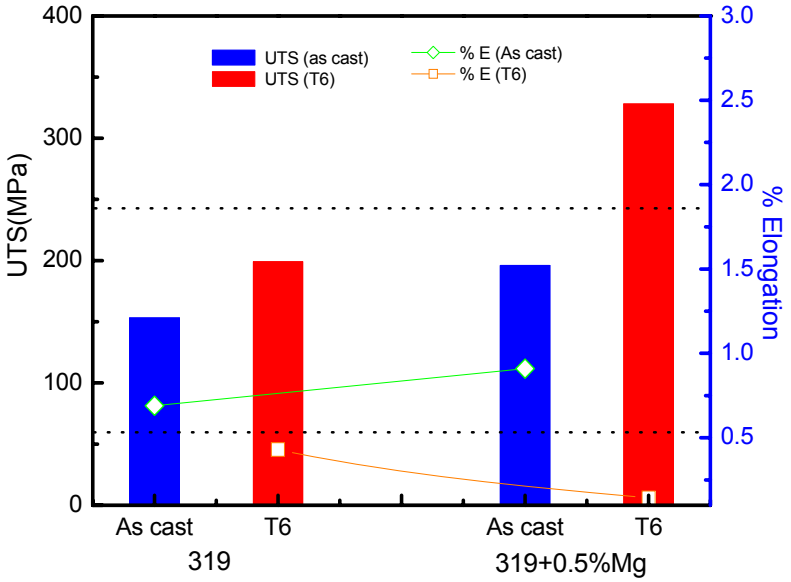

4.4 Reference

[1] Z. Li, A.M. Samuel, F.H. Samuel, C. Ravindran, S. Valtierra, H.W. Doty, Mater. Sci. Eng. A, 367 (2004) 96.

[2] P. Ouellet, F.H. Samuel, J. Mater. Sci., 34 (1999) 4671.

[3] F.H. Samuel, A.M. Samuel, H.W. Doty, AFS, 104 (1996) 893

[4] R. DasGupta, C.C. Brown, S. Marek, AFS. Trans. 97 (1989) 245.

[5] J.W. Zindel, K.A. Kofeldt, L.A. Godlewski, R. Vijayaraghavan, W.T. Donlon, SAE world congress & Exhibition, Apr.2006, Detroit, MI.

[6] F. H. Samuel, J. Mater. Sci. 33 (1998) 2283.

[7] J.E. Hatch, Aluminum: Properties and Physical Metallurgy, ASM, 1984.

[8] R. Jahn, W. Donlon, J.E. Allison, Automotive Alloys, 1999, TMS, pp.247.

[9] D.J. Chakrabarti, D.E. Laughlin, Prog. Mater. Sci, 49 (2004) 389.

[10] F.H. Samuel, P. Ouellet, A.M. Samuel, H.W. Doty, Metall. Mater. Trans. A, 29A (2004) 2871.

[11] L.F. Mondolfo, Aluminum Alloys: Structure and Properties, Butterworths, London, 1976

[12] G.C. Weatherly, A. Perovic, N.K. Mukhopadhyay, D.J. Lloyd, D.D. Perovic, Metall. Mater. Trans. 32A (2001) 213.

[13] J.Y. Hwang, H.W. Doty, M.J. Kaufman, TMS Letters, 3 (2006) 39.

[14] L. Arnberg, B. Aurivillius, Acta Chem. Scand. A. 34 (1980) 1.

CHAPTER 5

CHARACTERIZATION OF THE THREE DIMENSIONAL STRUCTURE OF NANOSCALE PRECIPITATES IN MODIFIED 319 TYPE Al ALLOYS

5.1 Introduction

The aluminum copper system has been studied extensively because of its classical precipitation hardening behavior and, as a result, it forms the basis of much of our understanding of precipitation phenomena in materials. From an industrial standpoint, the important 2XXX, 6XXX wrought alloys and the 2XX and 3XX cast alloys contain copper as one of the primary components, because of the very substantial strengthening that can be achieved using proper heat treatments. Significantly however, the nanoscale nature of the copper-rich θ' precipitates in the alloys heat treated to maximum strength are difficult to characterize using conventional methods e.g., X-ray diffraction, scanning electron microscopy, transmission electron microscopy due to the fact that they tend to be very thin (3-10 nm) disks or plates, which makes it challenging to probe them for both structure and composition. Furthermore, minor fluctuations in the composition of the aluminum matrix are essentially impossible to determine using TEM equipped with energy dispersive spectroscopy methods. Fortunately, the recent developments in the area of 3D atom probe tomography (3DAP) provide significant advantages over TEM for measuring fine scale compositional fluctuations, interfacial segregation and precipitate morphologies [1-3]. Obviously, TEM methods are complementary given that one can also obtain structural information via diffraction and bonding information using electron energy loss spectroscopy.

In the present study, we have used both high resolution TEM and 3DAP to characterize the nanochemistry and morphological features of an Mg-modified Type 319 casting aluminum alloy (Al-7Si-4Cu-0.5Mg) that was heat treated to a T6 condition. In the 319 aluminum alloys, the metastable θ'-Al_2Cu phase is the typical strengthening phase responsible for the precipitation hardening in these alloys. Small (~0.5%) Mg additions lead to increases in the T6 strength over standard alloys [4]; while such increases have been reported in the literature, there have been considerable discrepancies in the identification of the additional fine-scale precipitates that form due primarily to the characterization challenges mentioned above. For example, some authors reported that the small precipitates are β' (Mg_2Si type) [5], S' (Al_2CuMg type) [6], and Q' (containing Al, Mg, Si and Cu) [7,8] in the 3XX type casting alloys. However, despite the extensive studies of the precipitation hardening in these alloys over several decades, each decade has brought new discovery and controversy concerning the structures and compositions of the precipitates in the ternary or quaternary multi-component systems.

The focus of this study was on the identification of the additional strengthening phase in the quaternary Al-Si-Cu-Mg alloy using the three-dimensional atom probe tomography combined with high resolution transmission electron microscopy in order to investigate more clearly the structure, composition and morphology of these strengthening precipitates that form in modified 319 type aluminum alloys. The results help clarify the role of Si and Mg in the precipitation hardening in this particular system.

5.2 Experimental Procedures

The samples used in this study were from Al-7Si-4Cu-0.5Mg alloys that were cast into sand molds and then given standard solution heat treating and aging treatments, namely, 480°C, 8h, warm water quenched followed by 8h at 193°C to achieve T6 properties. The 3DAP analysis was carried out using the local electrode atom probe (LEAP) system developed at Imago, Inc. Sharp needle-like specimens (<100 nm tip radius) were prepared from the matrix regions of interest using a NOVA 200 focused ion beam (FIB) – field emission SEM system; these were then lifted out using an Omniprobe nanomanipulator and then attached to silicon microtips. The samples of interest are then inserted into an Imago LEAP 3DAP for analysis. The specimen temperature during atom probe analysis was held below ~70K and the extraction voltage used was approximately 5 kV. Both conventional and high resolution TEM analysis was also performed using both a Tecnai F20 ST TEM and a Philips EM420 TEM on samples that were produced by conventional electro-polishing techniques. A more detailed description of the sample preparation is presented in appendix 1.

5.3 Results and Discussion

The bright field TEM image of the as-cast structure in Fig.5.1 indicates that the alloy contains several undissolved interdendritic phases including silicon, α-$Al_{13}(Fe,Mn)_4Si_2$, θ-Al_2Cu and Q-$Al_4Cu_2Mg_8Si_6$. The EDS results are presented in Table 5.1 and confirm the presence of these particular phases. The effects of Mg on the structure and mechanical properties of this important alloy were addressed in the chapter 4.

A BFTEM micrograph of the matrix regions after the T6 aging treatment (Fig.5.2a) indicates that the sample contains two different fine-scale precipitates, namely what is believed to be θ' disks or plates on {001} planes and a second smaller phase which appears to be “lath-shaped” but with a habit plane (lath axis) that is at a very slight angle to the <001> matrix directions. The thin, plate-like (2-4 nm thick by 60-120 nm wide) θ' precipitates aligned along $\{001\}_{Al}$ planes are apparent in these images. The streaking in the corresponding SAD pattern in Fig. 5.2(b) results from these thin precipitates. The dark field image taken with a θ’ reflection at an orientation near <001> from the matrix (Fig.5.2c) indicates that the θ' phase appears to be approximately thin, square plates, where all of the edges are parallel to the {001} matrix planes, rather than circular, non-faceted disks.

A 3DAP reconstruction of two of these thin θ' plates (Fig.5.3) indeed reveals that these θ' plates are very thin (3nm) with broader faces larger than ~60nm in length. A one dimensional compositional profile through one of these plates (see Fig.5.3b) indicated that the composition of this phase is close to Al_2Cu as expected.

Fig.5.1 Bright field TEM micrograph in the as-cast condition showing the various interdendritic phase including silicon, iron containing intermetallic, and θ and Q phase.

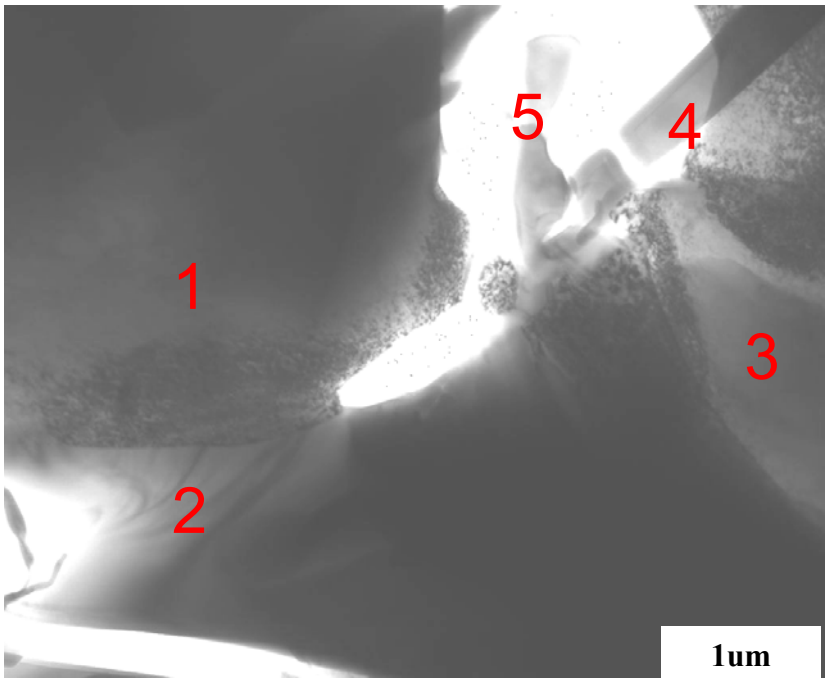

Table 5.1 Crystallographic and chemical composition data of selected phase in the Fig.5.1.

	Structure	Lattice parameter (A)	Composition
1	FCC	a = 4.04	$Al_{94}Si_2Cu_3Mg_{.1}$
2	BCC (α)	a = 12.56	$Al_{60}Fe_{10}Mn_{13}Si_{12}Cu_3$
3	BCT(θ)	a = 4.04 c = 5.8	$Al_{66}Si_1Cu_{33}$
4	HCP (Q)	a = 10.39 c = 4.01	$Al_{20}Cu_{10}Mg_{38}Si_{32}$
5	FCC	a = 5.4	Si_{99}

Fig.5.2 TEM results on the T6 conditions, (a) BF TEM micrograph, (b) SAD pattern, (c) DFTEM image showing the plate shape of θ' precipitate.

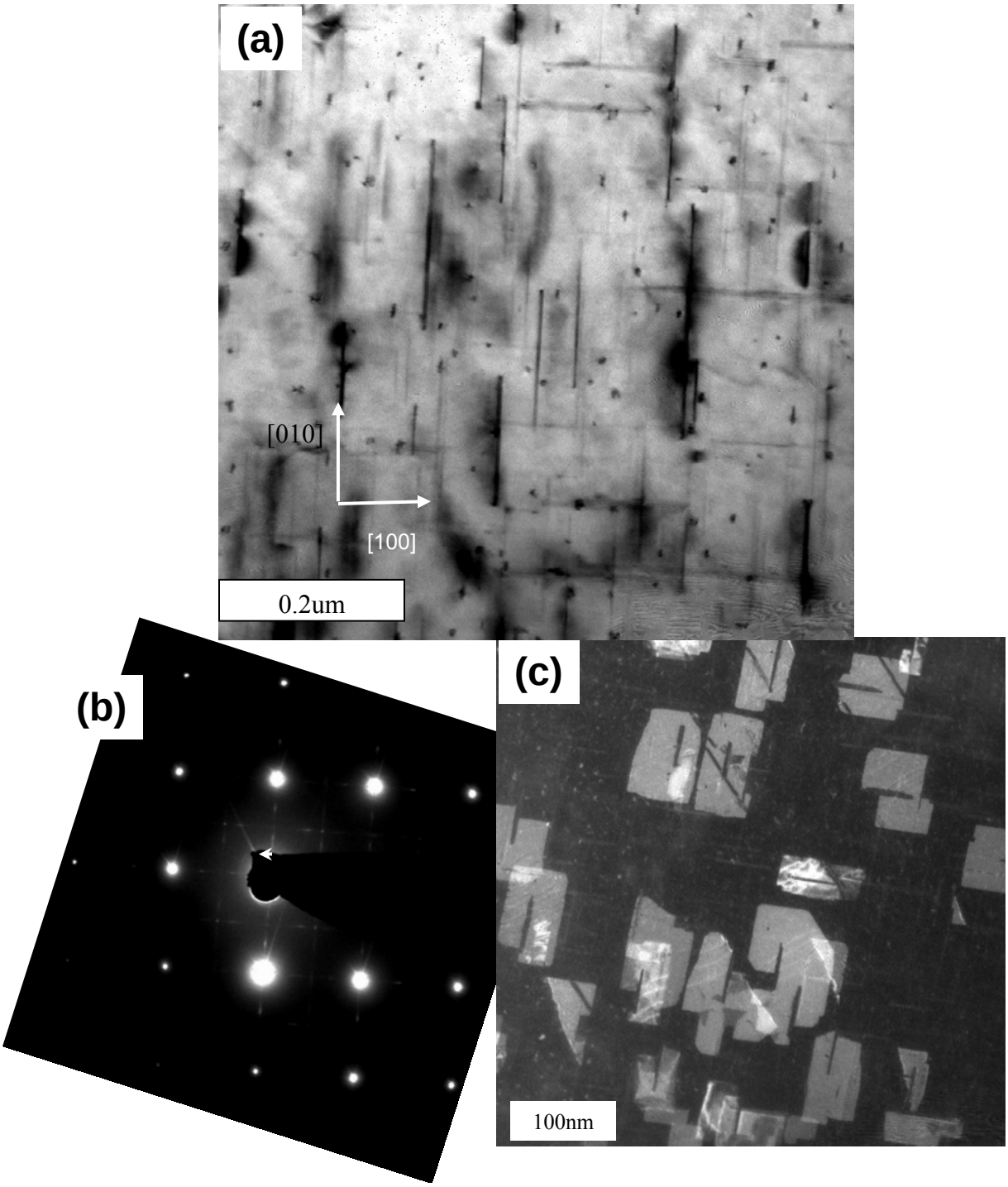

Fig.5.3 Three dimensional isoconcentration surfaces of the θ' precipitates in the modified 319 type aluminum alloy ages at T6 condition (a) and (b); Cu (green), Si (red), Mg (blue). The compositional profiles through the θ' phase along the cylindrical line is shown in (c).

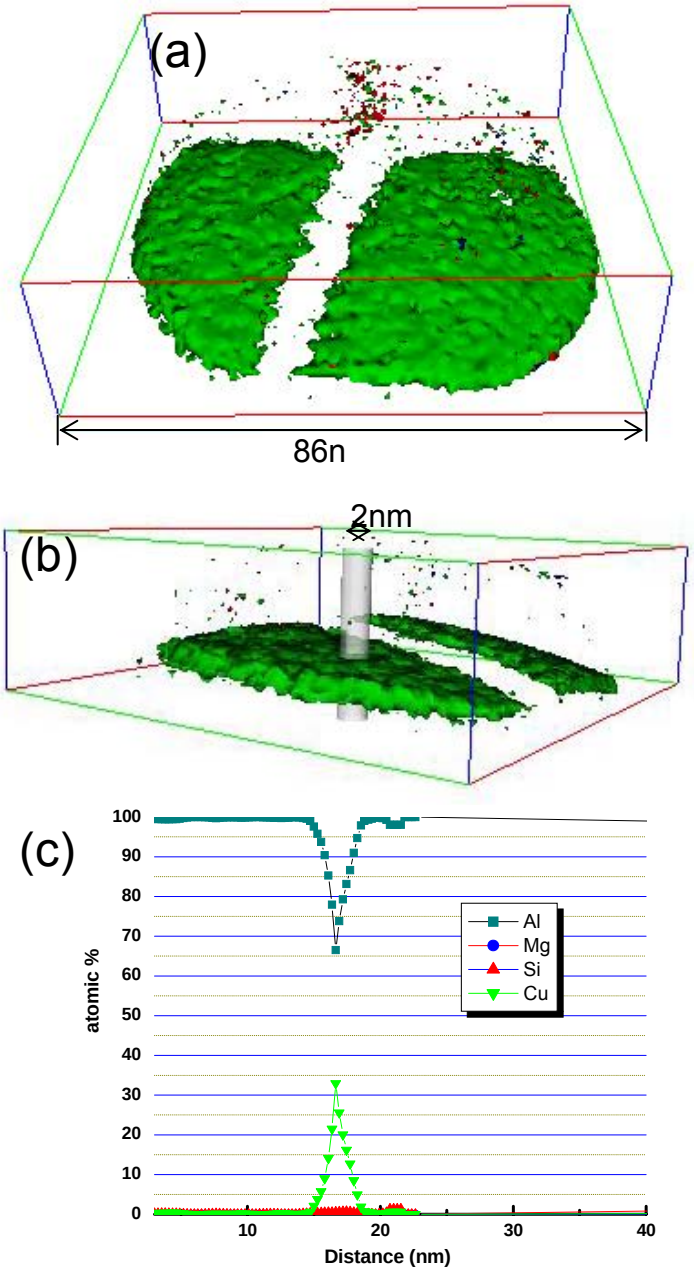

The smaller, lath-shaped precipitates were examined using scanning transmission electron microscopy (STEM), EDS (Fig.5.4) and high resolution TEM (Fig.5.5). Because these precipitates are considerably smaller than typical TEM foil thicknesses, it is difficult to obtain easily interpretable phase contrast images, diffraction patterns or composition analyses in the TEM given that the surrounding matrix material cannot be readily excluded. Even so, it is possible to note that these lath-shaped precipitates contain Al, Cu, Si, and Mg. Further, it is clear that the precipitates are probably cylindrical in shape where the cylinder diameter is approximately 5-6 nm with lengths on the order of 10–12 nm. These characterization challenges appear to be the reason for some of the confusion in the literature surrounding the identification of fine scale precipitates in both wrought and cast aluminum alloys. Indeed, the metastable phases in the quaternary Al-Mg-Si-Cu system have been variously reported as different phases with different stochiometries [9-12].

3DAP analysis of a tip containing both θ' plates and fine-scale precipitates (Fig.5.6) reveals that the larger precipitate is θ' whereas the two smaller precipitates contain mostly Al, Cu, Mg, and Si. Recently, Chakrabarti and Laughlin summarized the phase fields of the quaternary Al-Mg-Si-Cu system and the precipitation sequences of the metastable and equilibrium phases [13]. According to them, the Q' phase is a metastable version of the Q phase and has a lath-like morphology. Further, they reported that the Q' phase and the equilibrium Q phase have the same hexagonal crystal structure. In addition, the Q' phase is likely to maintain the crystal structure and morphology from the peak aged through the overaged conditions. Thus, it appears that the metastable phase in our study is the Q' phase even though there are still some

Fig.5.4 STEM micrograph showing the lath-shaped precipitates (a), and EDS spectra (b) obtained from white arrow containing Al, Cu, Si, and Mg.

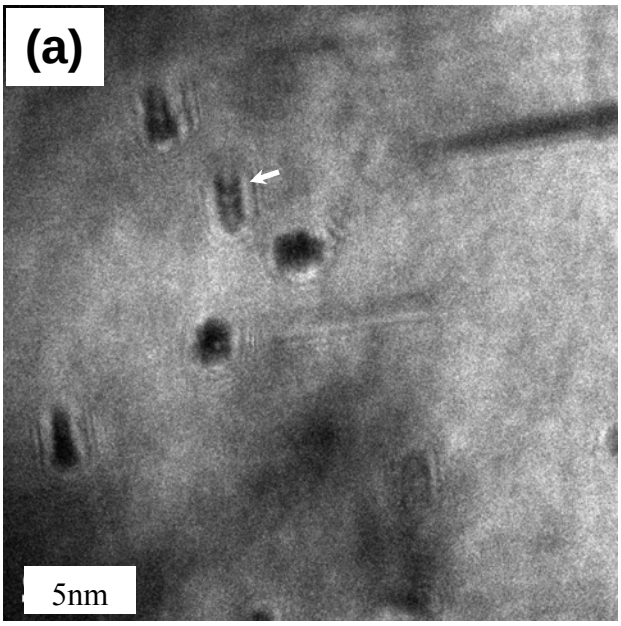

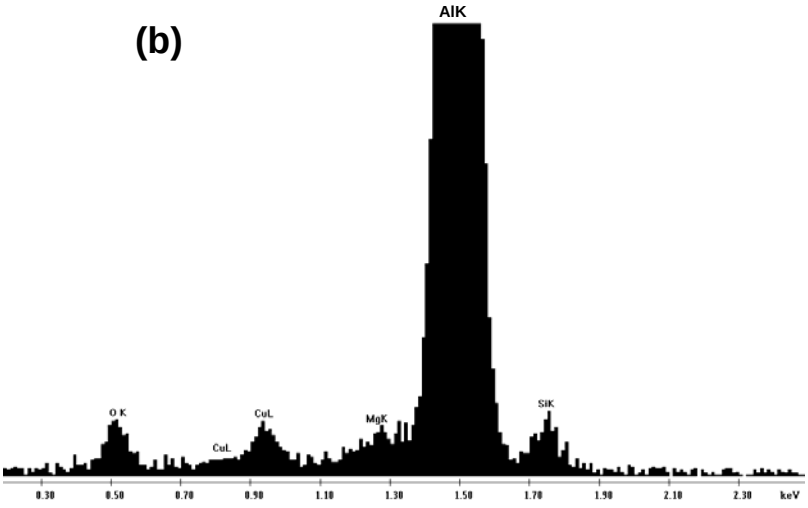

Fig.5.5 HRTEM images showing the two variants of lath-shaped precipitates.

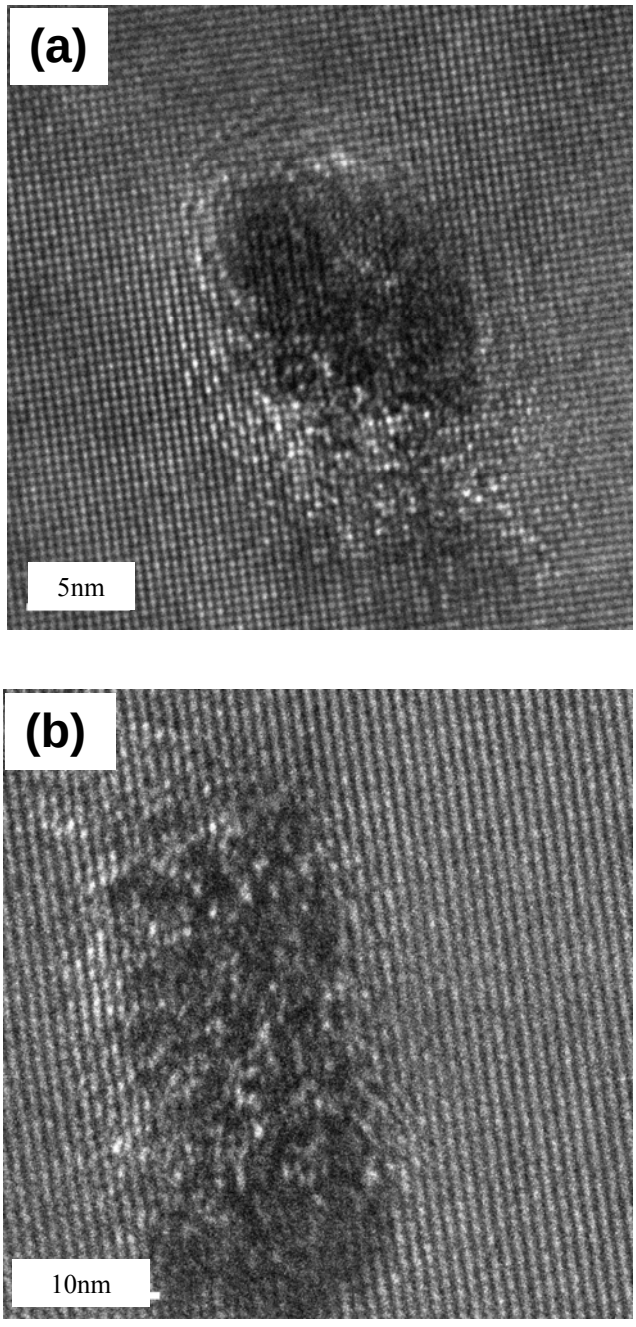

Fig.5.6 Three dimensional isoconcentration surfaces of the θ' and Q' precipitates showing two different view direction in the modified 319 type aluminum alloy ages at T6 conditions; Cu (green), Si (red), Mg (blue).

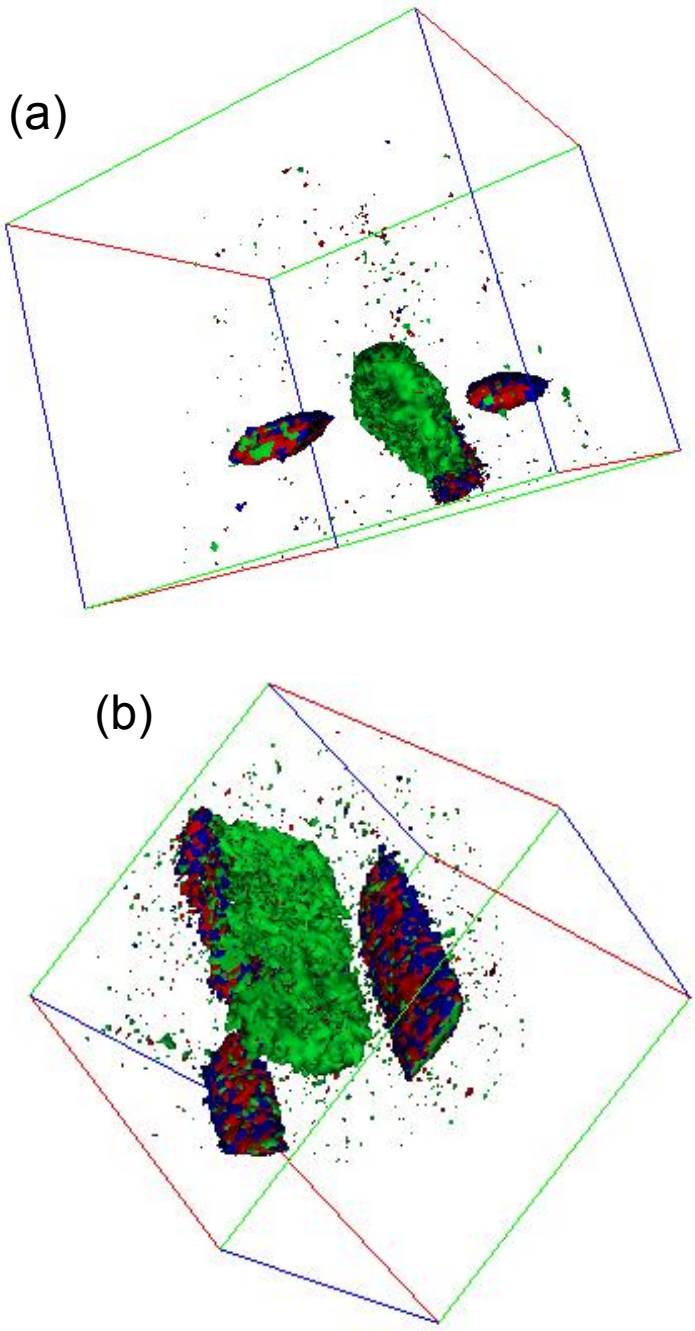

slight differences between the reported compositions and morphology. Wolverton suggested that the composition of the Q type precipitates should be temperature dependent, which could explain the various compositional differences reported for the Q phase and confusion arising from the use of different nomenclatures in the same phase [12].

The isoconcentration surfaces shown in Fig.5.7 indicate that these precipitates contain Al, Cu, Si and Mg. Given that the Q phase in the interdendritic regions also has these 4 elements in a similar ratio to that reported by Mondolfo, namely, $Al_4Cu_2Si_5Mg_8$ [14], it is not surprising that this phase is structurally similar. In fact, some authors have reported that this phase has the same crystal structure, namely, hexagonal (space group $P\bar{6}$) with a=1.039 nm and c=0.402 nm. The reported orientation relationship between Q and the matrix is

$$[0001]_Q \text{ // } [001]_{Al} \text{ and } [11\underline{2}0]_Q \text{ // } [510]_{Al}$$

Given that the c-axis of the Q phase is similar to the lattice parameter of Al, it has been argued that the c-axis should align along the cube axis of the matrix [10] in order to minimize strain energy. These precipitates have also been reported to have {510} habit planes, which have been related to the similar repeat distances alone these planes in the two structures [13]. From the atom probe tomography in Fig.5.7, it appears that there may have been heterogeneous nucleation of the θ' plates on the edge of Q' laths. It should be an evidence of the Q' phase as a strengthening ability. The lath-shaped Q' precipitates play a significant role as a not only hardening phase but also increase the heterogeneous nucleation site. It might be good evidence with Gao et al., who suggested the significant increase of the number density of θ' plates in the Al-4Cu-

0.3Mg-0.5Si alloy compared to a silicon-free alloy [15]. They suggested lath-like Q precipitates when only observed in the presence of Si in their literature may provide heterogeneous nucleation sites for θ' phase. We think their lath morphological phase seems to be close to our lath-shaped precipitate. Thus, it should be metastable Q' precipitate or precursor phase of equilibrium Q phase. For the careful investigation of this quaternary phase, Q type precipitate the systematic investigation on the aging process is underway from the initial stage of aging to overaged condition. The effect of the Q' precipitate on the mechanical properties is addressed by experiment observation in the previous chapter. In addition, the theoretical model based on the capsule type precipitate will be addressed in appendix 2.

The results indicate that the θ' phase in these alloys is mostly Al_2Cu with little evidence of any other components. Likewise, the finer precipitates appear to be quaternary in nature and have been designated Q' to be consistent with previous investigators. These small precipitates appear to be lath-shaped with their lath axis slightly misaligned from the <001> matrix directions- further work is needed to fully understand the basis for this orientation relationship.

Fig.5.7 Compositional profiles through the θ' phase (mark 1) and Q' phase (mark2) along the cylindrical line.

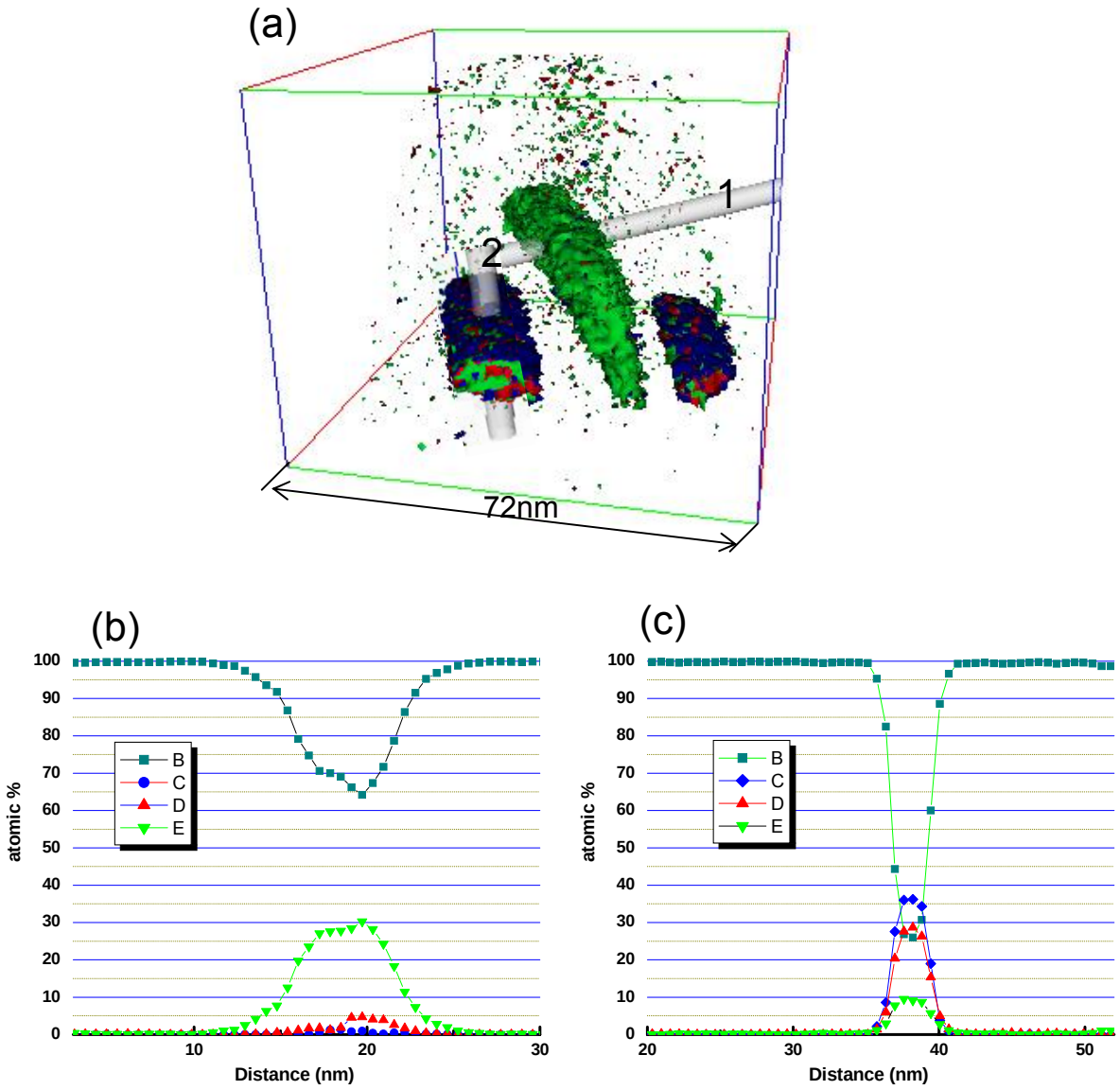

5.4 Reference

[1] M.K. Miller, Surf. Interface Anal. 31(2001)593.

[2]S.P. Ringer, Mater. Sci. Forum, 519-521(2006)25.

[3] S.P. Ringer, K. Hono, Mater. Char. 44(2000)101

[4] J.E. Hatch, Aluminum: Properties and Physical Metallurgy, ASM, 1984.

[5] P. Ouellet, F. H. Samuel, J. of Mater. Sci, 34(1999)4671.

[6] R.K. Mishra, G.W. Smith, W.J. Baxter, A.K. Sachdev, V. Franetovic, J. Mater. Sci. 36(2001)461.

[7] J.Y. Hwang, H.W. Doty, M.J. Kaufman. TMS letters, 3(2006)39.

[8] R. Jahn, W. Donlon, J.E. Allison, Automotive Alloys, 1999, TMS, pp.247.

[9] C. Cayron, L. Sagalowicz, O. Beffort, P.A. Buffat, Phil. Mag. A, 79(1999)2833.

[10] G.C. Weatherly, A. Perovic, N.K. Mukhopadhyay, D.J. Lloyd, D.D. Perovic, Metall. Mater. Trans. 32A(2001)213.

[11] K. Matsuda, Y. Uetani, T. Sato, S. Ikeno, Metall. Mater. Trans. 32A(2001)1293.

[12] C. Wolverton, Acta Mater. 49(2001)3129.

[13] D.J. Chakrabarti, D.E. Laughlin, Pro. Mater. Sci. 49(2004)389.

[14] L.F. Mondolfo, Aluminum Alloys, Structure and Properties, Butterworths, London, 1976.

[15] X. Gao, J.F. Nie, B.C. Muddle, Mater. Sci. Forum, 217-222(1996)1251.

CHAPTER 6

MICROSTRUCTURAL EVOLUTION IN LOW-Si 319 TYPE ALUMINUM ALLOYS

6.1 Introduction

The quaternary Al-Cu-Mg-Si system constitutes diverse alloy groups including the 2xxx, 6xxx and3xx series alloys. Compared to binary and ternary systems, quaternary systems frequently display increasingly complex precipitation sequences [1]. The addition of small amounts of alloying elements can significantly alter the precipitation kinetics and aging sequences [2-4]. From the industrial point of view, the modification of alloy compositions is favorable if it enhances the mechanical properties without increasing cost. Among those aluminum alloys, type 319 aluminum casting alloys have been attractive due to their reasonable strength and their thermal stability at the slightly elevated temperatures found in automotive engine applications [5]. Recently, GM Powertrain developed 319 alloys with much lower silicon contents (only 1 wt. Pct. Vs. the standard 7%); these alloys exhibit greater ductilities without a loss of strength. The enhanced ductilities are attributed to the decreased amount of the brittle eutectic Si phase. However, the aging behavior of these modified alloys is not clearly understood. Given that the strength is largely influenced by the precipitate shape, distribution, and volume fraction in the matrix, it is important to understand and control the precipitation behavior. Generally, the precipitation hardening behavior in Al-Cu-Mg alloys depends on the composition in the aluminum-rich corner of the Al-Cu-Mg phase diagram in Fig. 6.1. [6]. While Cu promotes the formation of the stable θ-Al_2Cu phase and the various metastable variations, Mg leads to the formation of the stable S-Al_2CuMg phase and

Fig.6.1 Ternary phase diagram of aluminum rich corner of the Al-Cu-Mg system showing the phase fields as a function of compositions after long term aging at 190°C. The thick solid line represents the (α+S) phase boundary at 500°C.

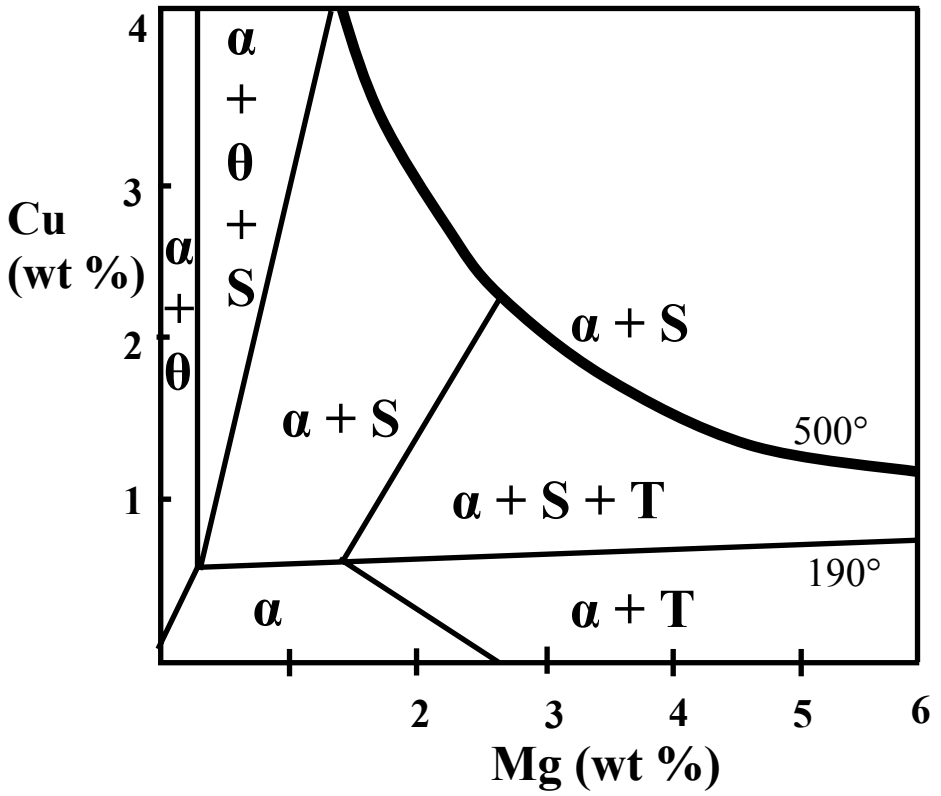

various metastable precipitates that are complex and that have led to confusing nomenclature in the literature [7-10]. Eskin summarized the reported variations in the crystallographic and morphological characteristics of the precursor and metastable phases in the Al-Cu-Mg system [1]. The confusion stems from the difficulty in identifying the structures and compositions of the very small metastable phases involved in the strengthening. Furthermore, additional alloying elements cause the precipitation process to become more complicated [2-4,11-18]. An important example is the effect of a small amount of Ag (~0.2 %) which is known to result in the formation of a hexagonal precipitates of a "Ω"-Al_2Cu phase on {111} Al planes [11] at the expense of the θ' phase. The nucleation mechanism of the Ω phase in the presence of Ag is not yet revealed.

In the case of Si additions to Al-Cu-Mg alloys, the precipitation behavior becomes more complex. According to Hutchinson, small amounts of silicon are incorporated into GPB (Guinier-Preston-Bagaryatskii) zones and also cause a slight refinement in the uniformly distributed S' (Al_2CuMg) type metastable precipitates [2]. However, there remains some controversy on the specific role of Si on the precipitation process and on the dominant hardening phases representing the σ ($Al_5Cu_6Mg_2$) [19], and Ω phase [13]. Therefore, the identification of the precipitates in this system is very important for understanding the microstructural evolution and for and for optimizing the process parameters during thermal heat treatment for high temperature engine applications in this new alloy system. Although transmission electron microscopy (TEM) can provide information concerning the nanoscale precipitates, it is limited when it comes to providing true atomic scale composition information. Currently, 3D atom probe (3DAP) tomography is an ideal method for quantitative analysis of solute clusters and GP/GPB

regions. The advantage of 3DAP analysis combined with high resolution transmission electron microscopy is that it is possible to verify the 3D morphology and compositions at atomic resolution.

The purpose of this study is to examine the microstructure and compositions of the nanoscale precipitates in low Si 319 type casting alloys using both analytical HRTEM and 3DAP.

6.2 Experimental Procedure

The alloy was obtained from GM Powertrain at Metal Casting Inc. The compositions of the alloy used in the present study are shown in Table 6.1. The alloy was solution treated at 488°C for 8 h and then quenched in warm water. The subsequent aging treatment was carried out at two different temperatures. For the peak aging treatment (T6), aging was conducted at 193°C for 8 hours. Some samples were also given a stabilizing treatment (T7) at 223°C for 4h. The microstructures of the aged samples were examined by transmission electron microscopy using a Philips EM 420, and high resolution transmission electron microscopy using an FEI TECHNAI F20 equipped with energy dispersive X-ray spectroscopy (EDX). The thin foil specimens for TEM analysis were prepared using a twin-jet electro polishing unit technique in a 33% nitric acid –methanol solution at –20°C. Before the TEM observations, plasma cleaning was carried out on the thin foil specimens to prevent artifacts from surface contamination.

The 3DAP analysis was performed using the local electrode atom probe (LEAP) system from IMAGO. The sharp needle specimens for the atom probe analysis were prepared using a NOVA 200 dual focused ion beam (FIB); these needles had less than

70nm end tip radius and were attached to Si microtips. The sample prepared by FIB on the Si microtip was shown in Fig.6.2. The atom probe analyses were carried out using the voltage mode at ~ 50K. Details of the analysis conditions for the atom probe experiments are summarized in appendix1.

Table 6.1 Composition of the alloy used in the present study.

	Al	Si	Cu	Mg	Fe	Mn	Sr
Amount (wt. %)	Bal.	0.927	3.47	0.42	0.48	0.68	0.01

Fig. 6.2 Scanning electron micrographs of the atom probe specimens prepared on the Si microtip (a), and the high magnification image on the edge (b).

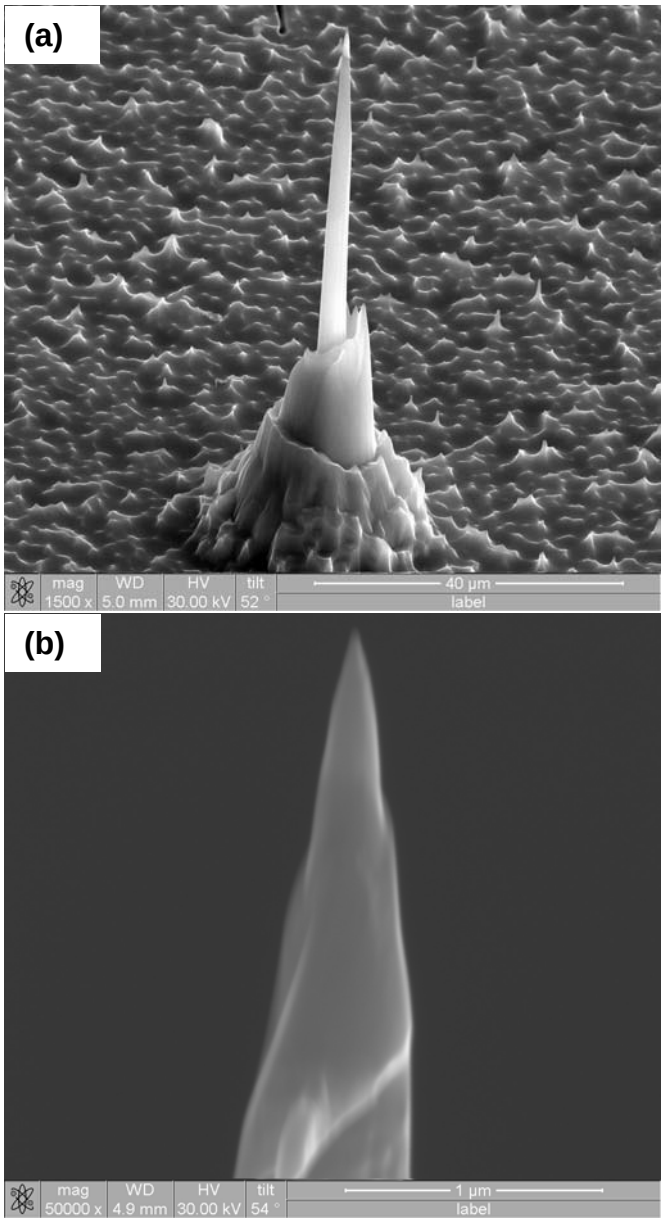

6.3 Results and Discussion

6.3.1 Observations of T6 Samples

Transmission electron microscopy studies (Fig. 6.3) of the T6 sample revealed that there two dominant hardening phases in the matrix. As can be seen, there are plate-like precipitates aligned along the {100} planes of the Al consistent with the streaking in the SAD pattern (Fig.6.3(c)). These metastable θ' precipitates are tetragonal with a=0.4nm, c=0.58nm. The dark field image obtained using the streaked intensity along $(020)_{Al}$ is shown in Fig. 6.3(b). In this alloy system, the θ' precipitates are randomly distributed in the matrix when compared with the second, much smaller precipitates that can also be seen in these images. The high resolution transmission electron micrographs in Fig. 6.4 show well aligned $(002)_{\theta'}$ planes with $\{200\}_{Al}$ planes with a $<100>_{Al}$ // $<100>_{\theta'}$ and $\{001\}_{Al}$ // $(001)_{\theta'}$ orientation relationship. The θ' precipitates have {001} Al habit planes. These results are in good agreement to typical θ' precipitation behavior in Al-Cu binary alloys.

The much finer precipitates in Fig. 6.3 are also aligned along the $<001>_{Al}$ matrix directions. In order to investigate the morphological shape of these fine precipitates, the sample was tilted to a $<011>_{Al}$ direction (Fig. 6.5). As can be seen in the BF and DF TEM images in Fig. 6.5, these precipitates appear to be very short rods (inside circle in Fig. 6.5(a)). The rod shape precipitates are very small, uniformly distributed and aligned along $<100>_{Al}$ directions. The dark field image developed around $(110)_{Al}$ matrix reflections-marked by A in Fig. 6.5(b) is represented in Fig. 6.5(c). From Fig. 6.5 (a) and (c), the fine rod-like particles display weak contrast compared to the plate shape θ' phases which are shown at Fig. 6.5(d) using the $(002)_{\theta'}$ diffracted beam (marked by B in

Fig.6.3 TEM micrographs and corresponding SAD pattern of the Al-Cu-Mg-Si alloy aged at 198°C for 8 h (T6 condition) near the <001> Al direction. Note the plate shaped θ' precipitates lying on the $\{100\}_{Al}$ planes.

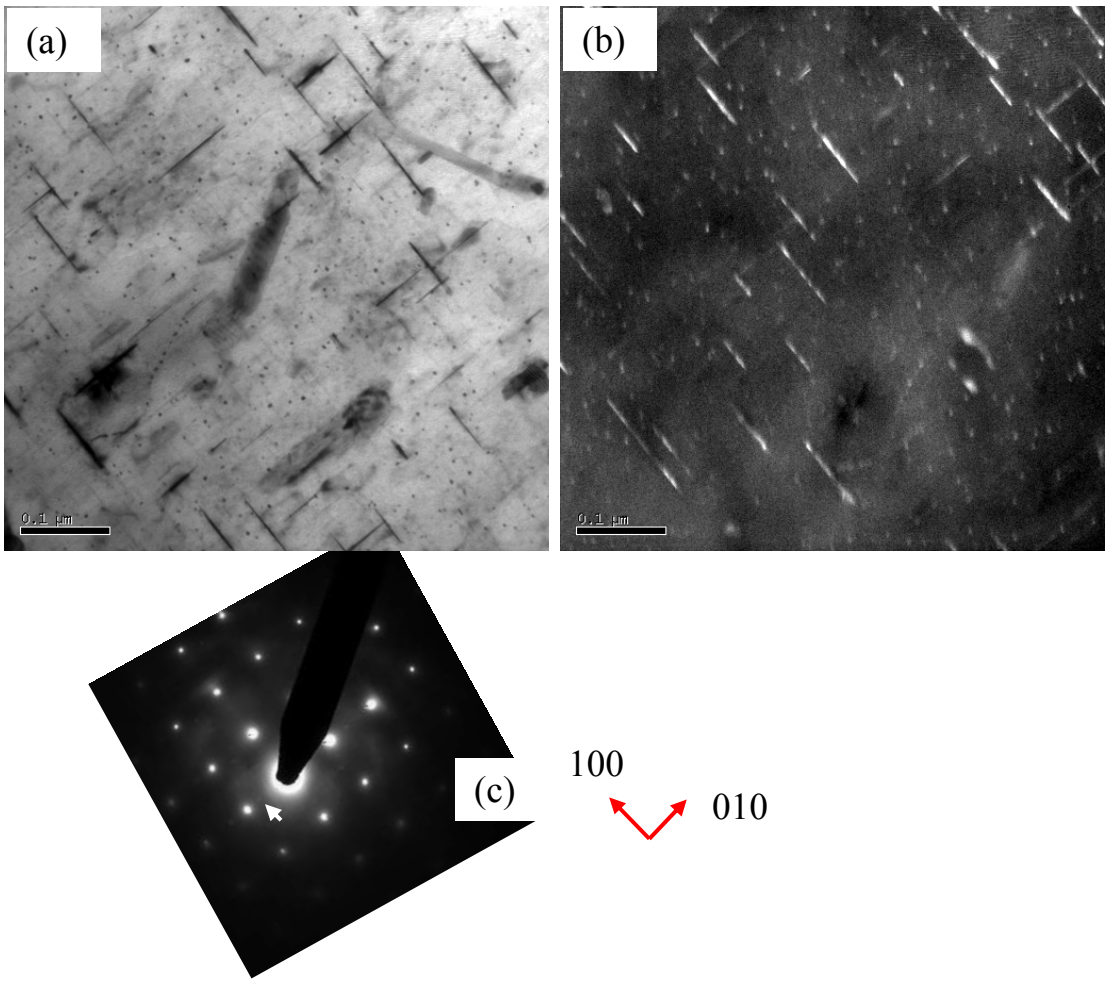

Fig.6.4 High resolution TEM micrographs and corresponding FFT spectrums on the θ' precipitates of Al-SI-Cu-Mg alloys aged at 198°C for 8 h along the (a) [001]Al, and (b) [011]Al beam direction.

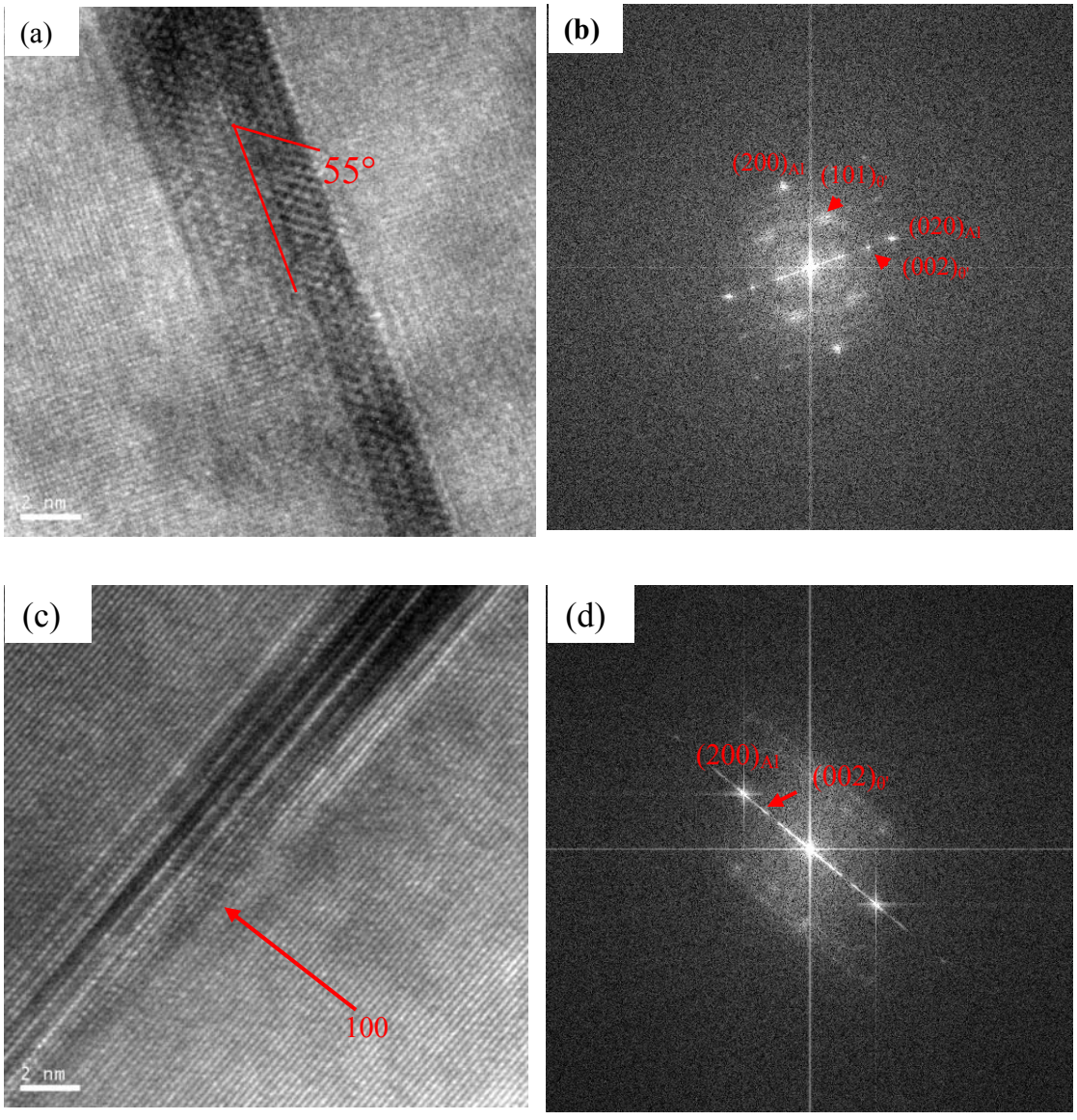

Fig.6.5 Transmission electron micrograph, in <110> Al orientation showing the presence of θ' phase and GPB zone. (a) BF TEM image and corresponding SAD pattern (b), and dark field images obtained using the streaks marked by A and B along the <001>Al direction in (c) and (d).

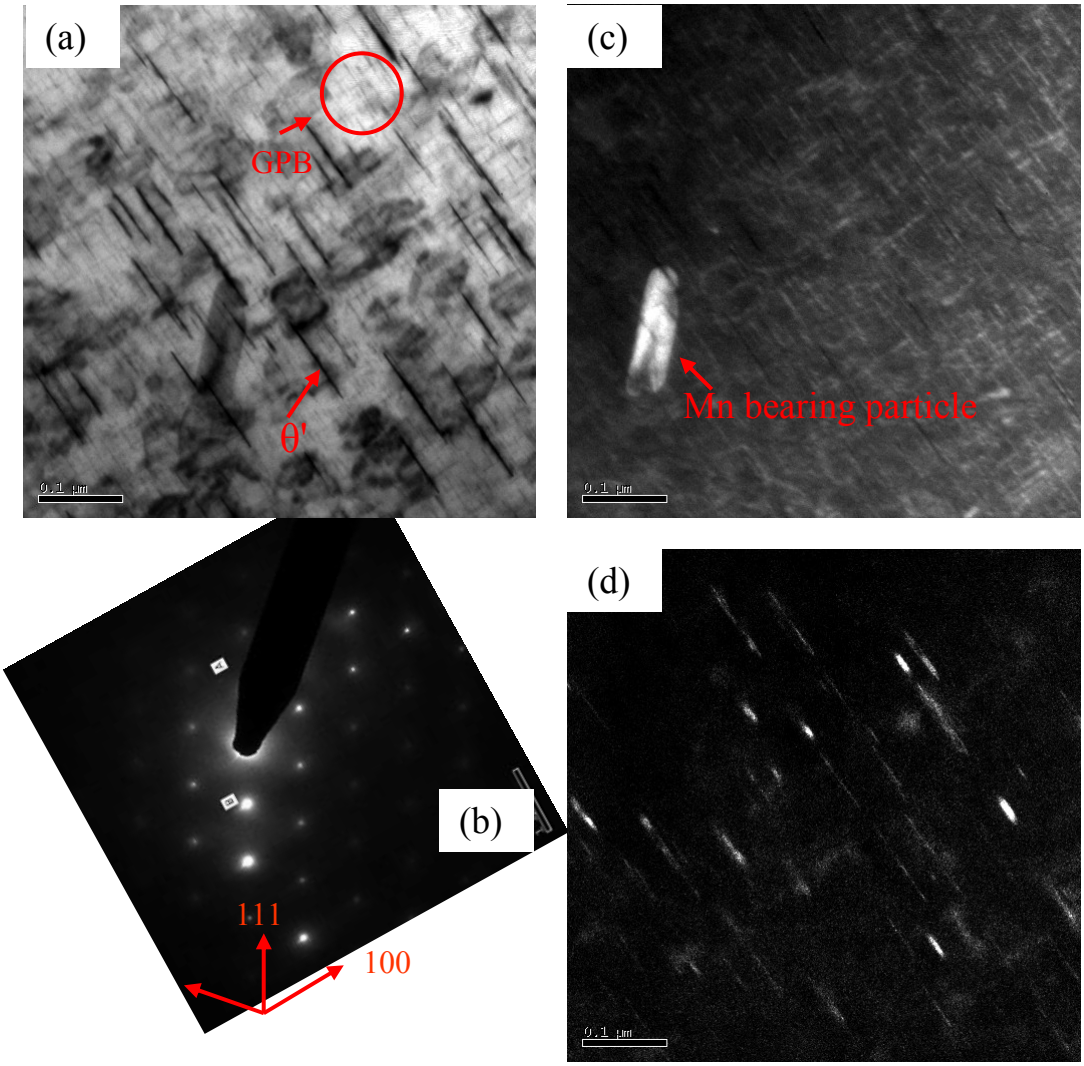

the Fig. 6.5(b)). The intensities of the reflections from the small rod-like precipitates were too weak to use to identify their crystal structure.

The morphological shape and SAD pattern of these rod-type precipitates are similar to the reported GPB zones in ternary Al-Cu-Mg alloys [18-19]. Similar observations were reported by Hutchinson and Ringer [2] in Al-Cu-Mg alloys containing 0.5 wt.% Si. Based on their observations, these GPB zones have a slight difference in morphology and composition with the typical GPB zones reported by Silcock [23]. Accordingly, they referred to these small rod-shaped precipitates as Si-modified GPB zones instead of introducing new nomenclature. Thus, it is reasonable to follow the terminology of the Si-modified GPB zone until we clearly identify this phase.

A more detailed investigation was carried out on the Si modified GPB structure using the HRTEM and 3DAP. A HRTEM image (Fig. 6.6) taken along an $<001>_{Al}$ direction reveal clear lattice fringes and a particle that is approximately 2nm in diameter. However, in the Fast Fourier Transform (FFT) it is difficult to distinguish strong periodic ordering for this Si-modified GPB zone. This might be related to random manner of solute atom clusters with Cu, Mg, and Si atoms in the Si modified GPB zones.

The 3DAP reconstructions and composition profiles in Fig. 6.7 reveal the two distinct precipitates. The composition analyses of these two precipitates indicate that the plates are indeed the θ' phase while the small rods are the Si-modified GPB zones consistent with our TEM results. From the composition profile, the Si-modified GPB zones are composed of approximately 70 at%Al-10 at%Cu-10 at%Mg, and 10 at% Si. The ratio of Cu, Mg, and Si is 1:1:1. This unique compositional measurements of Si-modified GPB zones appears to be the first to date. Therefore, we suggest that the Si

modified zones exist as short rods that are 2nm in diameter and 50nm in length and are aligned along the $<001>_{Al}$ matrix directions. Further work is clearly needed to determine the crystal structure of these Si-modified GPB zones.

The arrow in Fig. 6.5(c) points to a Mn-containing particle. Even though there is not much of large number density of these Mn-containing particles, they are readily observed inside the aluminum matrix and they tend to be either globular or lath-like along $<110>_{Al}$ (see Fig. 6.8(a)). The SADPs in Fig. 6.8 indicate that both morphologies of the Mn-containing phases have the same crystallographic structure as the α phase, namely cubic ($Im\bar{3}$) with a= 1.25nm, observed in the as-cast 319 alloys containing Mn (discussed in Chapter 3). EDS analysis indicated that these particles contain more than 10 at% Mn. However, unlike the interdendritic α phase, these particles contain negligible amounts of iron. The orientation relationship with the matrix and the morphological characteristics are still under investigation. Interestingly, the globular-shaped particles appear to act as heterogeneous nucleation sites for the Al_2Cu-type precipitates. A more detailed examination of the Mn-containing particles will be described in the next following chapter.

Fig.6.6 High resolution TEM micrograph and corresponding FFT spectra on the rod type precipitate of Al-Cu-Mg-Si alloy aged at 198°C for 8 hours along the $<001>_{Al}$ direction.

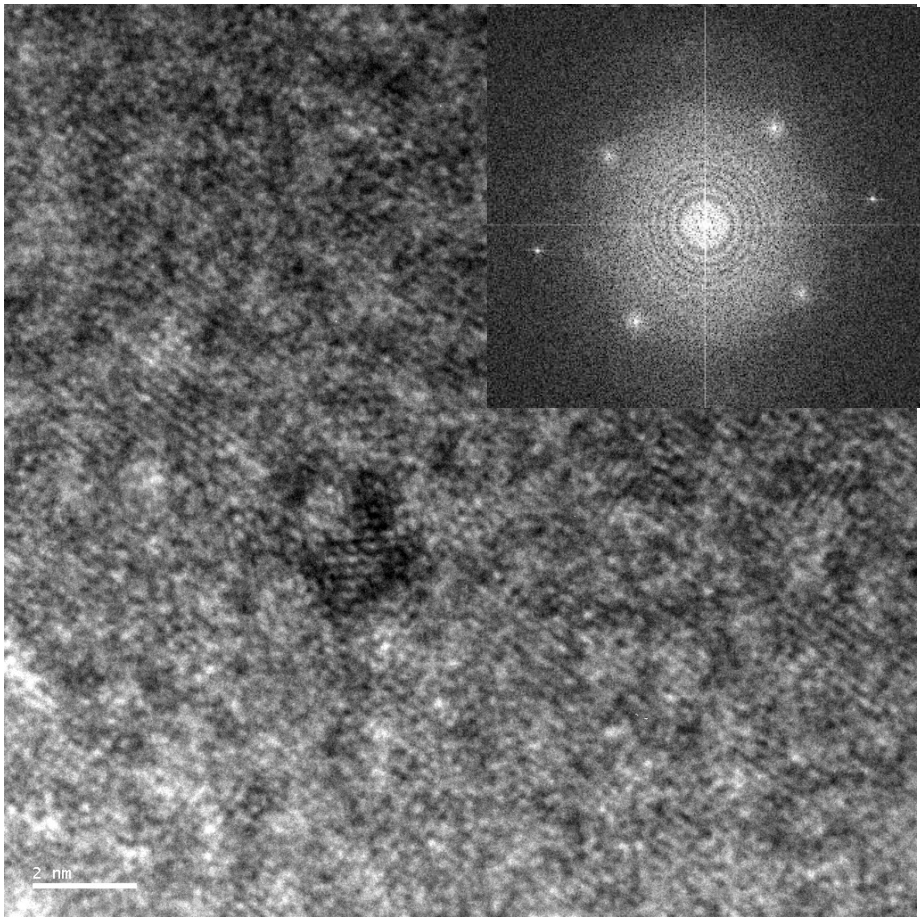

Fig.6.7 3DAP reconstructions of two different shapes of precipitates and their compositional profiles. Red, green, and blue represent silicon, copper, and manganese, respectively. Aluminum is not shown in the reconstructed images.

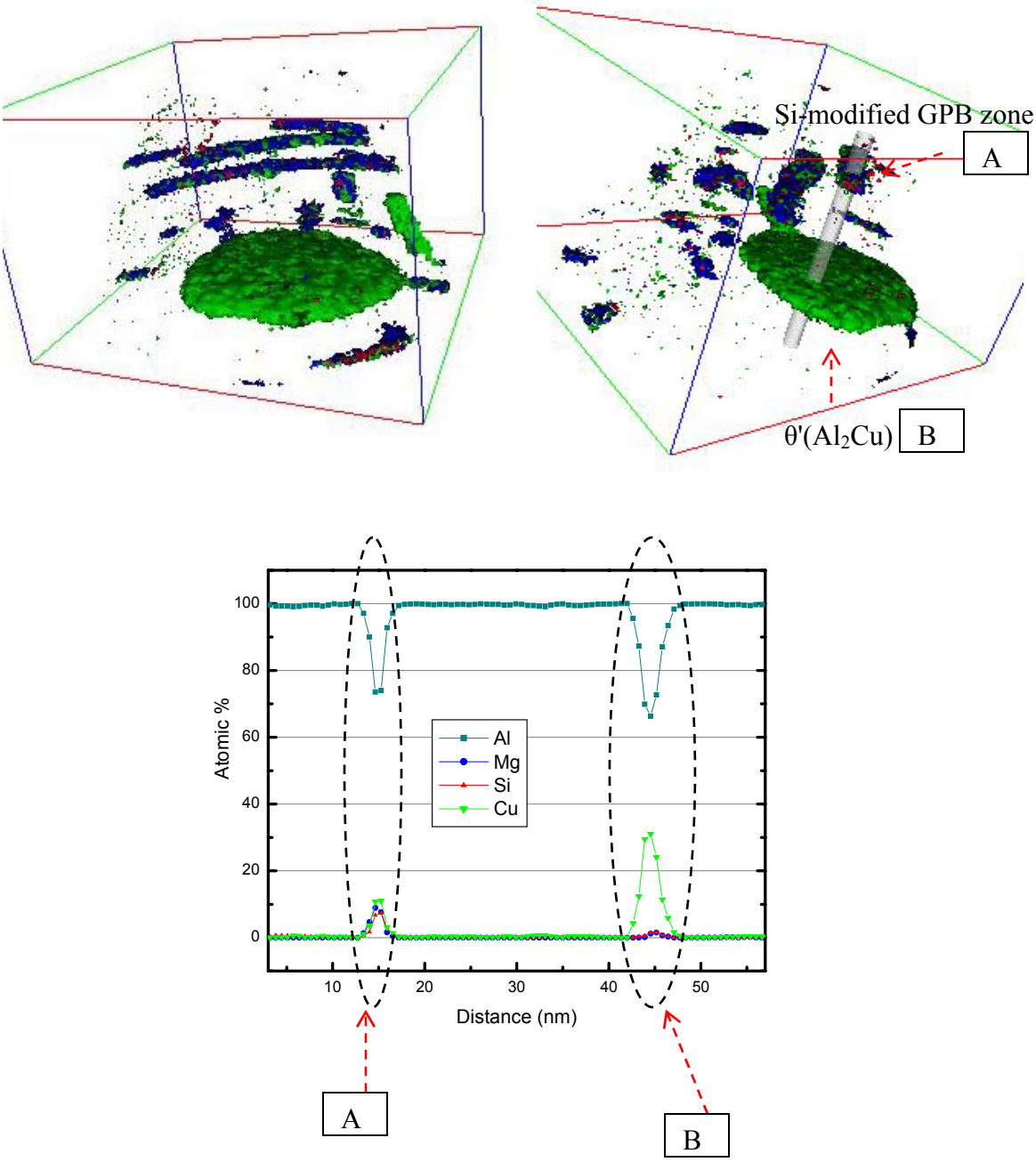

Fig.6.8 Transmission electron micrographs on the Mn containing particles. (a) lath shape particles along the <011> Al direction, (b) and (c) large globular shape particles with random oriental relationship with matrix.

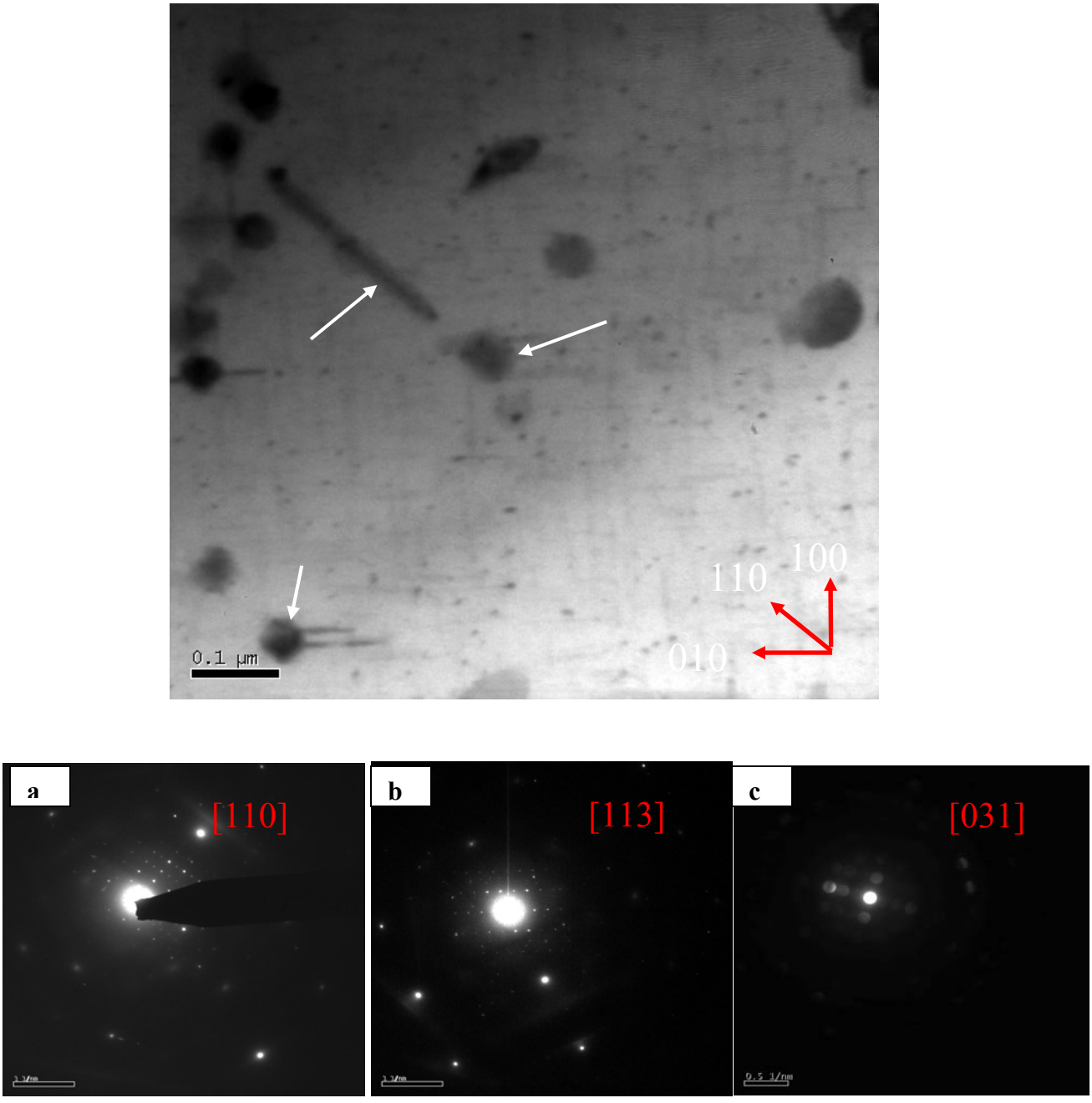

6.3.2 Observations of T7 Samples

6.3.2.1 Si-modified GPB2 Zone

The T7 samples also contained several different types of precipitates (Fig. 6.9). First of all, both the θ' and Si-modified GPB zones were observed along the $<001>_{Al}$ directions. In addition, both blocky shaped Al_2Cu in Fig. 6.9(a), and lath-shaped Al_2CuMg in Fig. 6.9(b) were observed. The nucleation of this these equilibrium phases are not relevant to the continuous growth from GP or GPB zones. The heterogeneous nucleation sites will assist the nucleation of these two equilibrium phases. However, these two equilibrium phases are rarely observed other than in specifically segregated regions of the sample. It is still considered that θ' and Si modified GPB zones are the major hardening phases even in the overaged condition. From the HRTEM and atom probe data, the structure and composition of the θ' phase are the same as those in the T6 condition. However, we found the Si-modified zones have grown and show slight differences when compared with those in the T6 condition. Thus, we called it Si-modified GPB2 zone.

Similar to the GPB zones, the GPB2 zones contain fine and uniformly distributed precipitates that are slightly elongated in the $<001>_{Al}$ direction (Fig. 6.9(b)). As can be seen in these figures, the Si-modified GPB2 zones are needle shaped with 2-4nm thickness and 60-100nm length. Again, these precipitates have different morphologies compared with the plate-like θ' phase and include considerable amounts of Si. The BFTEM and SADP from this material (Fig. 6.10a) reveal different types of precipitates including θ’ and the smaller GPB2 phase. From the DFTEM image in Fig. 6.10 (c), which was obtained using the $\{110\}_{Al}$ diffracted spot, it can clearly be seen that these

Fig.6.9 BFTEM near **B**=<001>$_{Al}$ showing the various precipitates after the T7 aging treatment. (a) Low magnification and (b) higher magnification showing the fine precipitates.

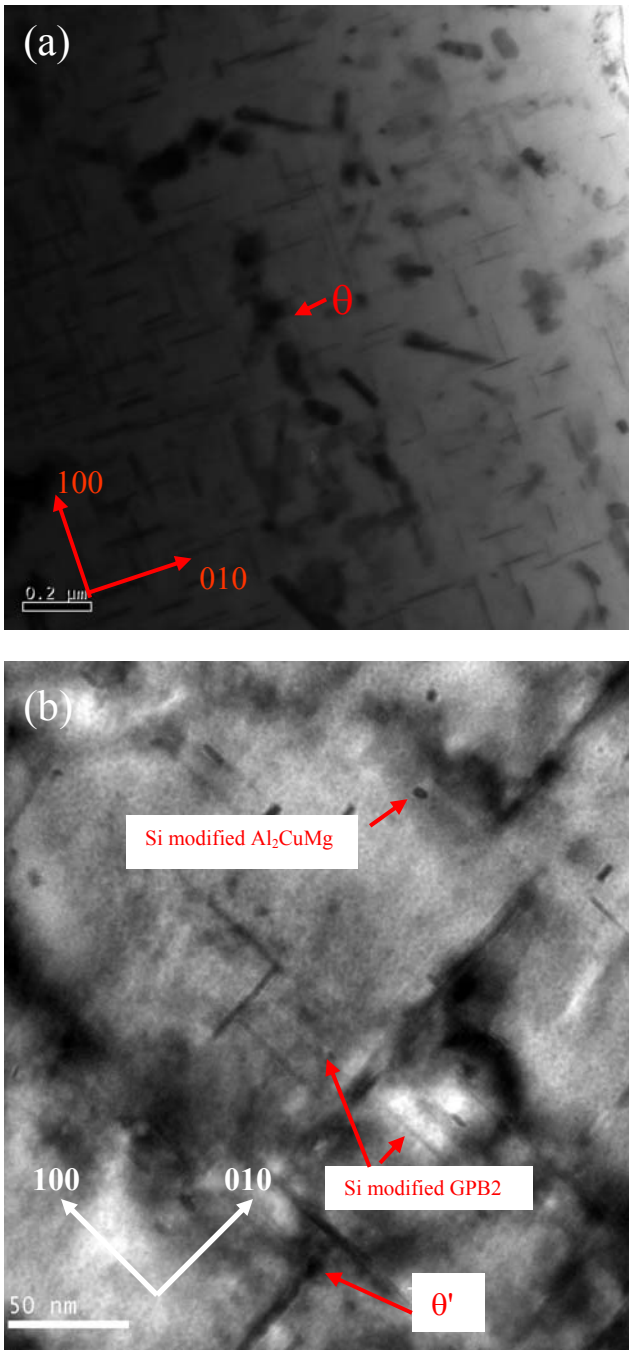

Fig.6.10 Transmission electron micrographs near **B=** $<112>_{Al}$ showing the presence of Si-modified GPB2 zone, (a) BFTEM image and corresponding SAD pattern and (b) dark field image obtained using the streaks marked by arrow along the $<011>_{Al}$ direction.

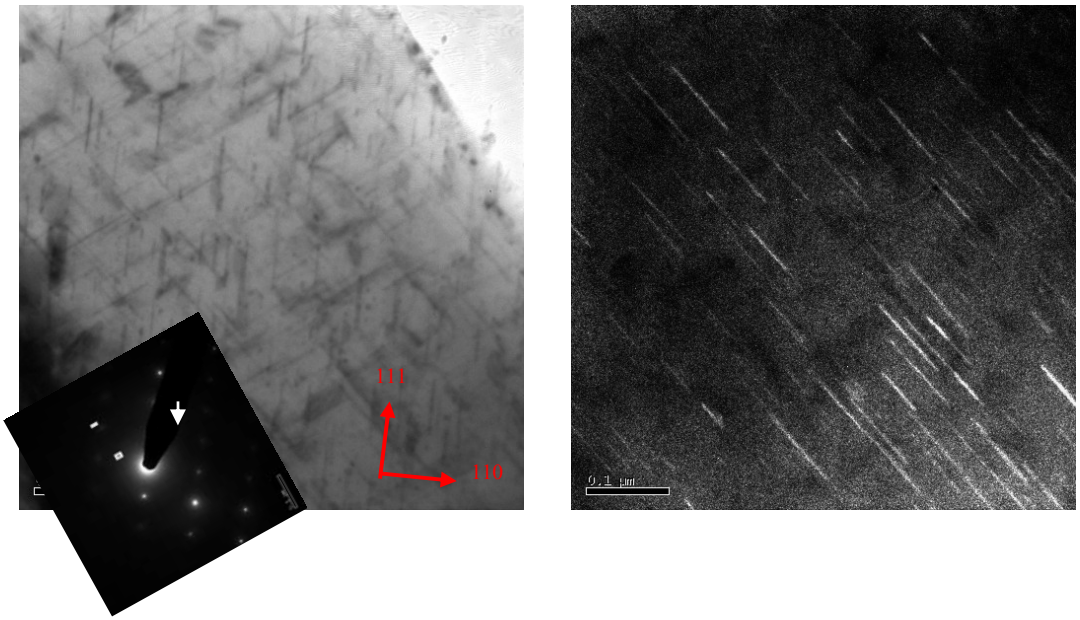

precipitates are rod shaped. The contrast of the Si-modified GPB2 zones is stronger than that of the Si-modified GPB1 zones. However, these precipitates have relatively weak extra reflections in the SAD patterns compared with those from the GP zones or θ' particles. This is related to the very thin widths of these particles. Thus, a more detailed examination was carried by HRTEM investigation. HRTEM images taken along the $<001>_{Al}$ zone axis are shown in Fig. 6.11. The end-on view of this precipitate in Fig. 6.11(a) indicates the sign of disordering of the lattice fringes and sign of typical ordering of in $\{120\}_{Al}$ are coexisted. It is possible to obtain better contrast in the HRTEM images, by aligning the particle ends along the <001> direction through the foil thickness in Fig. 6.11(a) when this phase lie along the <001> matrix direction in Fig. 6.11(b). Based on the experimental observations, it is clear that these particles have thin rod-type morphologies with facets along the $\{120\}_{Al}$. It is difficult to observe the specific interface except $\{120\}_{Al}$ interface. The FFT spectra from the Si-modified GPB2 zone show the streaks along the 220 directions in Fig. 6.11(b). The streaks probably originate from the thin faulted structure lying along the cube direction. Similar streaks were observed by Kovarik et al. in 5000 series aluminum alloys [10]. They proposed that the streaks were due to the small size of the plate-like particles oriented along the cube direction. However, careful examination of the morphology of the Si-modified GPB2 zone using 3DAP revealed them as rod-like precipitates. The atom probe results (Fig. 6.12) indicated that the composition of these precipitates is approximately $Al_{55}Cu_{15}Mg_{15}Si_{15}$. In other words the ration of Cu: Mg: Si is 1:1:1. This shows the similarity with the Si-modified GPB zones observed in the 6 condition with a slight increase in the Cu, Mg, and Si contents and decreasing Al content.

Fig.6.11 High resolution TEM micrographs and corresponding FFT spectra on the new precipitates of Al-SI-Cu-Mg alloys aged at T7 along the [001] Al matrix direction.

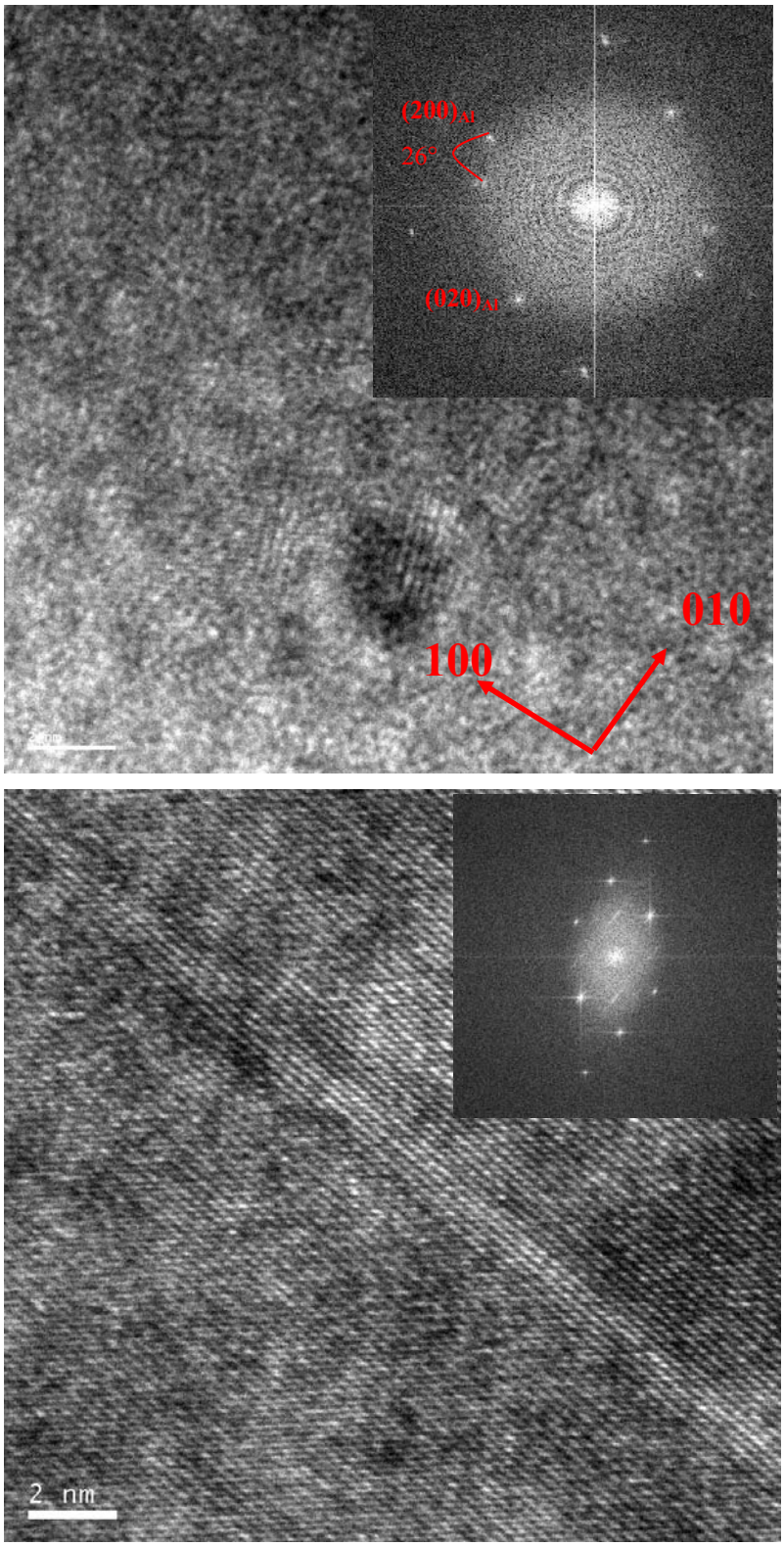

Fig.6.12 3DAP reconstruction results on the T7 aging treatment sample showing the rod type precipitates.

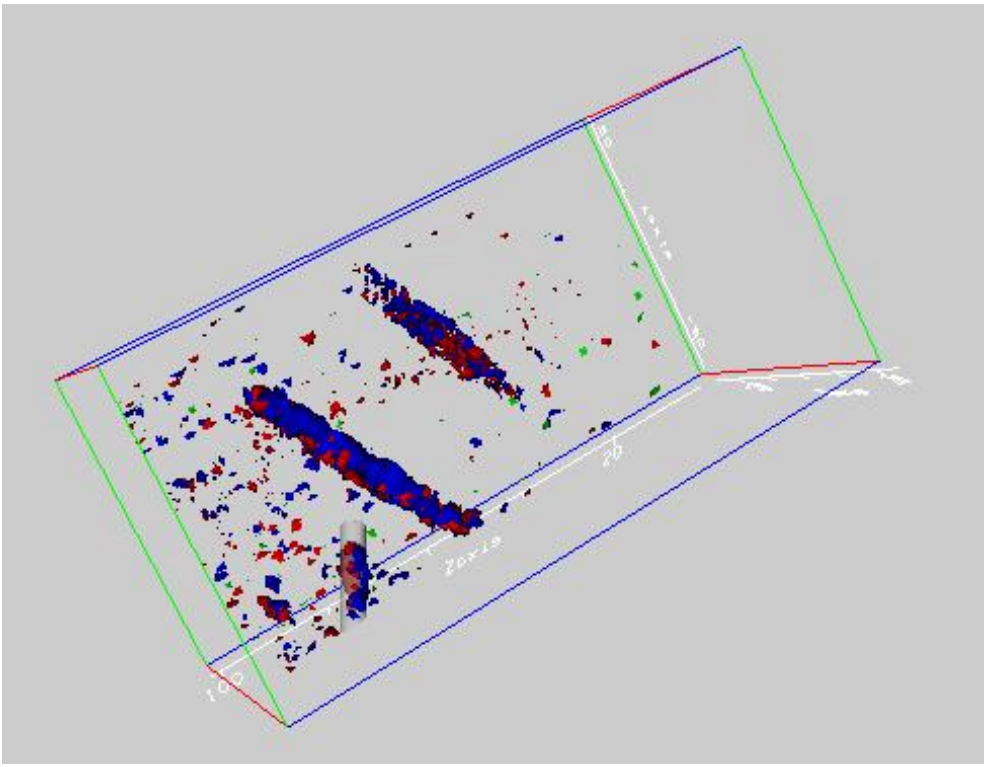

Based on our observations, this new precipitate phase has a similar morphology and Cu/Mg ratio that is similar to the S type (Al_2CuMg) precipitates. However, it is noteworthy that Si plays a quite significant role on the formation of these precipitates. There are number of structural variations in the microstructural evolution of Al-Cu-Mg alloys containing Si [2]. In addition, there is still the possibility of Q type precipitates even though no observations were made in this system. It is believed that the Si content plays an important role on the precipitation behavior. Detailed characteristics of the Q type precipitates are summarized in Chapter 4 on the high Si containing system.

There are still arguments concerning the terminology on the metastable phases during the microstructural evolution in Al-Cu-Mg alloy system. For example, there are some similarities between the S'' phase observed by Ratchev et al [21] and the present Si-modified GPB2 zones. However, the Si-modified GPB2 zones appear to have better ordering than the Si-modified GPB zones observed in the T6 condition. Second, we find no exact evidence from the SAD patterns associated with S'' or S' phase which means this phase is still underaged. Third, the chemical composition results via atom probe show the compositional similarity with Si modified GPB and GPB2 and totally different with S'' or some other type of precipitate such as Q type precipitate. We regard this Si-modified GPB2 zone is continuous sequence from the Si-modified GPB zone. Si-modified GPB zone is likely to retard the coarsening after forming (Cu-Mg-Si cluster) compared to GP structure (Cu rich cluster) and GPB zone (Cu-Mg cluster) even higher than 200°C. It is necessary to early stage of aging response on the GP and GPB structure in future study on the aging kinetics.

6.3.2.2 Al_2Cu and Si-modified Al_2CuMg Phase

In addition to the θ' and Si-modified GPB2 zones, both coarser and somewhat randomly distributed θ-Al_2Cu, and Si modified Al_2CuMg were observed in this alloy (Fig. 6.9). The number density of the Al_2Cu particles is small compared to the metastable θ' phase. However, it is noteworthy to nucleate of this equilibrium phase in this aging condition. Typically there is no report on the θ phase at this aging treatment around 220°C. Namely, it is necessary that the aging temperature is carried out above θ' solvus temperature in order to nucleate and grow of θ phase at grain boundary or θ'/matrix interface, or quite longer aging time is required. Recently, the Ω phase, a chemically-modified coherent form of Al_2Cu that nucleates on {111} habit planes, was observed in Al-Cu-Mg-Ag alloys [11-18]. Hono et al. suggested that Ω phase evolves from co-clusters to plate like precipitates continuously, rather than forming discretely by heterogeneous nucleation [11]. Kerry and Scott proposed that the Ag and Mg increase the density of {111} stacking faults by reducing the stacking fault energy, thereby Ω is heterogeneously nucleated [24]. Garg et al. found that the Ω phase occurs uniformly with no preference to defects [13]. They also proposed that the Ω phase has a tetragonal structure with a= 0.607nm and c= 0.496nm based on convergent electron diffraction results [5]. This result shows similar characteristics with the θ-Al_2Cu phase. However, the mechanism of nucleation of the Ω-Al_2Cu phase and the crystal structure analysis remains controversial. Based on the morphological characteristics, our Al_2Cu particles are different from the θ' and Ω phase. Thus, convergent beam electron diffraction (CBED) analysis and atom probe study were carried out on the globular Al_2Cu phase in order to identify its crystal structure and composition. The BF TEM

image on the tip shape of specimen is shown in Fig. 6.13. From the Fig. 6.13(c), there is 4 fold symmetry but not the cubic structure due to slightly different d spacing with {011} plane. Thus this phase may be tetragonal structure. The lattice parameter of this phase very close to that of equilibrium phase of Al_2Cu (θ phase) which has body centered tetragonal structure.

Si-modified Al_2CuMg phase in the T7 aging condition was also observed. However, there is not much of this particle like equilibrium θ phase. Interestingly, this S type Al_2CuMg phase still contain the same amount of Si as much as Cu and Mg in the precipitate. We represent the 3DAP result and compositional profile on the equilibrium θ and Si modified Al_2CuMg in Fig. 6.14 and 6.15, respectively. There is no evidence of Si effect on the equilibrium θ, while there is 20 at% of Si in Si- modified Al_2CuMg phase. We are still under way of the crystal structure of this Si modified Al_2CuMg.

Fig. 6.13 Transmission electron micrograph, in <001> Al matrix showing the presence of θ' phase and Al_2Cu. (a) BF TEM image and corresponding SAD pattern (b), and dark field images obtained using the streaks marked by A which d spacing corresponding to 4.2Å.

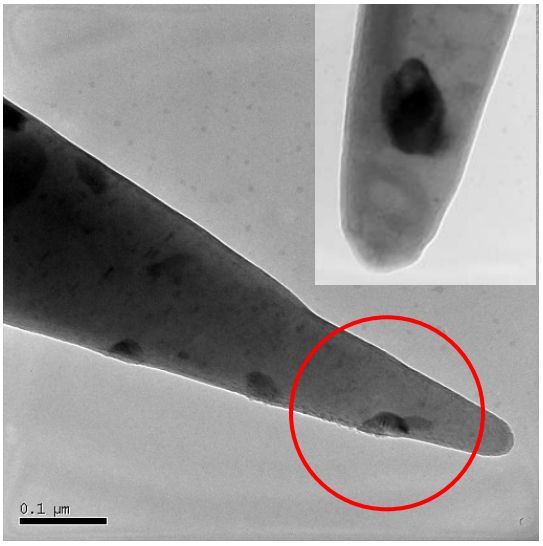

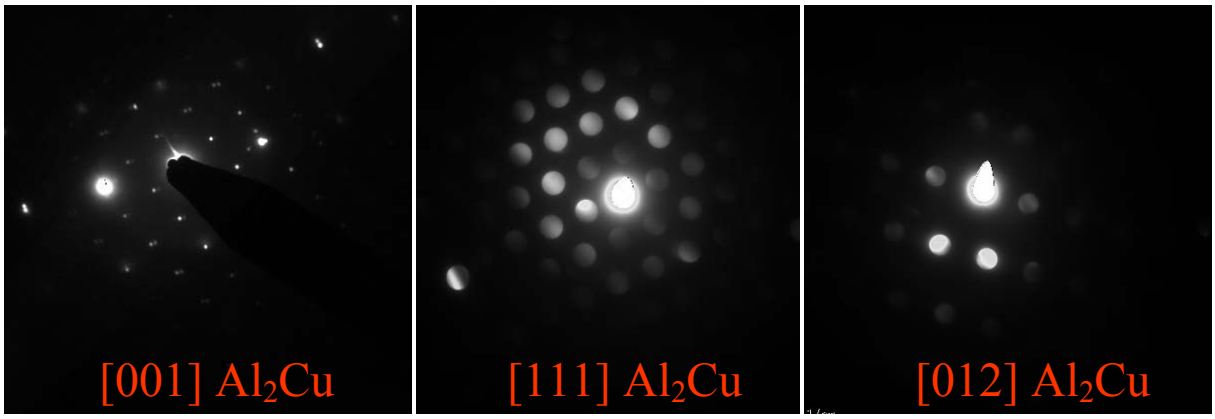

Fig. 6.14 3 dimensional reconstruction of Al_2Cu precipitates in the modified Al-Si-Cu-Mg alloy and its compositional profile.

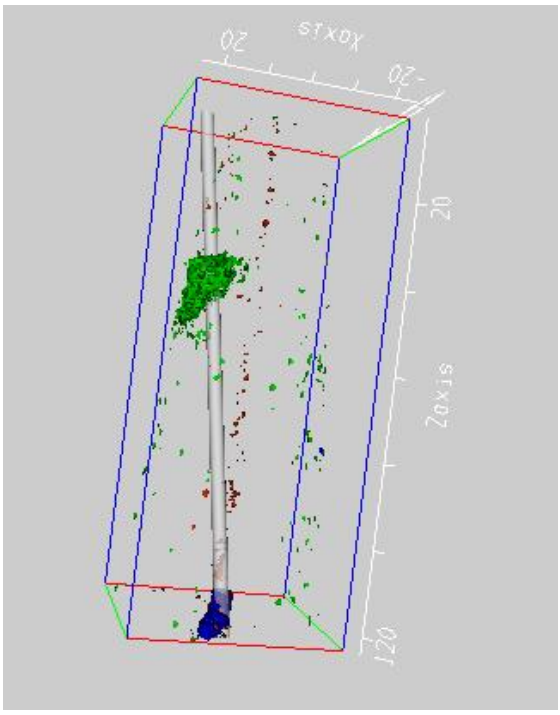

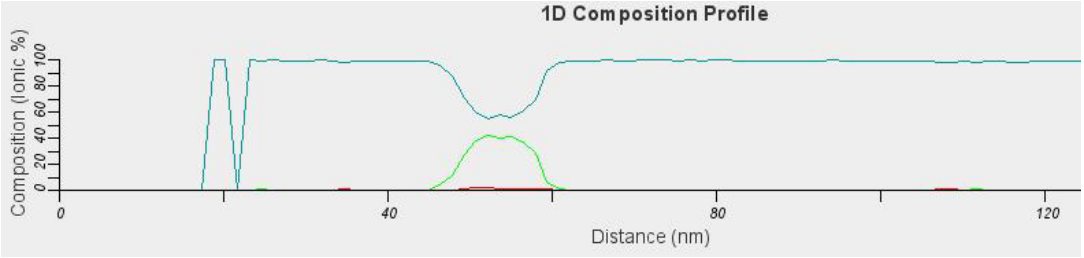

Fig. 6.15 3 dimensional reconstruction of Si modified Al_2CuMg precipitate in the modified Al-Si-Cu-Mg alloy and its compositional profile.

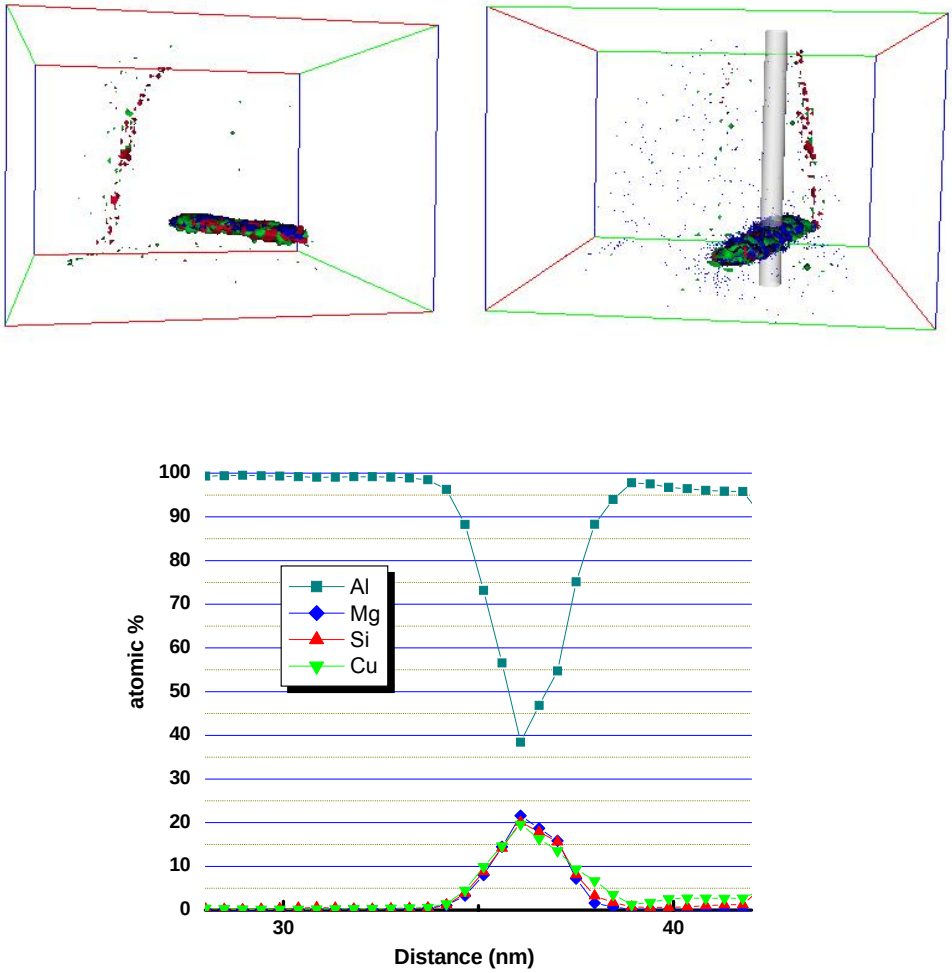

6.4 Reference

[1] D.G. Eskin, J. Mater. Sci. 38(2003)279

[2] C.R. Hutchinson and S.P. Ringer, Metall. Mater. Trans. 31A(2000)2721.

[3] K. Raviprasad, C.R. Hutchinson, T. Sakurai, S.P. Ringer, Acta Mater.51(2003)5037

[4] S. Hirosawa, T. Sato, A. Kamio, H.M. Flower, Acta Mater. 48(2000)1797

[5] J.Y. Hwang, H.W. Doty, M.J. Kaufman. TMS letters, 3(2006)39

[6] G.B. Brook, “Precipitation in Metals”, Special reports No.3, Fulmer Research Institute, UK,1963.

[7] A.M.Zahra, C.Y. Zahra, C. Alfonso, A. Charai, Scripta Mater. 39(1998)1553.

[8] S.P. Ringer, S.K. Caraher, I.J. Polmear, Scripta Mater. 39(1998)1559.

[9] A. Charai, T. Walther, C. Alfonso, A.M. Zahra, C.Y. Zahra, Acta Mater. 48(2000)2751.

[10] L. Kovarik, M.K. Miller, S.A. Court, M.J. Mills, Acta Mater. 54(2006)1731.

[11] K. Hono, N. Sano, S.S. Babu, R. Okano, T. Sakurai, Acta Metall. Mater. 41(1993)829

[12] B.C. Muddle, I.J. Polmear, Acta Metall. 37(1989)777

[13] A. Garg, J.M. Howe, Acta metal., 39(1991)1939

[14] M. Murayama, K. Hono, Scripta Mater. 38(1998)1315

[15] A.M. Zahra, C.Y. Zahra, K. Raviprasad, I.J. Polmear, Phil. Mag. 84(2004)2521

[16] S.P. Ringer, K. Hono, I.J. Polmear, T. Sakurai, Acta Mater. 44(1996)1883

[17] B.T. Sofyan, K. Raviprasad, S.P. Ringer, Micron, 32(2001)851

[18] A.K. Mukhopadhyay, Metall. Mater. Trans. 33A(2002)3635.

[19] I.C. Barlow, W. M. Rainforth, H. Jones, J. Mater. Sci, 35(2000)1413.

[20] L. Kovarik, P.I. Gouma, C. Kisielowski, S.A. Court, M.J. Mills, Acta Mater. 52(2004)2509.

[21] P. Ratchev, B. Verlinden, P. De Smet, P. Van Houtte, Acta Mater. 46(1998)3523

[22] L. Kovarik, P.I. Gouma, C. Kisielowski, S.A. Court, M.J. Mills, Mater. Sci. Eng. A. 387-389(2004)326.

[23] J.M. Silcock, J. Inst. Met. 89(1960-1961)203.

[24] S. Kerry, V.D. Scott, Metals Sci. 18(1984)289.

CHAPTER 7

HIGH RESOLUTION TEM STUDY OF HETEROGENEOUSLY NUCLEATED θ' PHASE IN THE Al-Si-Cu-Mg ALLOYS

7.1 Introduction

Precipitation strengthening mechanisms and precipitation kinetics have become the subject of much research since the discovery of Guinier-Preston (GP) zones [1-2]. In the case of Al-Cu alloys, the examination of GP zones, metastable θ' phase, and stable θ phase are important not only during the nucleation process but also for understanding useful strengthening mechanisms [3-6]. Among the many commercial engineering aluminum alloys, the quaternary Al-Si-Cu-Mg systems have been attractive recently because of their high strengthen and ductility as well as their enhanced thermal stability [7-8]. The precipitation sequence in these quaternary alloys is rather complex and involves several different metastable and/or stable phases as dominant hardening phases [9-10]. Thus, understanding the nucleation mechanisms and kinetic responses are important subjects for optimizing alloy design and process development in this system.

As shown in Chapter 6, the θ' phase and the Si-modified GPB zones (Guinier-Preston-Bagaryatskii) are dominant the hardening phases in these quaternary alloys. Based on the general nucleation theory, GP or GPB zones should develop homogeneously from the early stages of the aging process, while the θ' phase may develop preferentially on heterogeneous nucleation sites such as dislocations or other precipitates [11]. In addition, there are also some reports on the continuous transformation of GP(1) zones into GP(2) zones into the θ' phase with increasing the

thickness [5, 12-13]. To date, there have been few reports of the heterogeneous nucleation of θ' precipitates from the precursor GP zones or other types of precipitates. The difficulty of direct observation of such effects is due to the extremely small size of the precursor and product phases or the inability to detect this reaction.

The recent development of three-dimensional atom probe tomography combined with high-resolution transmission electron microscopy allows for the observation of atomic-scale nucleation. In this study, the heterogeneous nucleation of two different morphologies of θ' phases, plate shape and lath shape, from two different heterogeneous nucleation sites were found the metastable precursor of Si modified GPB zone and Mn containing particles. Based on the results, nucleation mechanism of θ' precipitate is discussed.

7.2 Experimental Procedure

The alloy used in this experiment is Al-1.1Si-2.0Cu-0.5Mg-0.5Fe-0.6Mn. A T7 averaging treatment was performed on this sample after solution heat treatment at 488°C for 8h. A more detailed heat treatment procedure was described in the chapter 4. High-resolution transmission electron microscopy combined with three-dimensional atom probe tomography were used to investigate the heterogeneous nucleation of the θ' phase in this alloy. The sample preparation procedure and analysis conditions are described in the appendix 1. For the direct observation with Z-contrast generated by high angle annular dark filed (HAADF) scanning transmission electron microscopy (STEM), FEI TECNAI F20 equipped with a Gatan energy dispersive X-ray spectroscopy (EDS) was used.

7.3 Results and Discussion

In Chapter 6, it was shown that the θ' and Si-modified GPB zones were the dominant hardening phases in this particular alloy. The typical morphology of the θ' phase was shown to be plate-like with dimensions of 3-5nm thickness and 80~120nm length and width. The composition of the θ' was also determined to be close to Al_2Cu. However, abnormally-thick θ' particles (marked A and B in Fig.7.1), were observed occasionally. EDS analysis (Fig.7.2) revealed that these particles appear to contain only Al and Cu. From this result, it is assumed that these particles are not S type (Al_2CuMg), β type (Mg_2Si), Q type ($Al_4Cu_2Mg_8Si_7$), or some other type of precipitates containing Mg and Si [9]. While these two precipitates are aligned along the $<100>_{Al}$ cube directions like the typical θ' phase, they have somewhat different morphological features. Specifically, it was found during tilting in the TEM that these two particles appear to have slightly different contrast and brightness in the HAADF-STEM images. Based on observations at different tilts, the precipitate marked by A appears to have a lath-like morphology, while the precipitate marked B appears to have a plate-like morphology. Three-dimensional atom probe analysis (Fig.7.3) of this material also revealed supporting evidence for the existence of two different morphologies of the Cu-containing precipitates. One-dimensional composition profiles through these different precipitates (Fig.7.4) indicate that these two particles have a 2:1 Al:Cu ratio. It is very interesting to find a lath-like Al_2Cu precipitate with an orientation relationship with the matrix.

Fig.7.1 HAADF-STEM micrograph showing the 2 abnormally thick Al_2Cu phases marked by A and B. The circled areas represent the heterogeneous nucleation sites for these two particles. White arrows point to typical dominant hardening θ' phase in this alloy.

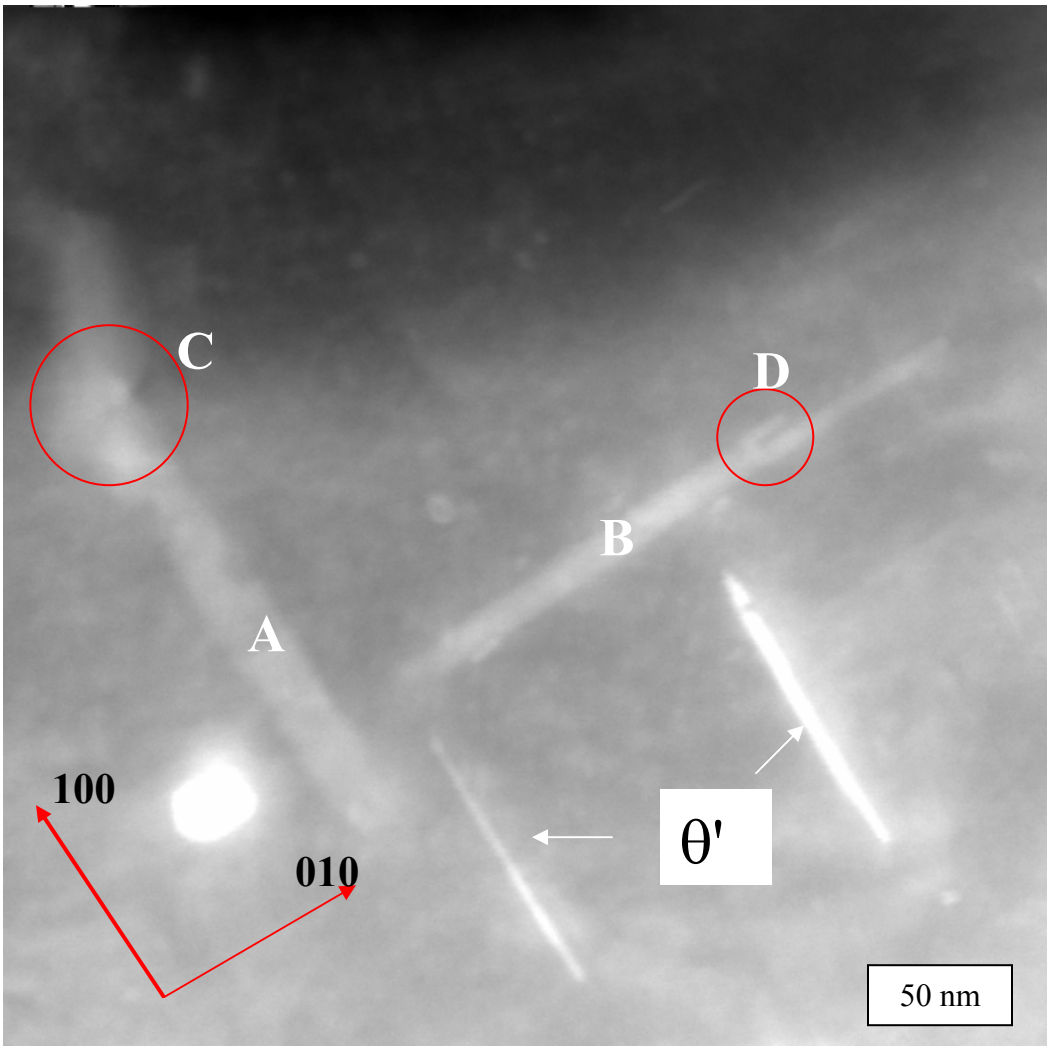

Fig.7.2 EDX spectra obtained from precipitates marked A, B, C, and D. The results show that these particles composed of mainly Al and Cu, while circle C area contains Mn and Si, and circle D contains small amount of Si and Mg with Cu.

(a)

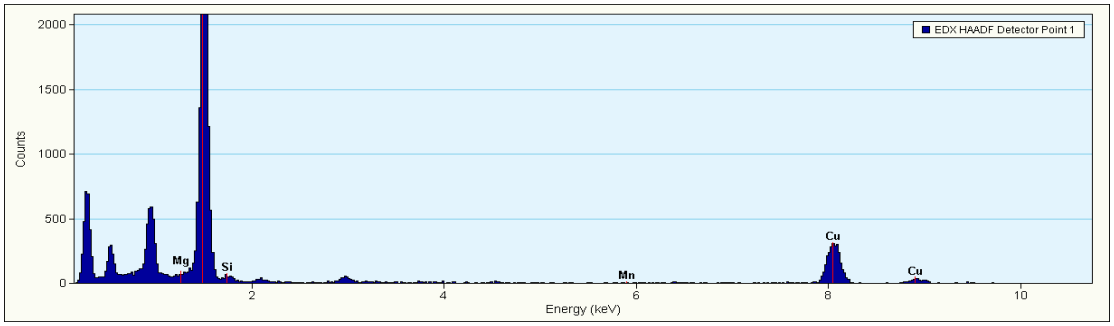

(b)

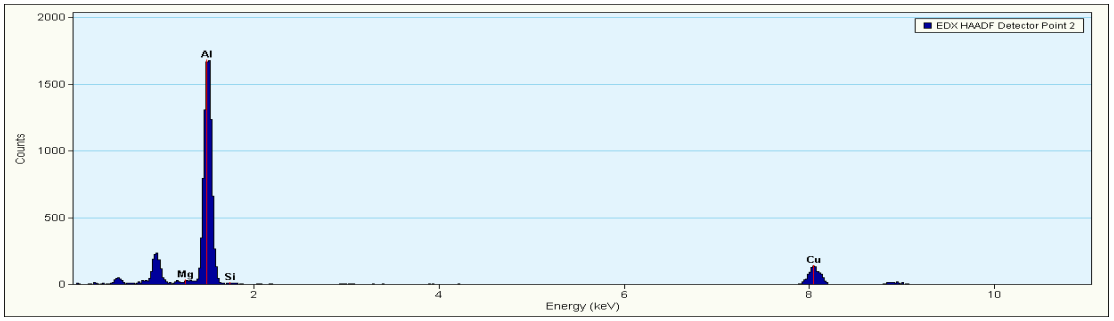

(c)

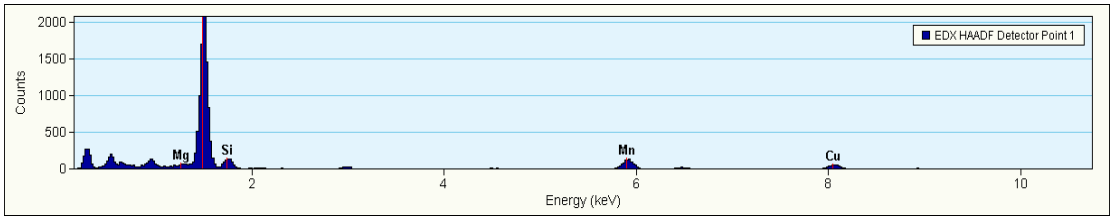

(d)

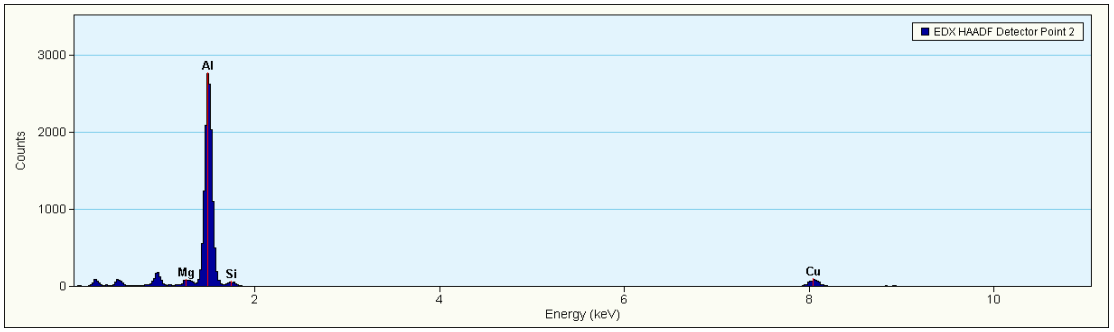

Fig.7.3 3D atom probe results show the existence of lath shape Al_2Cu precipitates. The cylinders in (c) and (d) were used to generate the 1 dimensional compositional profile in Fig. 4.

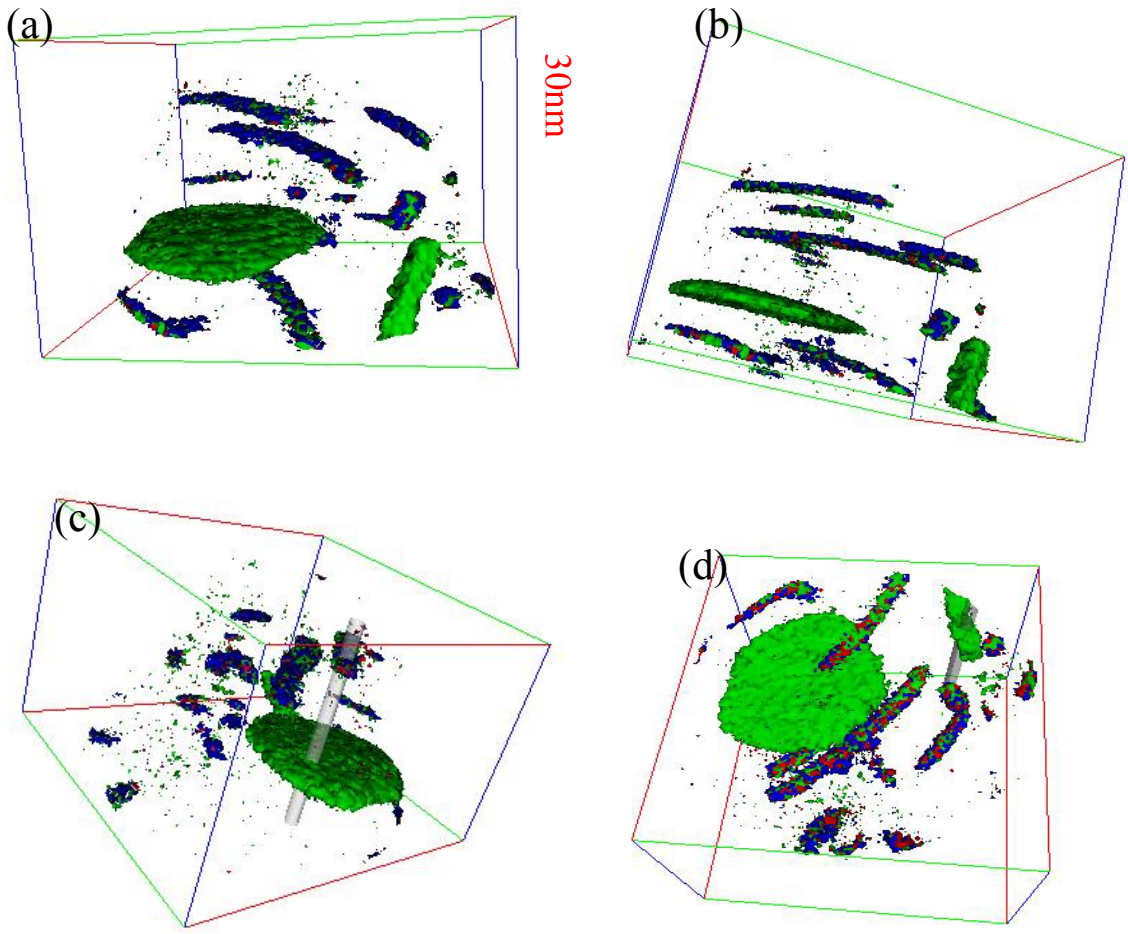

Fig.7.4 The 1 D compositional profiles from Fig.7.3 (c) and (d).

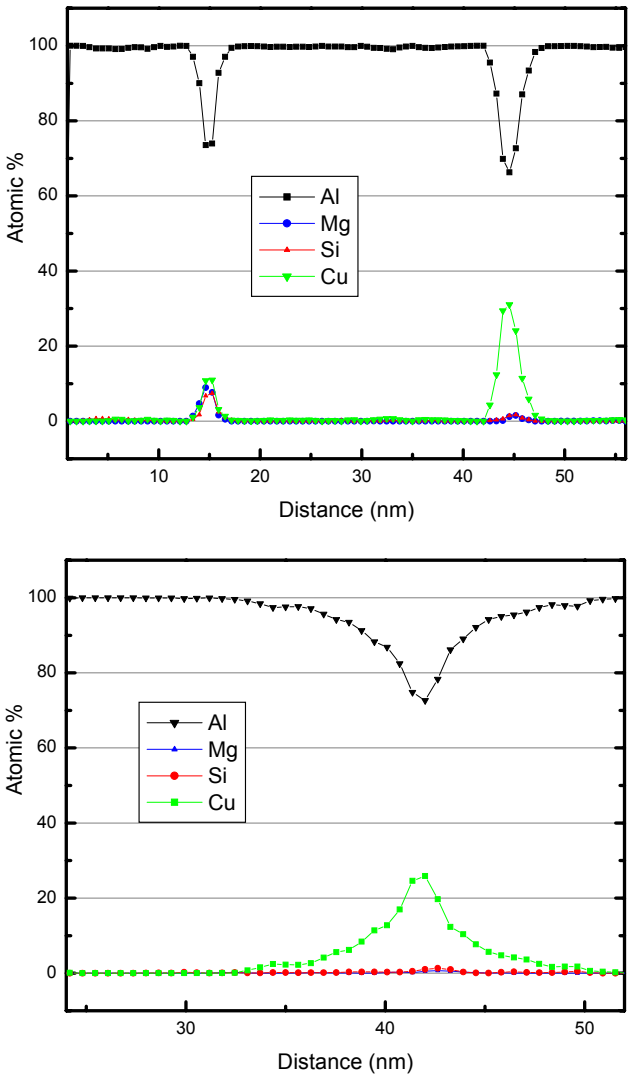

Generally, two variations of Al_2Cu are known as important hardening phases in this system [14]. One is the common θ' phase lying along the $\{100\}_{Al}$ planes and the other is the Ω phase which are also plates that lie along the $\{111\}_{Al}$ planes. They have different habit planes, nucleation mechanisms, and crystal structures, but morphologically they are similar.

A more detailed crystallographic study was performed on a lath type Al_2Cu precipitates. The circle at the end of the lath-type precipitate in Fig.7.1 shows a Mn-containing particle. Interestingly, it is common to find Mn-containing particles at the ends of these lath-type Al_2Cu precipitates. As shown in Chapter 6, two different morphologies, globular and rectangular, of the α-Al[Si,Mn]Cu phase are present in these alloys. The BF TEM image and microdiffraction pattern in Fig.7.5 confirm that this globular phase is α-Al[Si,Mn]Cu. Microdiffraction patterns from the lath-type Al_2Cu phase that nucleated on the globular α-Al[Si,Mn]Cu particle (Fig.7.6) indicate that these laths have the same lattice parameters as the tetragonal θ' phase (a = 0.4nm, c = 0.58nm). The HRTEM micrograph and FFT obtained from a lath type θ' precipitate (Fig.7.7) reveals that this particle has a different orientation relationship with the Al matrix as compared to the typical plate-like θ' phase. The sharp spot near the 020_{Al} corresponds to $011_{\theta'}$, and the spot lying on the forbidden 210_{Al} corresponds to $103_{\theta'}$. These data suggest that the orientation relationship between the lath-type θ' and the Al matrix is $<311>_{\theta'}//<001>_{Al}$ and $\{011\}_{\theta'}//\{010\}_{Al}$. This is different from the typical orientation relationship of plate-like θ' precipitates with a $\{001\}_{Al}$ habit planes which is $<100>_{\theta'}//<100>_{Al}$ and $\{011\}_{\theta'}//\{001\}_{Al}$. It is believed that the lath shape θ' precipitates nucleate heterogeneously at the edge of the α iron particles and grow and thicken losing

Fig.7.5 BFTEM micrograph and corresponding microdiffraction pattern (indexed as a <013> zone axis from α-Al[Si,Mn]Cu) of a region containing the globular phase nucleating two different Al_2Cu laths.

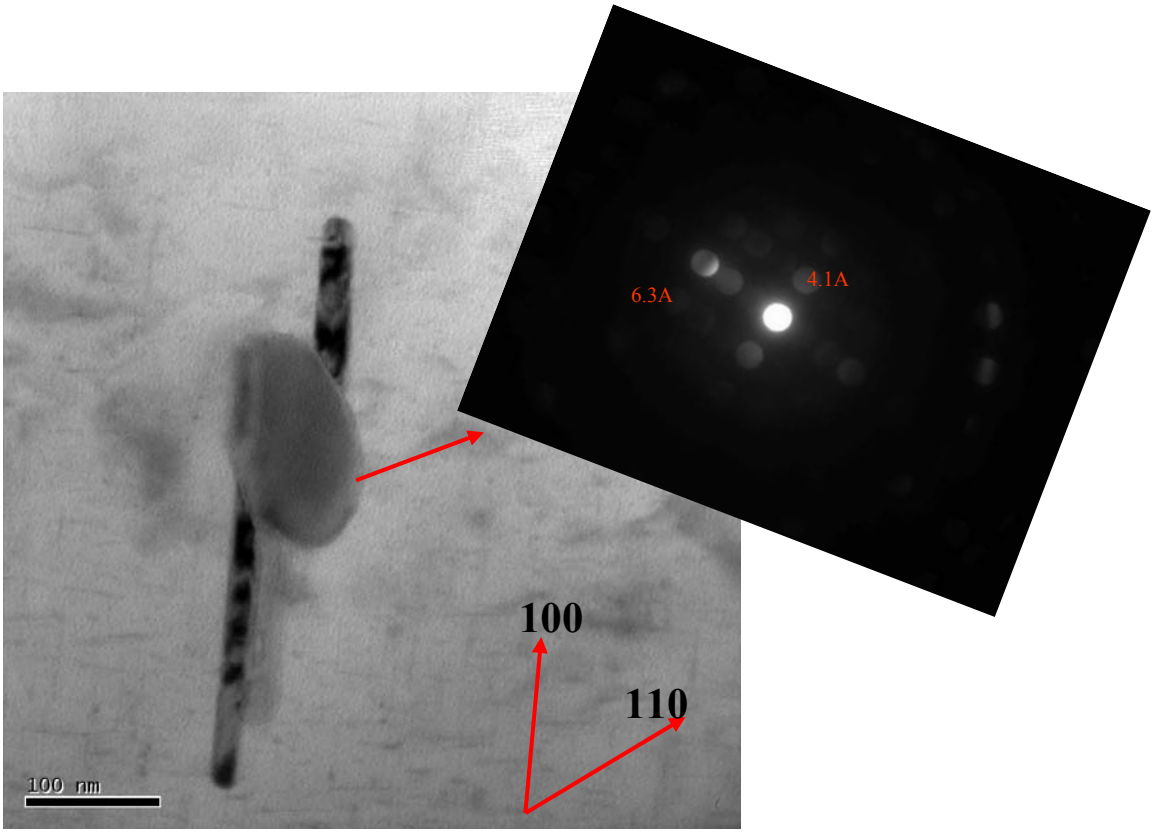

Fig.7.6 Microdiffration patterns from the lath types of θ' precipitate.

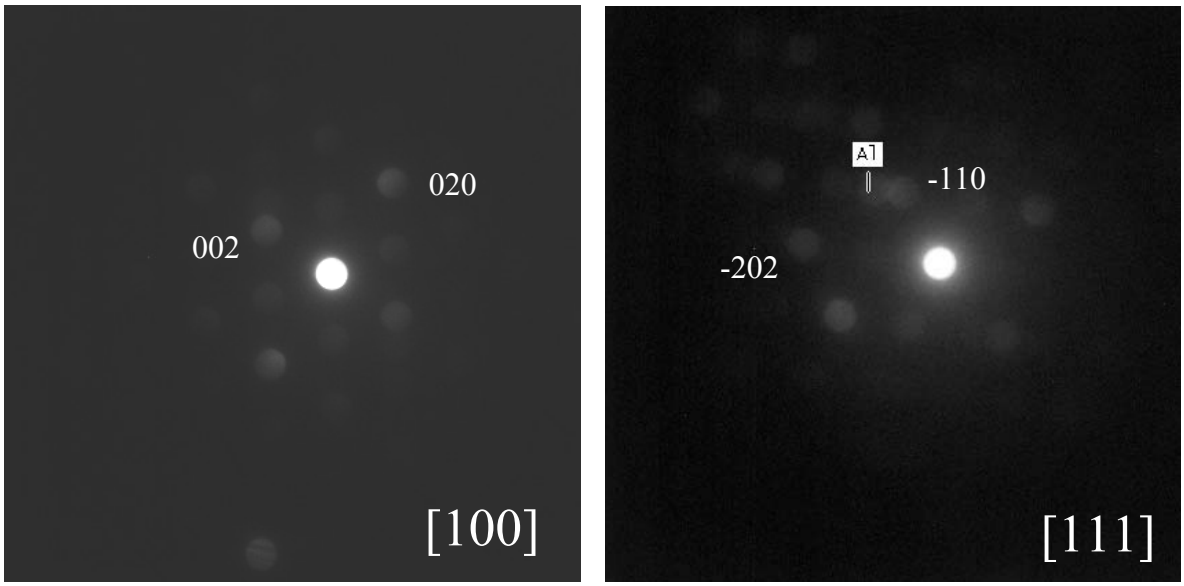

Fig.7.7 HRTEM from lath type precipitate.

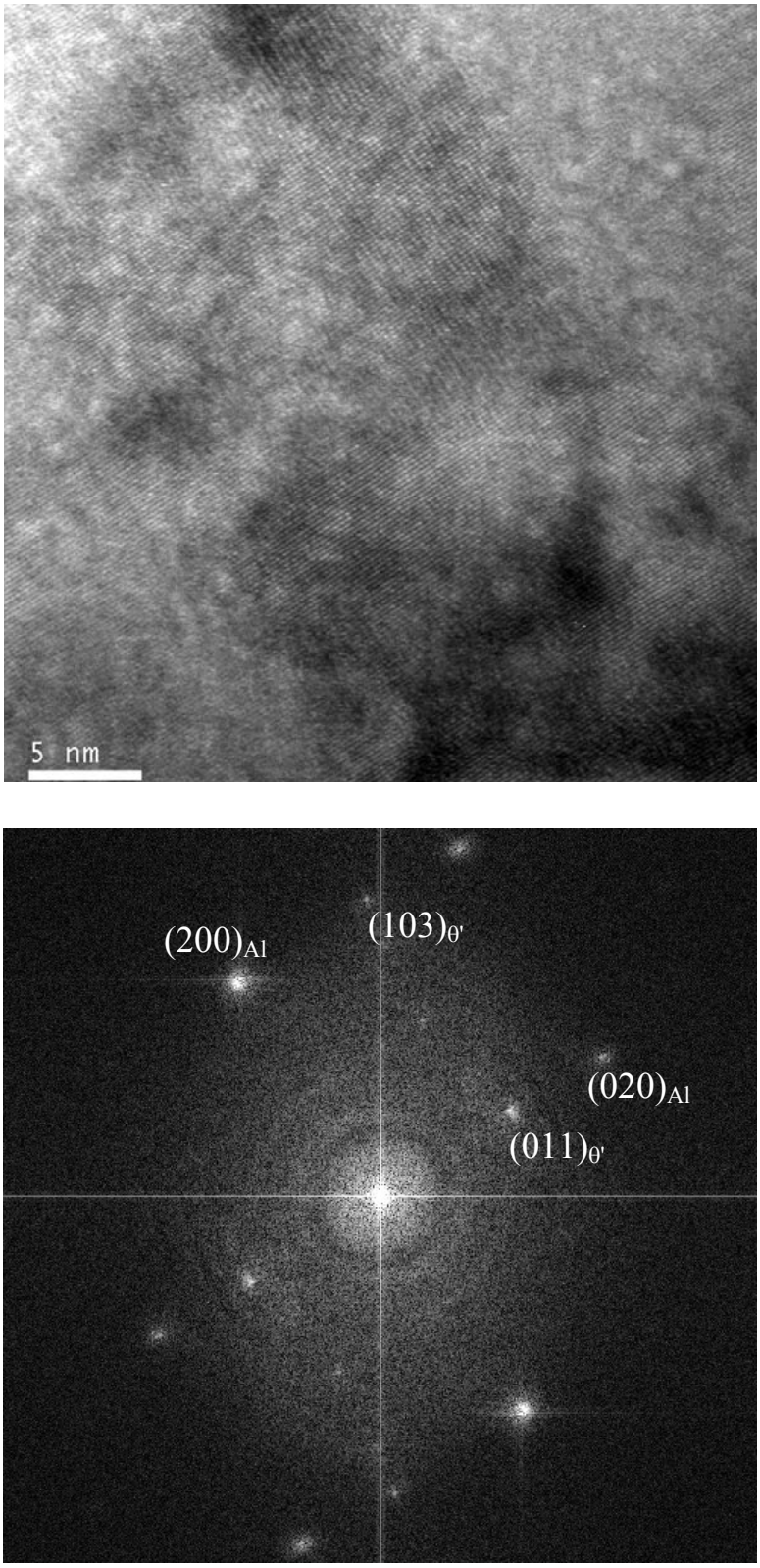

their coherency with the matrix. Thus, is appears that, for heterogeneous nucleation of θ' from the globular a precipitates, it is not necessary to satisfy the conventional orientation relationship. There are some interesting reports on the effects of Mn-containing dispersoids, *i.e.*, the $Al_{20}Cu_2Mn_3$ phase, which act as heterogeneous nucleation sites for the hexagonal plate shaped Ω phase (Al_2Cu) [15-16] and the cuboidal σ phase ($Al_5Cu_6Mg_2$) [16]. These reports suggested that these Mn-containing particles are predominant nucleation sites for the Ω phase which is a major hardening phase in these systems. However, the number density of the α-Al[Si,Mn]Cu particles is very small in our system, thus it is hard to observe the lath-type θ' phase. Further, there is a small amount of Mn in the primary α aluminum phase, because the Mn partitions with iron to the interdendritic regions during solidification. The solubility of manganese and iron in this system is very low; thus, the manganese is not likely to play a dominant role in the heterogeneous nucleation of the θ' phase.

Heterogeneous nucleation of θ' on the Si-modified GPB zones was also examined. Fig.7.8 represents three dimensional atom probe results showing the plate shape θ' precipitates nucleated on the rod type GPB precipitates. Both the Si-modified GPB zone and the plate-shaped θ' precipitates are aligned along the same $<001>_{Al}$ direction in the Al matrix as pointed out in Chapter 4. The growth of the plate-shaped θ' precipitate on the heterogeneous nucleation site is likely to follow the general growth mechanism [11] The θ' particle nucleated along the elongated side of the GPB zone and grew in the elastically-soft <100> direction in the aluminum matrix. The HRTEM micrograph (Fig.7.9a) taken from the circled area indicated by mark D in Fig.7.1 shows that one Si modified GPB zone served as two θ' nucleation sites. The FFT spectra

(Fig.7.9b) representing the combined θ' and Si modified GPB zone show very complex results. The spots in the FFT spectra corresponding to the Si modified GPB zone are unclear, but the view of the spherical end of the Si modified GPB zone is clearly visible in the HRTEM image. It is likely that the complexity of the FFT spectra in Fig.7.9 (b) is associated with the combination of two θ' phases nucleated on one Si-modified GPB zone. The spectrum corresponding to $(002)_{\theta'}$ is caused by the relatively thin θ' phase (right side of circle D in Fig.7.1), while the $(112)_{\theta'}$ spectrum is caused by the thicker area on the left side of circle D. As we described earlier in this chapter, abnormally thick θ' phase may not follow the typical orientation relationship with the matrix.

Gao et al., reported that fine-scale, lath-type precipitates enhanced the number density of θ' precipitates in the Al-4Cu-0.3Mg-0.5Si alloy [17]. They proposed that these lath particles are Q type precipitates, and regarded them as the dominant heterogeneous nucleation site for θ' precipitates. Hirosawa, et al. [18] reported a Si microalloying effect on the increase in number density of Mg/Cu/vacancy complexes resulting in finer and denser rod-type GPB zones [18]. However, their zones did not contain Si. Instead these GPB zones stimulated intragranular precipitation of hardening Ω phase. However, in the present alloy, Si-modified GPB zones were observed not only to serve as heterogeneous nucleation sites for the θ' phase, but also to act as a dominant hardening phase even for high aging temperatures. The association of Mg-Cu clusters with Si during the early stages of precipitation, i.e., the Si-modified GPB zones, serves to preferentially nucleate θ' phase instead of the Ω phase. However, the presence of two apparently different types of heterogeneous nucleation needs to be resolved. as understanding and controlling it may allow an increase in the density of the

θ' phase and significantly enhance the mechanical properties of quaternary Al-Si-Cu-Mg alloys as compared to the Si free Al-Cu-Mg alloys.

In this chapter, two different types of θ' particles were introduced. These appear to nucleate heterogeneously and grow in a manner not previously reported. The morphologies of these θ' precipitates are definitely influenced by the nature of their nucleation sites.

Fig.7.8 3D atom probe results showing the plate shape of θ' precipitate that heterogeneously nucleated on the Si modified GPB zone. The cluster of Mg and Si are represented in blue and red sphere in (c). (d) represents the 1 dimensional chemical compositional profile results along the gray cylindrical tube having a 2nm diameter .

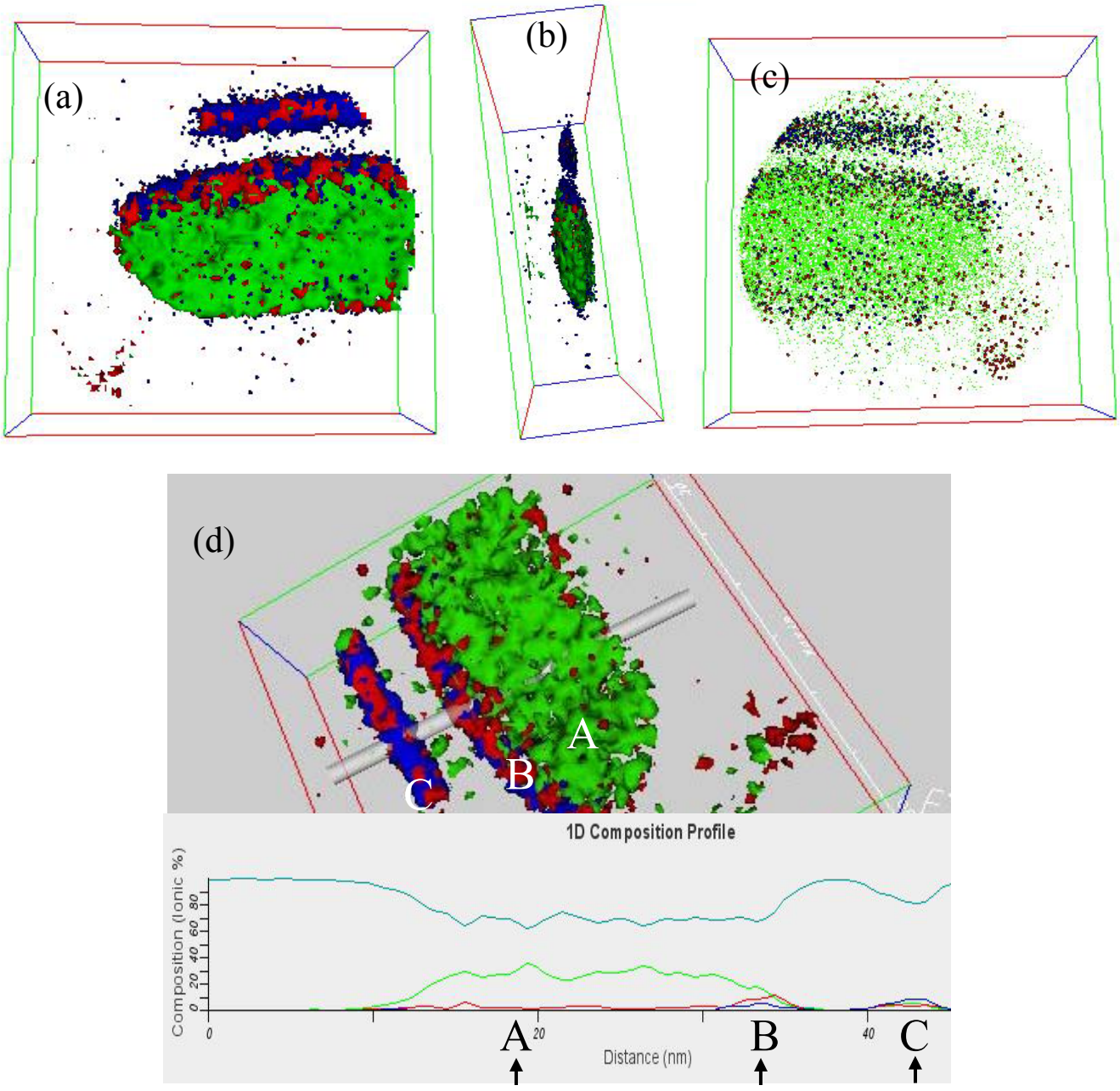

Fig.7.9 HRTEM (a) and FFT (b) showing heterogeneous nucleation of θ' precipitate from the Si modified GPB zone taken from the circle marked D in Fig.7.1.

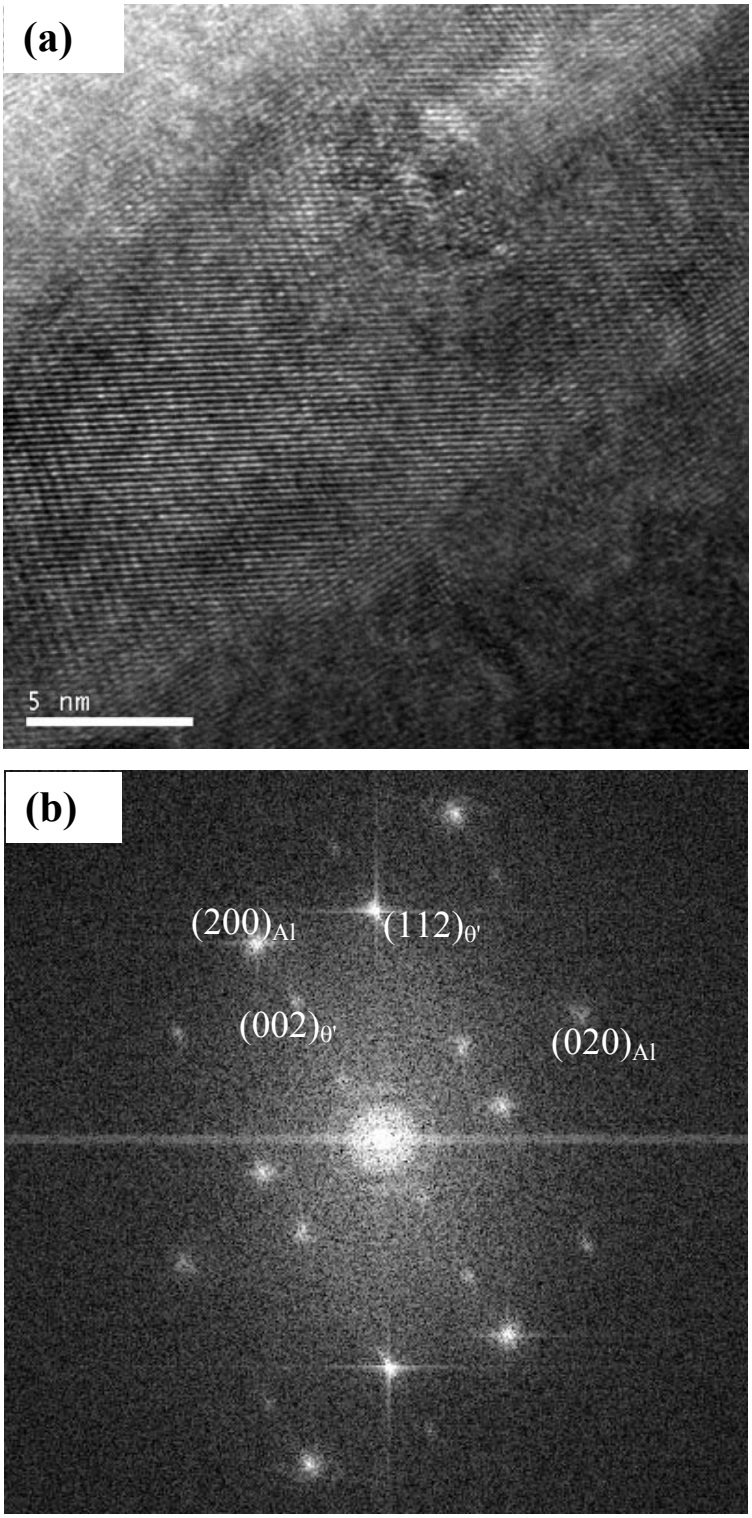

7.4 Reference

[1]. A. Guinier, Nature, 142(1938)569

[2] G.P. Preston, Nature, 142(1938)570

[3] T.J. Konno, M. Kawasaki, K. Hiraga, JEOL News, 36(2001)14

[4] J.M. Silcock, T.J. Heal, H.K. Hardy, J. Inst. Met. 84(1954-55)23

[5] H. Fujita, C. Lu, Mater. Trans. JIM, 33(1992)892

[6] J.W. Martin, Micromechanism in particle-hardened alloys, Cambridge, UK, 1980.

[7] C.R. Hutchinson and S.P. Ringer, Metall. Mater. Trans. 31A(2000)2721.

[8] K. Raviprasad, C.R. Hutchinson, T. Sakurai, S.P. Ringer, Acta Mater.51(2003)5037

[9] D. G. Eskin, J. Mater. Sci. 38(2003)279

[10] J.Y. Hwang, H.W. Doty, M.J. Kaufman. TMS letters, 3(2006)39

[11] D.A. Porter, K.E. Eastering, Phase transformations in metals and alloys, 2 edition, Nelson Thornes Ltd. UK, 2001

[12] T. Sato, T. Takahashi, Trans. JIM, 24(1983)386.

[13] V. Gerold, Scripta Metall. 22(1988)927

[14] K. Hono, N. Sano, S.S. Babu, R. Okano, T. Sakurai, Acta Metall. Mater. 41(1993)829

[15] L.M. Wang, H.M. Flower, T.C. Lindley, Scripta Mater. 41(1999)391.

[16] A. K. Mukhopadhyay, Metall. Mater. Trans. 33A(2002)3635.

[17] X. Gao, J.F. Nie, B.C. Muddle, Mater. Sci. Forum, 217-222(1996)1251.

[18] S. Hirosawa, T. Sato, A. Kamio, H.M. Flower, Acta Mater. 48(2000)1797.

CHAPTER 8

CONCLUSIONS

1. The microstructure and mechanical properties of 319 aluminum casting alloys have been examined as a function of Mn content. It is shown that, as the Mn content is increased up to 0.65 wt. pct. (corresponding to an Mn/Fe ratio of ~1.2) in the baseline alloy (Al-7wt%Si-3.8wt%Cu-0.5wt%Fe), the plate-like β-Al_5FeSi intermetallic phase is completely modified to the Chinese script α-$Al_{13}(Fe,Mn)_4Si_2$ phase resulting in improved tensile properties. Excess amounts of Mn, however, deteriorate the mechanical properties by increasing the total amount of intermetallic phase. The ultimate tensile strength (UTS) values in the T6 samples are in inverse proportion to recess area measured from the fracture surface. The UTS and % Elongation are slight increased, as the amount of Mn contents increase in the T6 heat treated sample, while the yield strength (YS) is less dependent on the Mn variation.

2. The crystal structure of α and β intermetallic particles in aluminum 319 (Al-Si-Cu) system was investigated. The morphology of α phase was Chinese script, while β phase was plate shape. The structure of α phase was cubic with 12.5Å lattice parameter and $Im\bar{3}$ space group. Plate shaped β-phase was orthorhombic with a = 20.8Å, b = 6.2Å, and c = 6.18Å and Cmcm space group. The β phase was a single crystal having planar defects along the (100) plane with identical orthorhombic phase, which formed faulted variants. The Kikuchi lines of the cubic α phase was featured in the double bands due to its distinctive ordered structure.

The structure of the α and β intermetallic phases had no influence by the cooling rate, rather presence of Mn is critical for modification of morphology of iron intermetallic phases.

3. The influence of Mg additions on the microstructure and mechanical properties of Type 319 aluminum alloy (Al-6.5~7wt%Si-3.5~4wt%Cu) has been investigated. As increase the Mg content up to 0.45 wt.%, the strength of the alloy increase by promoting the formation of a very fine precipitate phase.

4. The compositions and morphologies of nanoscale Q' and θ' precipitates in a Mg-modified Type 319 aluminum foundry alloy have been characterized using both three dimensional atom probe tomography and high resolution transmission electron microscopy. It is shown that the Q' precipitates are lath-shaped and enriched in Mg, Cu and Si with a composition almost identical to that in the stable Q ($Al_5Mg_7Cu_2Si_6$) phase present in the as-cast condition. Further, the θ' phase appears as thin plates and is enriched in both Si and Mg in addition to the expected copper enrichment. Finally, the atom probe results suggest a tendency for Si segregation in the matrix although the mechanism for this is unclear at this time.

5. The Si-modified GPB structure are discussed in the low-silicon Al-1.1%Si-3.7%Cu-0.5% Mg alloys. The Si-modified GPB structure have rod type morphology and very fine and uniform distribution along <001> matrix.

6. Two different types of θ' particles were introduced. These appear to heterogeneously nucleate and grow in a manner not previous reported. The morphology of these θ' phase appear to be influenced by the properties of their nucleation sites.

APPENDIX A

FIB SAMPLE PREPARATION FOR ATOM PROBE TOMOGRAPHY AND TRANSMISSION ELECTRON MICROSCOPY, AND ANALYSIS CONDITIONS OF Al-Si-Cu-Mg ALLOY FOR THE 3DAP RECONSTRUCTION

Three dimensional atom probe (3DAP) tomography is an extremely powerful technique for atomic scale characterization of metals, semiconductors and, most recently, some non-conducting materials [1]. Specifically, 3DAP provides unique and precise details concerning atomic scale clustering and precipitation. The structure, morphology and distribution of the strengthening phases are extremely important to the precipitation hardening of aluminum alloys. Thus, the application of the 3DAP to the aging behavior of these alloys can provide some of this information. In addition, transmission electron microscopy can provide both crystal structure information as well as orientation relationship data between the precipitates and the matrix. Thus, the combination of using both 3DAP and TEM can provide a comprehensive insight into the nature of the precipitation behavior/evolution. However, the typical geometries used for each technique are generally quite different. In addition, the 3DAP technique is a destructive characterization tool.

For normal TEM investigations, typical specimens have a 3mm diameter disk geometry. Atom probe specimens, on the other hand, must be sharp needles having tip radii less than 100nm. Thus, successful examination using both the TEM and 3DAP requires sample geometries suitable for both techniques. Modern focused ion beam (FIB) instruments have good capabilities for sample preparation via milling and nanomanipulation; thus, this technique can be used to create new specimen geometries appropriate for both TEM and atom probe analysis.

In this appendix 1, the procedures used to prepare samples for both TEM and 3DAP tomography using the FIB are described. The analysis conditions and 3DAP

reconstruction results are described and compared with TEM observation to analyze the precipitation behavior in modified 319 Al casting alloys.

A.1 Specimen Preparation

First, the Si microtips supplied by IMAGO and FIB half grids supplied by Ted Pella were prepared to attach the aluminum samples. To sharpen the FIB grid tips, electropolishing was performed with 0.25vol% phosphoric acid in distilled water. The geometry of the Si microtips is presented in Fig. A1(a). After heat treating the Al-Si-Cu-Mg alloys to the T6 condition, a representative matrix dendritic region was selected for milling using the FIB, and then lifted out using the nanomanipulator and attached to Si microtips. One end of the lift out was then attached to the posts by milling off sections around 5μm wide. For TEM and atom probe analyses, the samples are sharpened to less than 100nm radius (Fig.A1(b)). Thus, further thinning of the material was carried out with a 30 KV ion beam. Finally, the sample was cleaned with a 5 KV ion beam to reduce any surface damage on the tips. The final specimens prepared by FIB have ~60nm tip radius (Fig. A1(c)). Using these specimens, the morphologies and crystal structures were examined in the TEM prior to the atom probe experiments. For the latter experiments, the samples must be mounted approximately normal to the local electrode. Thus the grid was sandwiched between two silicon pieces with conductive silver epoxy, E-Solder ™ 3021, adhering the samples on the specimen holder of atom probe. TEM and atom probe examination will provide comprehensive and complementary analysis results.

A.2 Atom Probe Analysis Conditions

During the atom probe examination, there appeared to be an issue concerning aluminum hydride formation inducing the overlapping the mass-to-charge peaks with minor trace elements. In particular aluminum-based alloys have low evaporation fields, which invoke hydride formation severely [2]. Some previous results have shown what appears to be an exaggerated Si concentration [3-4], which is likely to come from the overlap between doubly-charged aluminum hydride $(AlH)^{2+}$ and Si^{2+} peaks corresponding to a mass-to-charge (m/n) ratio of 14 amu. While typical 319 type alloys contain ~7% silicon, the majority is known to reside in the as eutectic silicon. Therefore, only small amounts of silicon will dissolve in the matrix. Slightly exaggerated Si segregation along the vertical axis in the aluminum matrix region was found in this research. It seems to be caused by doubly-charged aluminum hydride. It is interesting because Danoix et al. suggested that no aluminum hydrides were detected in the Si^{2+} peak position [2]. Even though the excess silicon content is below 0.1 at% in our sample, the quantitative analysis of the silicon segregation is affected by the overlap between the $(AlH)^{2+}$ and Si^{2+} peaks. However, in the precipitates of interest, the Si content is as low as 0.1 at%, thus, this will not affect the concentration of Si in the precipitates. In order to prevent hydride formation, higher evaporation rates, up to 1% were used. In order to find the appropriate operating temperature for decreasing the hydrogen content, three different specimen temperatures: 40K, 50K, and 70K were used. At 40K, the sample fractured before sufficient data was produced. This is likely caused by the stress in the platinum attachment area. At 70K, there was an apparent increase in the Si content of the aluminum matrix. This may be caused by doubly-

charged aluminum hydride $(AlH)^{2+}$. Therefore, it appears that 50K is the optimal temperature not only for preventing early fracture, but also for preventing overlap of Al and Si information.

A.3 Reconstruction Analysis

The mass-to-charge (m/n) peaks assigned to Al, Si, Cu, and Mg are shown in Fig.A2. There are three isotopes of doubly-charged Mg^{2+} corresponding to 12, 12.5 and 13 amu with no magnesium hydride formation or singly-charged Mg^{1+}. This is in good agreement with Marquis et al. [3]. There are two aluminum peaks corresponding to doubly-charged Al^{2+} at 13.5 and singly-charged Al^{1+} at 27. Aluminum hydride $(AlH)^{+}$ was assigned at 28 amu, because there is very little possibility of detecting the single charged Si^{+} at 28 amu peak position in this sample. Even though it detects the single charged Si^{+} in specific conditions [4], for our experimental condition there was no evidence of single-charged Si. The only three isotopes of silicon were doubly-charged Si^{2+} were observed at 14, 14.5, and 15. Slightly overlapping between the double charge aluminum hydride $(AlH)^{2+}$ and $Si2^{+}$ was a considerable concern. However, based on the isotopic ratio calculation, only a small increase is detected between the measured isotopic ratio and natural isotopic ratios of the three doubly-charged Si isotopes: $^{28}Si^{2+}$, $^{29}Si^{2+}$, $^{30}Si^{2+}$. This value has an effect on the precipitation hardening behavior in our alloy system. Cu was detected at the single charged isotope positions (63, 65 amu), and copper hydride $(CuH)^{1+}$ at corresponding 64 amu. Mass-to-charge peaks corresponding to doubly-charged Cu^{2+} were not clearly observed in our samples.

A.4 Comparison between TEM and 3DAP Results

The morphological features and chemical analysis results on the same area obtained using the two different techniques, TEM and 3DAP are presented in Fig.A3, and Fig.A4, respectively. From the BF TEM image in Fig. A3(a), there is a big particle at the tip end with weak contrast. The overall compositions detected by EDS in TEM technique show the 94.5 at.% Al, 4at.% Cu, and 0.8at% Mg, and 0.5at% Si. The SAD pattern from the higher contrast particle in Fig. A3(a) was indexed as coming from <111> zone of Al_2Cu-θ phase with an orientation relationship with the Al matrix. Obviously, it is difficult to obtain the precise composition from such small particles because of the probe resolution and beam interaction volume. There is also a limitation in determining the exact morphology in three dimensions. However, the morphology obtained by 3DAP reconstruction via isoconcentration surfaces, which creates equivalent compositional contour lines by dividing the three-dimensional data into equiaxed volumetric segments does show a more exact morphology. We observed a total of 2.1 million atoms with an overall composition of 95.2% Al, 0.6% Si, 3.9% Cu, and 0.3% Mg in this sample. In the reconstructions in Fig.A4, aluminum was excluded in order to improve the visibility of the isoconcentration surfaces of the minor elements. Negligible amounts of minor elements such as Fe, Mn, and Sr were detected using both EDX and atom probe analysis. The solubility of Mn and Fe in the dendritic aluminum is very small, thus it is hard to find Mn or Fe containing precipitates.

Fig. A.1 Specimen preparation procedure using the FIB on the Si microtips.

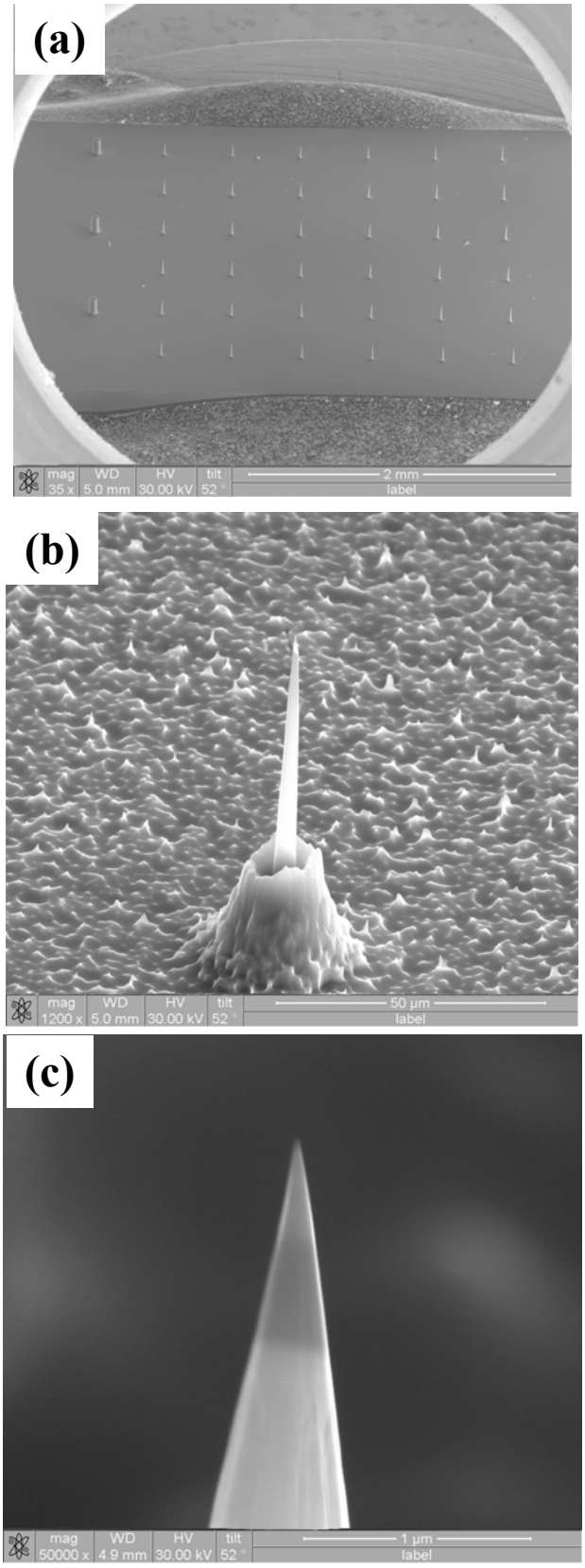

Fig. A.2 Mass to charge spectra from the 3DAP.

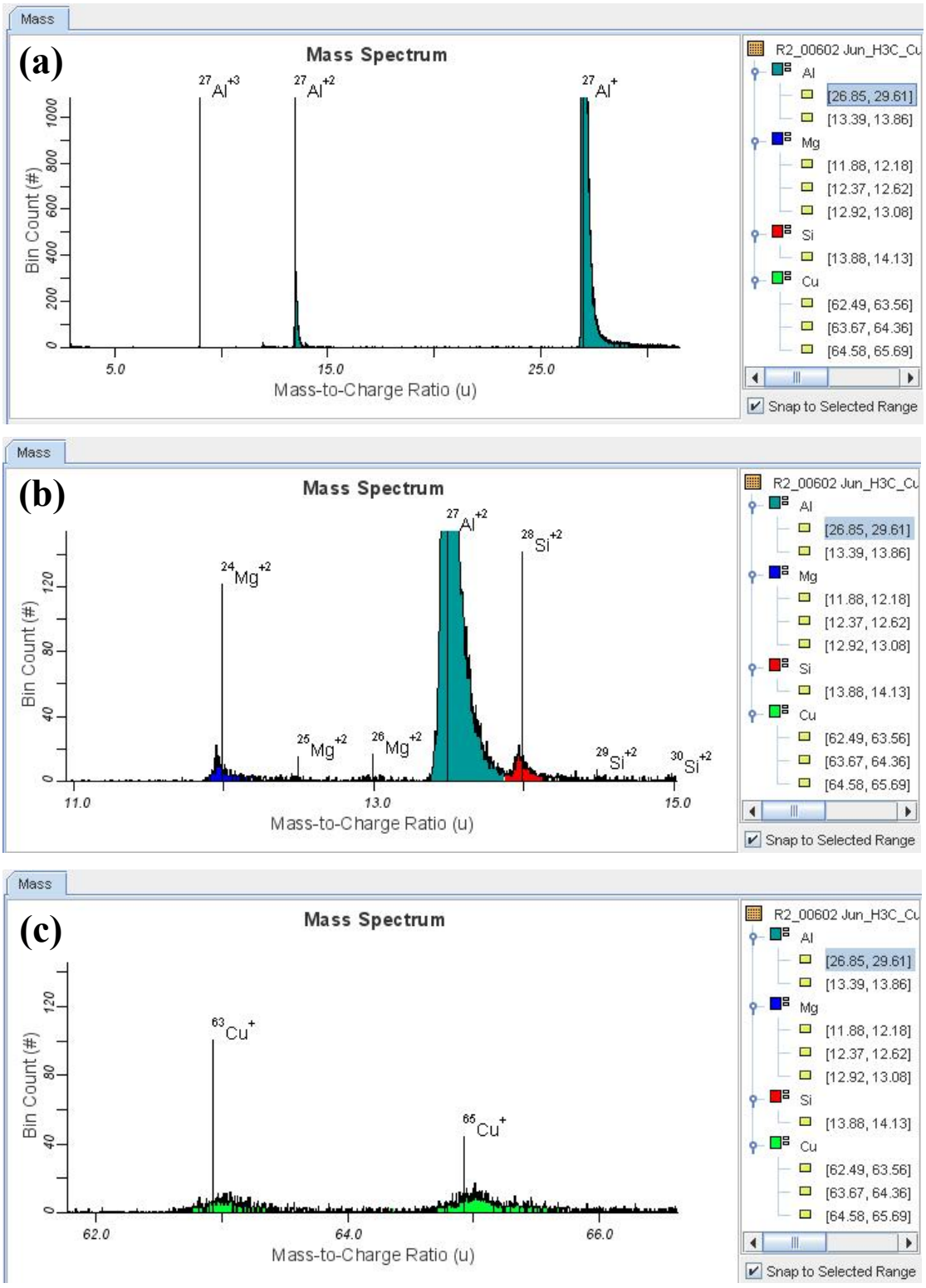

Fig.A.3 TEM bright field micrograph, SAD pattern and EDX spectra obtained from circled area, respectively in (a), (b), and (c).

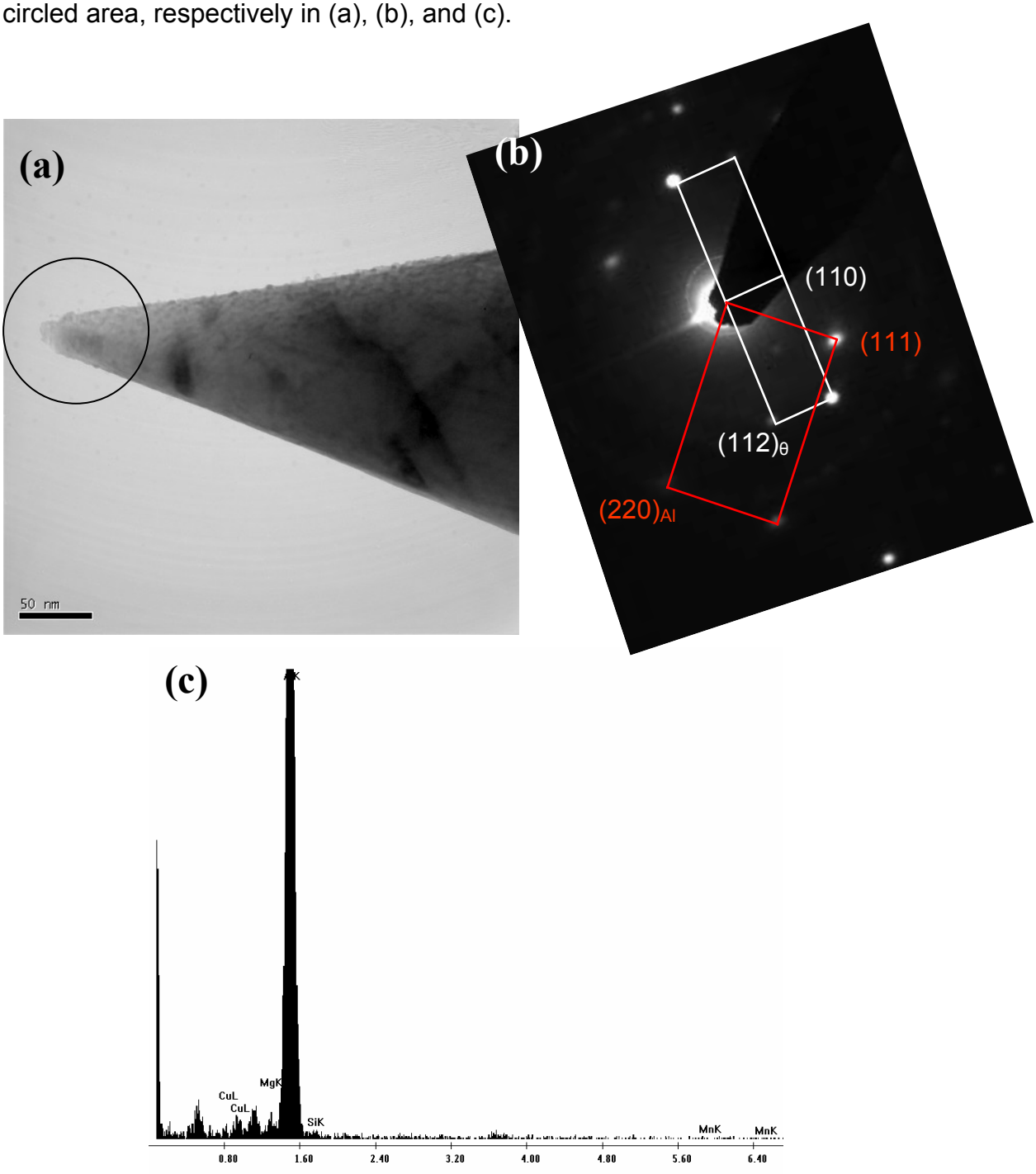

Fig.A.4 Three dimensional atom maps showing the distribution of Si (a), Cu (b), and Mg (c) atoms, and isoconcentration surface images (e) and its compositional profile (f).

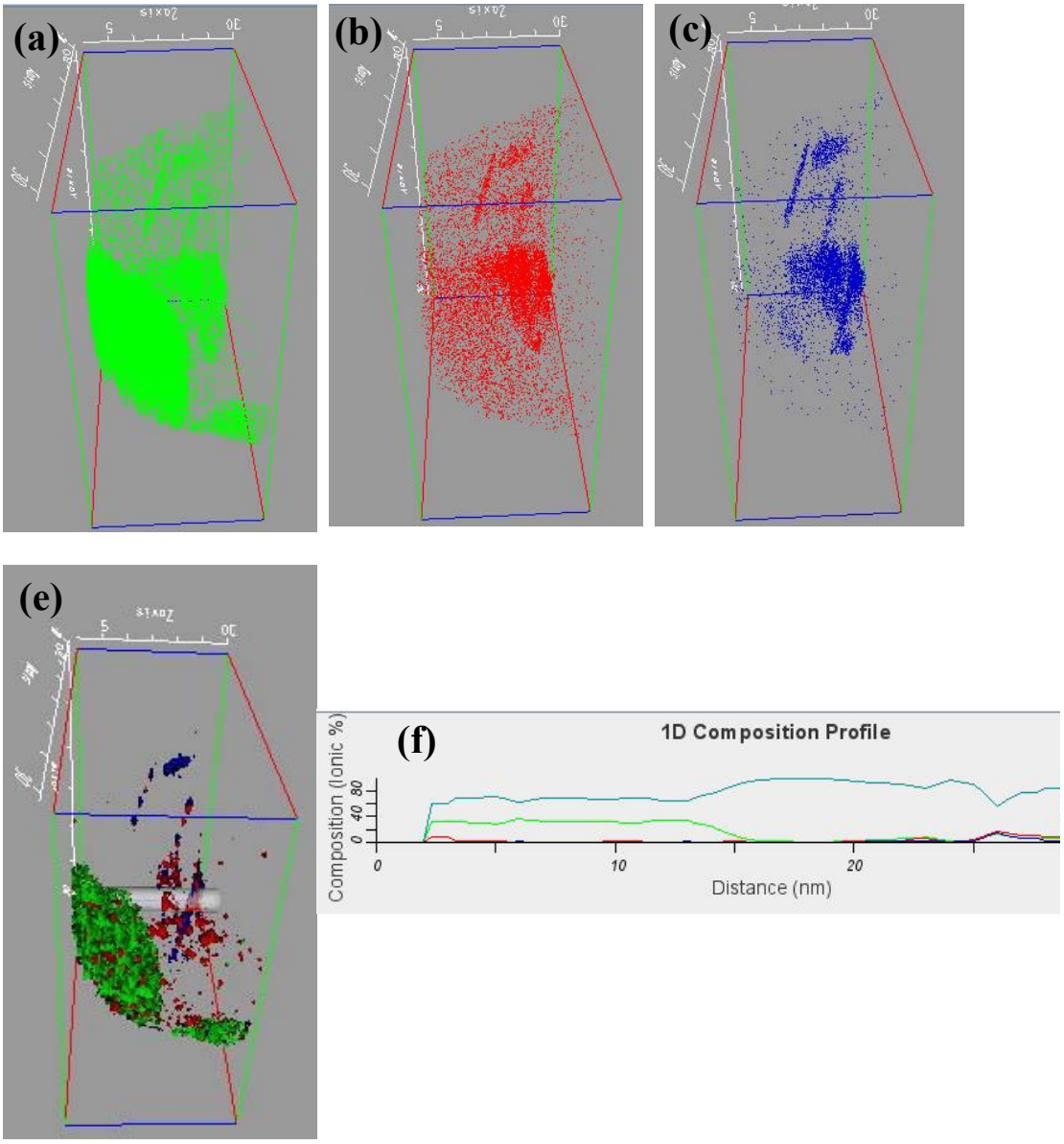

A.5 Reference

1. M.K. Miller, Surf. Interface Anal., 31(2001)593.

2. F. Danoix, M.K. Miller, A. Bigot, Ultramicroscopy, 89(2001)177.

3. E. A. Marquis, D.N. Seidman, M. Asta, C. Woodward, Acta Mater., 54(2006)119

4. Private communication with IMAGO.

APPENDIX B

PRECIPITATION STRENGTHENING MODELS OF MODIFIED 319 TYPE ALUMINUM ALLOYS

Quantification of precipitation hardening remains very challenging despite of a few decades of intensive research on this subject. The characterization of precipitates becomes possible with the aid of advanced characterization techniques such as three dimensional atom probe tomography and transmission electron microscopy. Computed simulation approaches such as first-principle calculations based on density-functional theory are also widely studied. However, many difficulties still need to be overcome in both the practical and theoretical fields.

The main precipitates in the Mg added 319 alloy are proposed as θ' and Q' phases in the previous chapters. Plate-shape of θ' and lath/rod-shaped Q' precipitates form with specific crystalline orientations with the matrix. Therefore, two different precipitates are likely to affect the strengthening in this alloy, which call for consider two different particle hardening models based on the crystal structure and morphological features [1]. However, it is not well understood in the combining effects via two or more multi precipitate hardening mechanism. The method for combining or averaging the two contributable strengthening phases is also unclear. In this study, modified Zhu models [2,3] are first examined to validate to our system, and then proposed model to simulate the strength will be discussed in the modified 319 aluminum system. Finally, new micromechanical models propose by Weakley-Bollin et al., [4] are discussed in our system.

B.1 Strengthening Model by θ’ Phase

For the linear obstacles of random orientations in the slip plane, Zhu developed a model, based on the Orowan equation [5], as a function of precipitate size and volume fraction with unshearable precipitates as follows [2].

$$\Delta\sigma_{ppt} = 0.398\left(\frac{G\mathbf{b}}{\sqrt{Dt}}\right)\left(\sqrt{f} + 0.75 f\sqrt{\frac{D}{t}} + 0.14\frac{D}{t} f^{3/2}\right)\left(\ln\frac{0.87\sqrt{Dt}}{r_o}\right) \quad (1)$$

where D, t, and f are the precipitate diameter, thickness, and volume fraction respectively, as a function of time. r_o is the inner cut-off radius, which is equal to **b** (Burgers vector, 0.286nm). G is the shear modulus (G_{Al} = 25Gpa). The Eq.1 is applicable for plate-like precipitates coherent with specific habit planes in the matrix. Since plate shape particles have large diameter-to-thickness aspect ratios and orientation relation with {001}Al matrix, this model can be applied to the θ' precipitates in Mg added 319 aluminum alloy. The simulated results are depicted in Fig. B1 assuming 4nm thickness and 3.8 vol.% of the θ' particles.

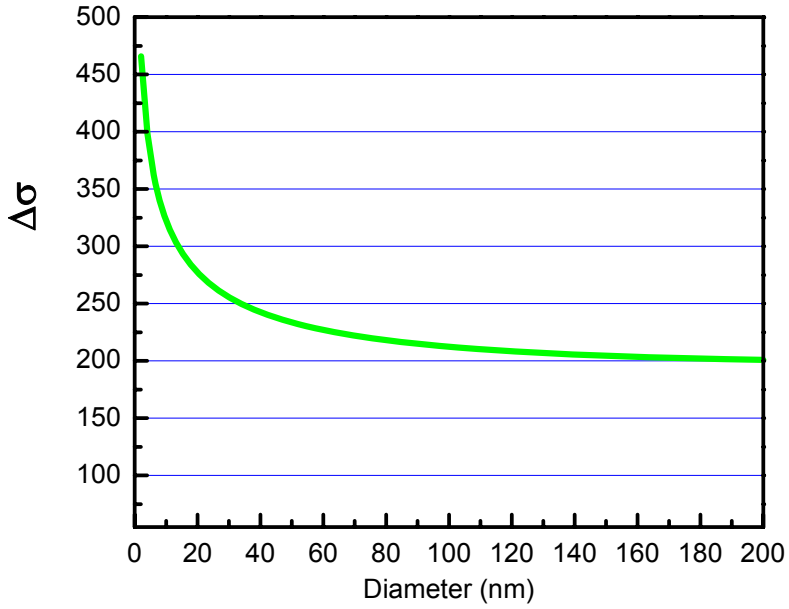

Fig.B.1 Simulated yield strength model strengthened by θ' precipitates based on the equation 1.

B.2 Strengthening Model by Q' Phase

The rod or needle-shape precipitates have been in difficulty for simulating the strengthening mechanism. The reason for this difficulty is their complicated morphology. For the simulation due to rod type precipitates, the Zhu model also can be applied after modification [3]. He also proposed the equation for the rod-shape precipitate by modification of the Orowan equation as follow.

$$\Delta\sigma_{ppt} = 0.459\left(\frac{G\mathbf{b}}{D_r}\right)\left(\sqrt{f} + 1.84\,f + 1.84\,f^{3/2}\right)\left(\ln\frac{1.316\,D_r}{r_o}\right) \qquad (2)$$

where $\boldsymbol{D_r}$ is particle diameter. The Q type precipitates are less understood, not only microstructural evolution, but also the strength hardening mechanism, Therefore, it's necessary to validate above modified Orowan equation with experimental data. We assumed the Q type precipitate as a rod-like precipitate. The simulated results are depicted in Fig. B2 assuming average equivalent circular cross section of radius and 0.038vol.% of the Q' particles.

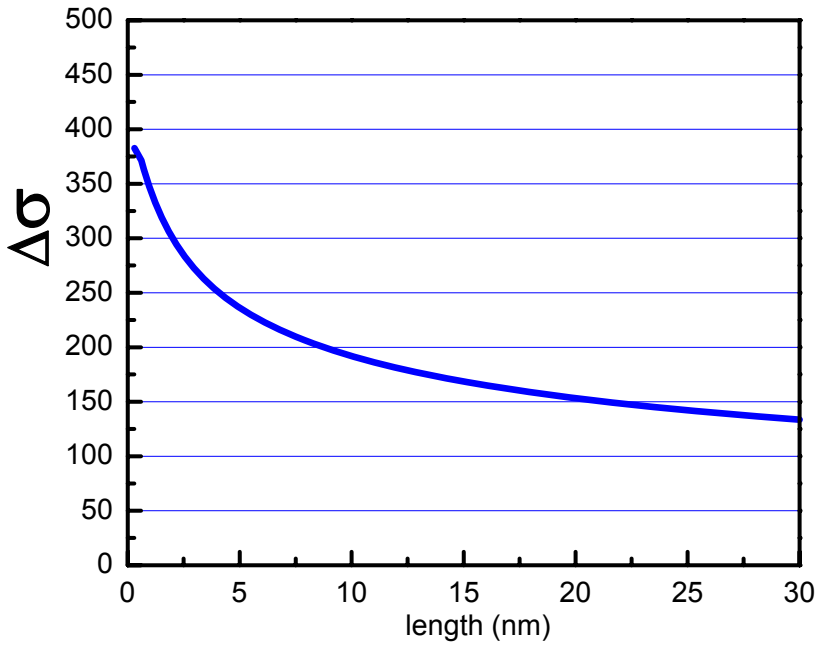

Fig.B. 2 Simulated yield strength results strengthened by Q' precipitates based on the equation 2 .

As the Mg added 319 alloys have two different precipitates after aging treatment, strengthening mechanism also operate simultaneously. The combining effects of two different precipitates on the dislocation movement barrier will be averaged based on the root-mean-square by Koppenaal and Kuhlmann-Wilsdorf [6].

$$\Delta \sigma_{ppt} = [\Delta \sigma_{\theta'}^{2} + \Delta \sigma_{Q'}^{2}]^{1/2} \quad (3)$$

They verified that in the case of simultaneous strengthening occurring by different precipitates, the root-mean-square method is a good averaging technique. However, the contribution of the grain size hardening and solid solution hardening occur independently. Simple superposition of the contribution from the intrinsic strengthening and solution hardening is enough for this case [1]. Therefore, the total strength in Mg added 319 aluminum alloy can be described as following

$$\sigma_Y = \sigma_i + \sigma_{ss} + \sqrt{(\sigma_{\theta'})^2 + (\sigma_{Q'})^2} \qquad (4)$$

B.3 Micromechanical Model

The modified Zhu models (eq. 1, 2) have focused on the physical aspects of precipitation such as precipitate size and shape, thickness, and volume fraction. Recently new precipitate strengthening models have been devised as a function of aging process variables such as aging time and temperature. Allison et al. [4] suggested that the equations for determining the diameter and thickness of precipitate experimentally as a function of aging time at a given temperature. The process models show the exponential growth equation for the diameter and a power-law equation for the thickness as follows.

$$D = a[1 - \exp(-bt)]$$

$$w = ct^{d} \qquad (5)$$

where ***D*** is diameter, ***w*** is thickness and ***a, b, c***, and ***d*** are constants obtained by experiment, and ***t*** is time. They used the TEM image analysis for the quantitative precipitate analysis.

The combination of the strengthening model (1) and the process model (5) will give a simple prediction by containing only one variable, aging time *t*. For the success of this micromechanical model, accurate measurement of precipitate properties such as diameter, thickness, and volume fraction by TEM and 3DAP analysis is essential. After quantitative TEM image analysis, the validity of the micromechanical model will be examined for the Mg added 319 aluminum alloys.

Assuming that only plate-like precipitates are dominant phase during the aging, the micromechanical model in the 319 aluminum alloys is described as follows

$$\sigma_{ys} = \sigma_{int} + 0.398\left(\frac{G\mathbf{b}}{\sqrt{D(t)W(t)}}\right)\left(\sqrt{f(t)} + 0.75\, f\sqrt{\frac{D(t)}{W(t)}} + 0.14\,\frac{D(t)}{W(t)}\, f(t)^{3/2}\right)\left(\ln\frac{0.87\sqrt{D(t)W(t)}}{r_o}\right) \qquad (6)$$

Based on the results proposed by Weakley-Bollin et al [4]. with our experimental results during the aging behavior as a function of time, the constant parameter in Eq. 5 were determined as a=78.2, b=3.46, c=2.78,d=0.2, and σ_{int}= 70Mpa. Using these parameters to the Eq. (6), we obtained the simulated yield strength by micromechanical model in Fig. 3. The experimental results measured by Rockwell hardness and electrical conductivity are shown in Fig. 4 as a function of aging time. The simulated results and experimental results show a good agreement, thus the micromechanical model are valuable to predict the yield strength in the 319 alloy system. However, for the better fit, it is necessary to consider the multi precipitates in the modified 319 type alloys.

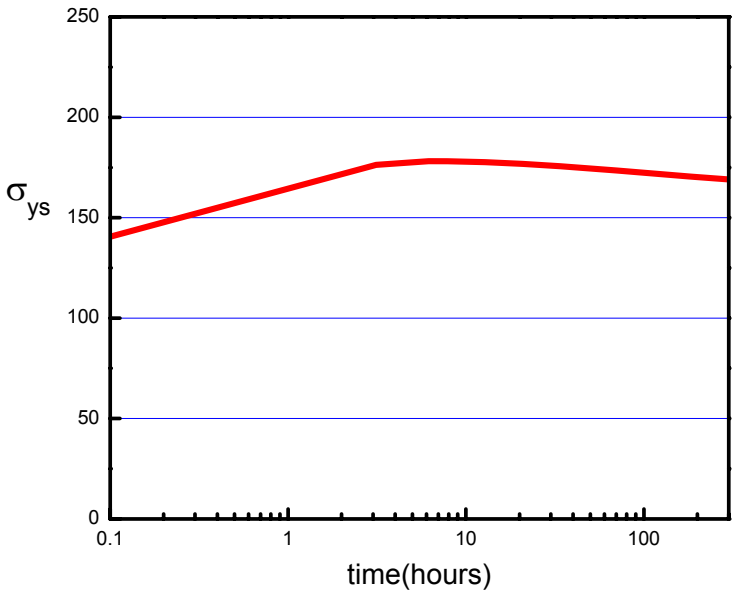

Fig.B.3 The simulated yield strength by micromechanical model [4].

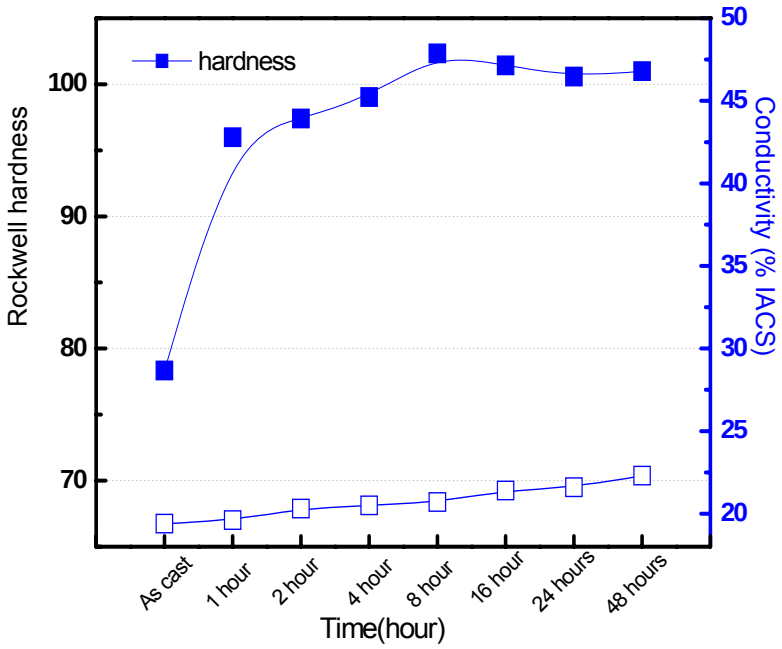

Fig.B.4 Experimental results measured by Rockwell hardness as a function of aging time.

B.4 Reference

[1] J.C. Williams, A.W. Thompson, Strengthening of Metal and Alloys, in "Metallurgical Treaties", Met. Soc. of AIME, Warrendale, Pa. 1981.

[2] A.W. Zhu, J. Chen, E.A. Starke Jr, Acta Mater., 48(2000)2239.

[3] A.W. Zhu, J. E.A. Starke Jr, Acta Mater., 47(1999)3263.

[4] S.C. Weakley-Bollin, W. Donlon, C. Wolverton, J.W. Jones, J.E. Allison, Metall. Mater. Trans. A, 35(2004)2407.

[5] E. Orowan, " Discussion" in Symposium on Internal Stresses in Metal and Alloy, Inst. of Metals, London, 1948

[6] T.J. Koppenaal, D. Kulhmann-Wilsdorf, Appl. Phys. Lett., 4(1964)59.